The Impact of Installation Effects on Propeller Design Optimization for Aerodynamic and Aeroacoustic Performance

Master Thesis

Wouter de Gruijl

Supervisor: Dr. ir. T. Sinnige

Thesis Committee: Dr. ir. T. Sinnige (supervisor)
Prof. dr. ing. G. Eitelberg (chair)
Dr. ir. W. Baars

Department of Aerospace Engineering
Delft University of Technology

This dissertation is submitted for the degree of
Master of Science

May 2022

Preface

This master thesis report is written to meet the graduation requirements of a Master of Science degree in Aerospace Engineering, with a specialisation in Flight Performance, at the faculty of Aerospace Engineering at Delft University of Technology. When I began working on this thesis I had several doubts. I was not familiar with propellers and aeroacoustics, and when I was reading the papers in the initial stages of the project, I was overwhelmed with a serious case of imposter syndrome. Nevertheless, I went forwards, and over time the pieces started falling in their place. The most important thing I learned from this project is to trust in my abilities, stay positive, and keep going. Several people have been invaluable in this journey. First of all I'd like to thank my supervisor Tomas Sinnige, who provided guidance and feedback on the project, and with whom I had genuinely enjoyable meetings discussing the physics and issues of this work. I'd also like to thank my girlfriend Yijia Chen, who's encouragement always came at the right time. Finally I'd like to thank my parents, who made it possible for me to go to university, and my brother, who has been a great companion for the last few years of my studies.

Wouter de Gruijl
Delft, May 2022

Abstract

The objective of this thesis is to quantify the impact of including installation effects in propeller design optimization for maximum aerodynamic efficiency and noise reduction. The non-uniform flow used to model installation effects in this work is an inflow under an angle of attack of 5 degrees. Given the increasing oil prices and growing concern about the impact of aviation on climate change, propellers have received renewed interest. While propellers have the potential to be significantly more efficient than their jet engine counterparts, they are considerably noisier. Noise pollution has become a more recognized issue, as more and more reports surfaced that people around airports suffer health consequences from the aircraft noise production. If propellers are to be made feasible for greener future aircraft, their aeroaocustic performance needs to be addressed. Several propeller design optimization studies have been performed by other authors, investigating design options to improve both aerodynamic and aeroacoustic performance. However, very few studies investigate a propeller operating in installed conditions. When installed on an aircraft, a propeller can be exposed to different types of non-uniform flow that could have a profound effect on the propeller's aerodynamic and aeroaocoustic performance. To realize actual performance improvements with propeller-driven aircraft, it is essential to understand the installation effects on the propeller's performance, and the potential design methods to mitigate or exploit these effects. The aim of this work is to add to this understanding.

To do so, a design optimization study was set-up, in which propeller designs were optimized for aerodynamic and aeroacoustic performance. A BEM-model was used for the aerodynamic performance, combined with a non-uniform flow model by van Arnhem to model the aerodynamic performance as a result of the inflow under an angle of attack. For the aeroacoustic performance, Hanson's helicoidal surface theory was chosen. This model also has an adapted version specifically for calculating noise when dealing with a non-uniform inflow. These models were selected for their relatively good accuracy and low computational cost, which made them suitable for inclusion in an optimization framework. Validation data showed that although all selected models show significant errors in absolute values when compared to CFD or experiment, they could all predict trends with acceptable accuracy and were found suitable to be used for the preliminary design studies described in this thesis.

The propeller designs are optimized for a specific mission that includes a climb and a cruise phase. Noise was only evaluated during the climb phase, since this flight phase is critical for community noise hindrance. The design variables studied in this work are the collective pitch angle and advance ratio, both varied for climb and cruise separately, and the twist and chord distributions. Propeller designs were optimized for different blade counts (3-6) separately. The optimizations were split up into two objectives. First the propeller design was optimized for aerodynamic performance only. Next, the propeller design was optimized for aeroacoustic performance only, but constrained such that its total mission energy expenditure was only allowed to deviate from the aerodynamic optimum with a set percentage (1%, 2%, and 5%). These optimizations were carried out for propellers exposed to uniform flow and propellers exposed to a non-uniform flow under a 5 degree angle of attack, such that comparisons could be made.

Results show that the aerodynamic performance for the isolated propeller designs improves

significantly with increasing blade count. This efficiency increase is largely due to an increase in induced efficiency, as lower blade loading is required to meet the thrust requirement at higher blade counts, such that induced losses can significantly be reduced. The performance increase flattens at 6 blades, since the chord length had reached the lower bound which was defined based on structural considerations, and there was little to no room for improvement in terms of induced and profile efficiency. For the aeroacoustic results, a significant decrease is seen in terms of noise with increasing energy penalty, 5 dB for the three-bladed propeller and 10.3 dB for the four-bladed propeller at 5% increased energy expenditure compared to the aerodynamic optimum designs. The main mechanism for noise reduction seen in the results is a sharp reduction in tip Mach number, achieved through an increase in advance ratio in fixed freestream conditions. Blade lift loading increases to compensate for the lower rotational velocity, such that the thrust requirement can be met, and a decrease in efficiency is observed, mainly due to increased induced losses. Higher blade counts are beneficial because they allow for lower blade loading requirement resulting in a larger reduction in tip Mach number, and increased acoustic interference between the pressure signals from the different blades, also leading to reduced noise experienced by the observer.

For the designs operating in non-uniform flow, very similar trends were observed in terms of aerodynamic performance increase with increasing blade count. The difference in efficiency of the installed designs compared to the isolated designs operating in a non-uniform flow was found to be negligible (-0.02% - 0.14%). No alternative design strategy by the optimizer was detected when comparing the changes in design variables and efficiency components that had occurred in the installed designs compared to the isolated designs. In terms of aeroacoustic performance, a significant increase in noise was found for the optimized propeller designs operating in non-uniform flow (18 - 24 dB), resulting from the unsteady loading, compared to the optimized propellers operating in uniform flow. However, the difference in average noise emissions of the installed designs compared to the isolated designs operating in a non-uniform flow was again found to negligible (-0.08 to -0.66 dB). A similar noise reduction strategy was used for the installed propeller designs, focusing on a reduction in tip Mach number. To achieve this aim, very similar changes in design variables were seen when comparing the propeller designs that were optimized for aeroacoustic performance in isolated conditions compared to those designs optimized in installed conditions. Only a slight deviation in the design variable values became visible for the 5% penalty case, showing a lower solidity, and slightly different pitch values and advance ratios. The overall reduction in tip Mach number and efficiency remained very consistent however, indicating that even though a small change might be visible in the design variables, the desired outcome was the same.

To conclude it can be said that for this particular non-uniform inflow, an inflow under a 5 degree angle of attack, with this particular mission design and evaluation set-up, installation effects made no significant differences in terms of design optimization strategy and performance improvement when included in the optimization. It is recommended to include more design variables such as propeller blade sweep, propeller diameter, and airfoil type, in future studies to further investigate whether these design variables will result in a difference between propeller designs optimized in uniform flow or in a flow under a 5 degree angle of attack. Furthermore the author recommends researching other types of non-uniform flow in a similar fashion, and to critically evaluate the mission design. Another common type of non-uniform flow, a wake impingement, might result in a different design strategy when included in an optimization routine, since it could require a different noise reduction strategy than the one employed for propellers in uniform flow.

Table of contents

List of figures

Nomenclature

Roman Symbols

c	Chord length
C_d	Section drag coefficient
C_l	Section lift coefficient
C_m	Moment coefficient
C_n	Normal force coefficient
C_P	Power coefficient
C_Q	Torque coefficient
C_T	Thrust coefficient
D	Diameter
E	Energy
f	Frequency
J	Advance ratio
$\dot{m}$	Mass flow
M	Mach number
n	Rotational velocity
N_B	Number of blades
P	Shaft power
p	Pressure
Q	Torque
R	Radius
r	Radial coordinate
T	Thrust

V	Velocity
V_∞	Freestream velocity

Greek Symbols

α	Angle of attack
β	Collective pitch angle
η	Efficiency
θ	Twist angle / Observer angle
Γ	Circulation
Λ	Sweep angle
ρ	Density
ϕ	Azimuthal angle / Observer angle
Ω	Propeller rotational speed

Acronyms / Abbreviations

BEM	Blade Element Momentum
BPF	Blade Passage Frequency
CFD	Computational Fluid Dynamics
FEM	Finite Element Method
MDO	Multidisciplinary Design Optimization
NACA	National Advisory Committee for Aeronautics
OASPL	Overall Sound Pressure Level
RANS	Reynolds Averaged Navier-Stokes
RMS	Root Mean Square
SPL	Sound Pressure Level

Part I

Background

Chapter 1

Introduction

This chapter forms the introduction to this work, and covers the research motivation, the research objective, and a general outline of the thesis work, all of which form the basis for the interpretation of this thesis.

1.1 Research Motivation

With an increasing concern of the impact of emissions from flight on the climate, an interest in the development of propeller-based engines for future aircraft has been reignited. It has long been known that turboprop engines have the ability to be 10%-30% more efficient than jet engines when cruising at a Mach number below $M = 0.7$[1]. However, the turbofan engine can typically generate more thrust, and cover a wider range of speeds. This made turbofan engines the engine of choice in the past decades, when environmental concerns were deemed less critical.

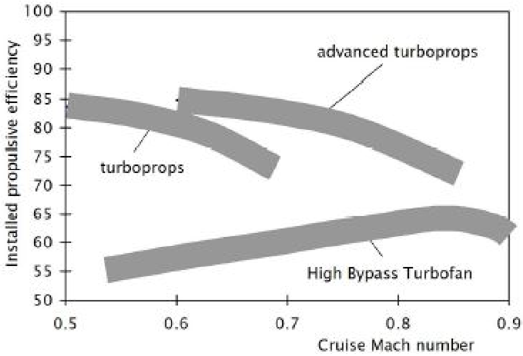

Fig. 1.1 Comparison of the installed propulsive efficiency as a function of the Mach number for turboprops, advanced turboprops, and turbofan engines. [1]

The reason that propeller engines can be more efficient compared to turbofan engines can be explained by observing the fundamental equations for thrust and efficiency that govern both types of engine. The first equation is the equation for calculating the engine trust, which is equal to the time rate of change of momentum:

$$T = \dot{m}\Delta V \tag{1.1}$$

The second equation describes the propulsive efficiency of the engine:

$$\eta_p = \frac{2}{2 + \left(\frac{\Delta V}{V_\infty}\right)} \tag{1.2}$$

Looking at the equation for the thrust, it can be seen that there are only two components that produce a given thrust, the mass flow $\dot{m}$ and ΔV. The ΔV component refers to the difference between the flow velocity before and after the engine. This component can also be seen in the formula for the propulsive efficiency, and the following can be deduced: for any given freestream velocity V_∞, the efficiency will be the highest for an as low as possible ΔV. This means, that if one wants to increase the propulsive efficiency, but keep the thrust level the same, the mass flow has to increase for an equal decrease in ΔV. Knowing this, the benefit of the propeller becomes apparent. A propeller is much better equipped to move larger amounts of air at a smaller velocity increment compared to a turbofan, for example by increasing the propeller diameter. Increasing the diameter would be more difficult for a turbofan, since the engine casing would have to scale with it, leading to a significant mass increase and an increase in drag, among other issues.

Propellers face disadvantages as well. Increasing propeller diameter would lead to increasingly higher airspeeds at the blade tip, eventually leading to such high Mach numbers that it will diminish propeller performance. This limitation is one of the reasons that propellers are also limited to lower cruise Mach numbers. Another limitation for an increase in diameter is the ground clearance, and clearance in general, as the possible positions for the propeller obviously decrease with an increase in the diameter of the propeller disk.

The lack of casing around the propeller, which is one of the reasons it can be scaled for higher efficiencies better than a turbofan, is also a cause for one of the propellers main disadvantages. Due to the lack of casing, the noise produced by the propeller can be emitted directly to its surroundings. As a result, propellers are generally noisier than their turbofan counterpart. Since noise pollution is a serious issue, as shown for example in the review by Swift[21], and regulations around aircraft noise are getting stricter, this is a problem that needs addressing.

Regardless of these disadvantages, propellers are still seen as a viable option to meet the sustainability requirements. To make this option more feasible, more research is necessary into the characteristics of propeller performance, such as the aeroacoustics, and the interaction between the propeller and the airframe. A better understanding of these phenomena, combined with techniques such as Multidisciplinary Design Optimization (MDO), can lead to propeller designs that can meet the noise and performance standards of the future. Another advantage of propellers is that they can be combined with electric motors. This also opens up interesting design avenues for more sustainable aircraft.

A number of studies have already been performed on propeller design optimization; these will be covered in detail in section 3.1. As these studies show, there is already quite some knowledge about how to model propeller blades, and optimize them for reduced noise emissions and increased efficiency. However, most of these studies look at the isolated propeller, and do not account for interaction effects between the propeller and the airframe. The presence of the airframe influences the incoming flow field, exposing the propeller to a non-uniform inflow. The composition of this non-uniform inflow depends on the location of the propeller on the airframe, as well as the orientation of the propeller with respect to the incoming airflow. Depending on the type of non-uniform inflow, the propeller will experience a certain change in aerodynamic and aeroacoustic performance.

In order to realize future-proof designs of integrated propellers, it is essential to get a better understanding of these interaction phenomena. Once these phenomena can be accurately modelled, optimization methods can also be used to optimize a propeller design for a given non-uniform inflow. This is not a trivial task, as it is difficult to model the interaction effects accurately without resorting to RANS CFD methods or similar high-fidelity methods, which are often computationally too expensive to feasibly include in an optimization framework. Furthermore, research has not yet properly established what the impact of non-uniform inflow on propeller design optimization is, and whether this effect is significant.

The main goal of the thesis is to realize an optimization framework for a propeller geometry that can include a non-uniform inflow interaction into the optimization, and study the impact of doing so on the resulting propeller design and its performance compared to a propeller optimized in uniform flow. This non-uniform inflow is modelled to represent a situation that would occur if the propeller were to be installed on an aircraft which is carrying out a mission. The optimization objectives are twofold, namely a maximum reduction in noise, and a maximum increase in efficiency. At the same time, reasonable constraints are set to other operational and geometric parameters to generate practically feasible propeller designs. A comparison is made between the optimized propeller design and performance in a situation with installation effects and a situation without installation effects, and conclusions are drawn on the necessity to include these installation effects in future studies. Furthermore, the impact of the installation effects on the optimized propeller geometry is observed, and these observations serve to better understand the design mechanisms that allow for noise reduction and increased efficiency in the given installed setting. Finally, insight is gained into the parameters that play a role in the trade-off between a design for minimal noise, and a design for maximum efficiency.

1.2 Thesis Aim and Objectives

As the previous section clearly indicates, studying and understanding the impact of installation effects on propeller performance and design optimization is of vital importance to be able to design propellers that have acceptable levels of noise and air pollution. However, the amount of research on propeller design optimization in installed conditions is very limited. Therefore, the main objective for this thesis work is stated as follows:

To quantify the impact of accounting for installation effects in propeller design optimization for maximum aerodynamic and aeroacoustic performance.

To achieve the objective, the following set of research questions was defined:

1. Based on literature, which aerodynamic and aeroacoustic performance models are capable of accurately modeling isolated and installer propeller performance, and are suitable for implementation in an optimization framework?
2. Which optimization method is suitable for this type of problem?
3. How to implement the trade-off between aerodynamic and aeroacoustic performance in the optimization framework that allows for clear quantification of the effects on propeller design for both types of performance?
4. What is the influence of installation effects on the propeller performance and optimized design?

The choice of aerodynamic and aeroacoustic performance models are based on literature, and verified and validated to ensure the results have a reasonable degree of confidence. The optimization method is also chosen based on literature and an assessment of the type of problem that needs to be solved. It is important to note that structural and aeroelastic models are not incorporated in this work. Instead, boundaries on the geometric parameters are set as such that the probability of a structurally feasible design is large.

1.3 Thesis Outline

This thesis is divided into four parts. The first part of the thesis (part I: Background) covers background information on the topic of this thesis. After the current chapter, part I includes another two chapters. Chapter 2 covers the background theory required for this work, which includes a number of fundamental principles of aerodynamic and aeroacoustic performance. Chapter 3 will cover previous notable propeller design studies, as well as an overview of the design consideration in light of improving propeller performance.

Part II discusses the research tools that were used to generate the results for this thesis. Chapter 4 starts off with describing the propeller design parameters that are relevant for this work, and the motivation behind including some parameters while excluding others. Next, chapters 5 and 6 cover the chosen aerodynamic and aeroacoustic performance models in details, including the reasoning behind choosing these specific models. Finally, chapter 7 discusses how all the chosen models were integrated in an optimization setup, and what the parameters of this setup are. Part III documents the verification and validation of the relevant research tools in chapter 8, and subsequently presents the results of the performed optimization work in chapter 9. The purpose of this part is to demonstrate that the used models meet a certain standard of accuracy, such that a reasonable amount of confidence can be put on the results of the optimization work, and then to discuss the obtained results in detail such that the research questions can be answered.

The final part of this work is Part IV. In this part, conclusions will be drawn based on the results presented in part III. This is also the part where the research objective is answered. The answers to the research question and the conclusions are presented in chapter 10. Based on the limitations found in this work, the author proposes a number of recommendations for future work in chapter 11, which is the final chapter of this thesis.

Chapter 2

Propeller Performance

In this chapter, a general background is provided on the theory of propeller performance. The theory presented is a summary of a very large body of work, and adapted to fit into the story line relevant for this project. Three aspects of propeller performance are discussed in separate sections, starting with aerodynamic performance in section 2.1, then the aeroacoustic performance in section 2.2, and finally the performance of a propeller when installed on an aircraft as opposed to isolated propeller performance in section 2.3.

2.1 Aerodynamic Performance

The main goal of a propeller is to generate thrust and thereby forward movement. The blades of a propeller can be seen as a set of radially distributed airfoil sections, very similar to the wing of an aircraft. During rotation, airflow approaches the propeller blade under an angle. The blade sections respond to this incoming airflow similar to the airfoil of a wing that is exposed to an airflow under an angle of attack. A schematic overview of the forces and velocities at play is shown in figure 2.1.

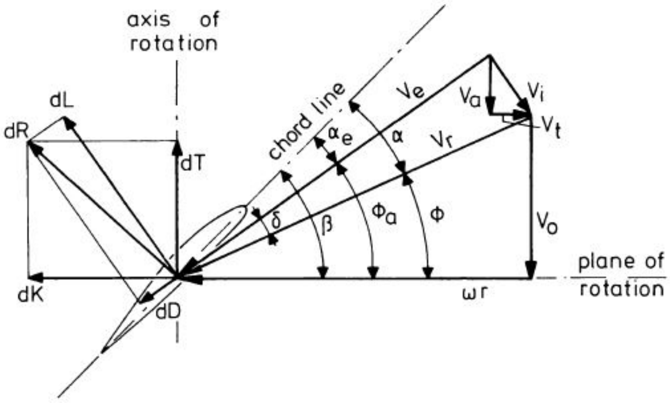

Fig. 2.1 A 2D representation of a blade element, adapted from Ruijgrok. [2]

Subjected to this airflow, the blade section produces a lift (dL) and a drag force (dD), which can be decomposed into a thrust (dT) and torque force (dK). Under the influence of the forces that are produced by the propeller, an additional induced velocity V_i shifts the relative velocity V_r with an angle δ. As can be seen in the figure, the pitch angle β is made out of the inflow angle ϕ and the angle of attack α. Since the pitch angle is typically fixed completely or fixed for at a certain setting for a particular phase of the flight (in case of a variable pitch propeller), the angle of attack is influenced mainly by the inflow angle ϕ, which can be controlled by changing the ratio of $V_o/\omega r$, indicated by the advance ratio (discussed below).

Considering the blade in 3D, the local rotational velocity component changes along the blade with increasing radial coordinate, changing the local angle of attack along with it. At the tip, the loading returns to zero due to tip-losses.

To evaluate the aerodynamic performance of the propeller, generally a small number of key performance indicators are used. These are:

- The thrust force T
- The shaft power $P = \Omega \cdot Q$ $(\Omega = 2\pi \cdot n)$
- The propeller efficiency $\eta = \frac{TV_\infty}{P}$

Furthermore, a metric that is often used in propeller analysis is the advance ratio J, which relates the freestream velocity to the rotational velocity.

$$J = \frac{V_\infty}{nD} \tag{2.1}$$

To be able to compare propeller designs, these performance indicators are typically non-dimensionalized. In the formulas presented below, the thrust and power coefficients are non-dimensionalized with respect to the dynamic pressure relative to the tip speed[22].

$$C_T = \frac{T}{\rho_\infty n^2 D^4} \tag{2.2}$$

$$C_P = \frac{P}{\rho_\infty n^3 D^5} \tag{2.3}$$

$$\eta = \frac{TV_\infty}{P} = \frac{C_T \rho_\infty n^2 D^4 V_\infty}{C_P \rho_\infty n^3 D^5} = J(\frac{C_T}{C_P}) \tag{2.4}$$

When assessing the aerodynamic performance of the propeller, these performance indicators are generally used, as well as the radial loading distribution along the blade. As can be seen, the definition of the efficiency in terms of the thrust and power coefficients can be traced back to the elemental formula for propulsive efficiency, which is defined as the useful thrust power over the overall shaft power. When substituting the thrust T and power P with the definitions for those variables derived from equations 2.2 and 2.3, equation 2.4 is obtained.

When it comes to the operation of the propeller, two types can be distinguished. Fixed pitch propellers have the geometry of their blades fixed, but vary the rotational speed during operation. By changing the rotational speed, and thus the advance ratio, the propeller is able to manipulate the generated thrust and the required torque. The second type is fixed speed propellers. This type of propellers operate at a constant rotational speed, but they vary their blade pitch during operation.

As a result, this type of propeller can manipulate the thrust and torque through changing blade pitch, and the advance ratio through adjusting the flight speed. Due to having two parameters available to influence the propeller performance, this type of propeller is generally able to fly more efficiently[2].

2.2 Aeroacoustic Performance

A disadvantage of propellers compared to jet engines is that they generally produce a lot more noise. This is caused, among other things, by the lack of casing around the engine. In order for propellers to become a more viable propulsion option for aviation in the future, design solutions will have to be implemented that can reduce the noise production to acceptable levels. Before design solutions can be found, the physics of noise production by propellers have to be properly understood. This section will cover the topic of isolated propeller aeroacoustics.

Propeller Noise Classification

Within the observation of propeller noise, three separate categories of noise are defined. These are (1) harmonic noise, (2) broadband noise, and (3) narrow-band random noise[3]. As the name suggests, harmonic noise (also known as tonal noise) is noise with a periodic component. This means that there is a certain constant period of time at which this noise will repeat itself. For an ideal propeller with B number of blades that operates at a constant rotational speed N, the fundamental frequency of the noise signal will be $B \cdot N$. The accompanying blade-passage period is then defined as $1/BN$. Usually, the noise is not purely sinusoidal, and thus has several harmonics which are multiples of the fundamental frequency. This is illustrated in figures 2.2 (time domain) and 2.3 (frequency domain). As can be seen, the harmonic noise can be represented by Dirac-delta functions exactly at the location of the fundamental frequency and its harmonics in the frequency domain.

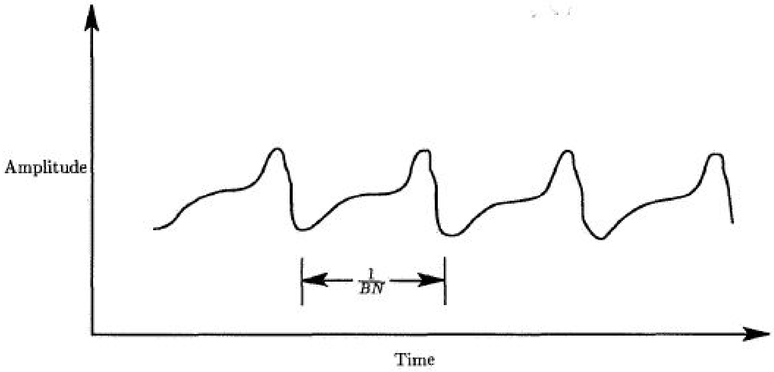

Fig. 2.2 Graphical example of harmonic noise in the time domain. [3]

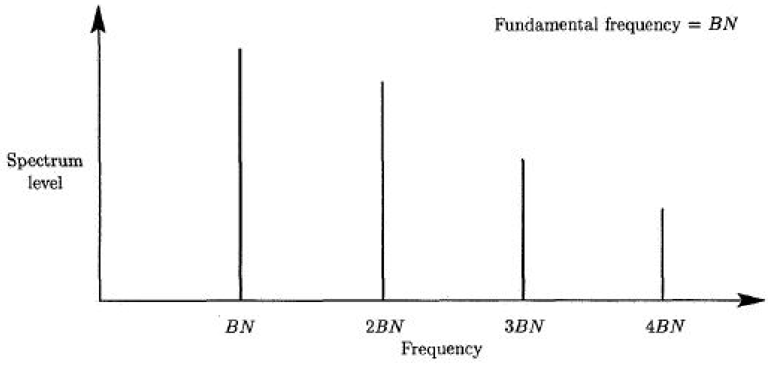

Fig. 2.3 Graphical example of harmonic noise in the frequency domain. [3]

Broadband noise is noise that is random in nature, and contains a very broad set of frequencies, hence the name. The random nature of a typical broadband noise signal is illustrated in figure 2.4. While a large range of frequencies is represented in the noise signal, some frequencies might have a larger amplitude than others, resulting in frequency domain curve as shown in 2.5.

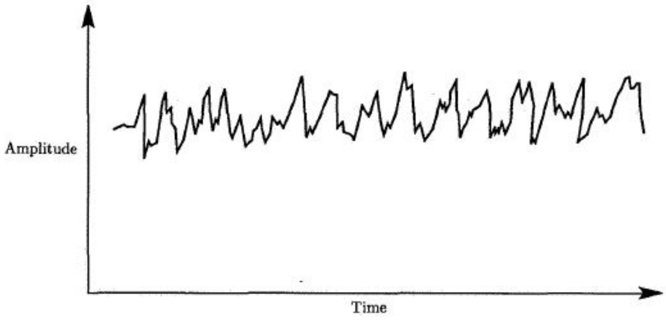

Fig. 2.4 Graphical example of broadband noise in the time domain. [3]

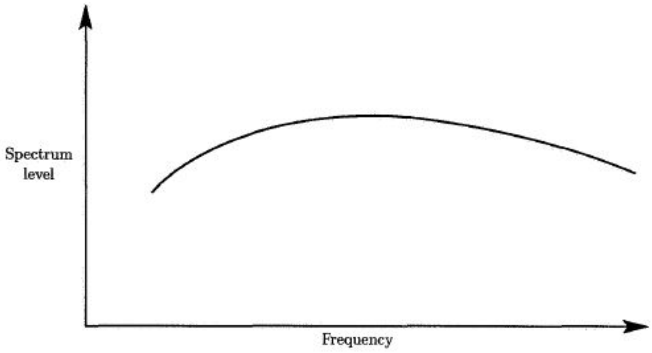

Fig. 2.5 Graphical example of broadband noise in the frequency domain. [3]

Narrow-band random noise has a periodic element, but is different from harmonic noise. When one observes the graph of narrow-band noise in the frequency domain, it can be seen that the sound energy is not concentrated at one single frequency or its harmonics, as it was for harmonic noise. Instead, the frequencies around the fundamental frequency and its harmonics are higher in energy as well. An illustration of narrow-band noise in the time domain and frequency domain can be seen in figure 2.6 and 2.7 respectively.

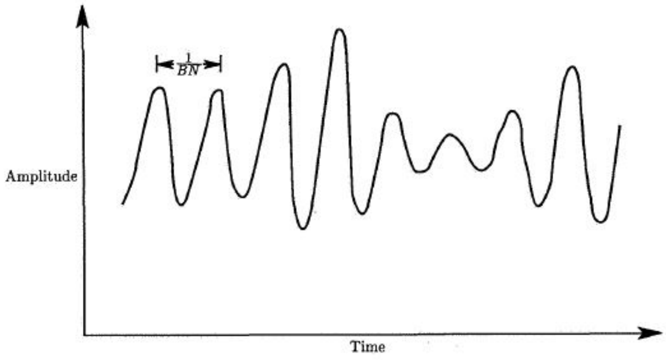

Fig. 2.6 Graphical example of narrow-band noise in the time domain. [3]

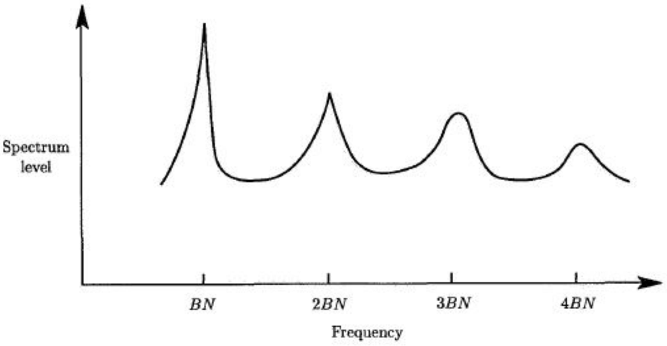

Fig. 2.7 Graphical example of narrow-band noise in the frequency domain. [3]

Figure 2.8 shows a graphic example of a full spectrum noise signal that could have been emitted by a propeller. Within this figure, *SPL* stands for the Sound Pressure Level, a metric that will be discussed in more detail later, and *BPF* stands for the Blade-Passage Frequency. When looking at the noise spectrum as a whole, one can still clearly distinguish the harmonic or narrow-band noise, which make up the peaks (denoted tonal in this case), and the broadband noise that supplies a sort of steady base of noise. As can be seen, the peaks caused by harmonic noise cause the loudest noise, especially at lower frequencies, which is why this type of noise is most relevant when analyzing propeller noise. Therefore, this is the only type of noise that will be considered in the remainder of this thesis.

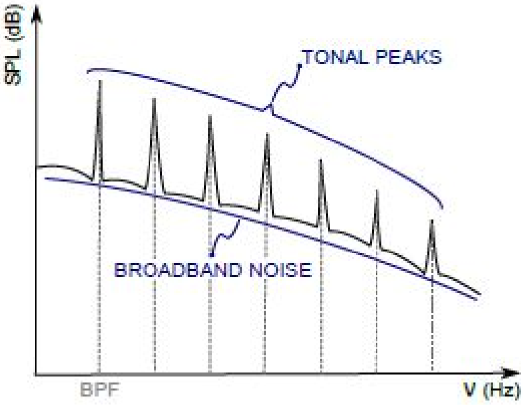

Fig. 2.8 Graphical example of a propeller noise signal in the frequency domain. [4]

Propeller Noise Sources

Next, the noise-generating mechanisms, or propeller noise sources will be discussed. These are generally divided into three categories: (1) Steady sources, (2) unsteady sources, and (3) random sources. All three will be discussed in that order.

Steady noise sources are noise sources that seem constant over time when observed from the point of view of the rotating blade. The steady noise sources can once again be divided into three categories, namely (1) linear thickness noise, (2) linear loading noise, and (3) quadrupoles (non-linear). The thickness noise originates from the periodic displacement of air by the volume of the blade element. While the frequency characteristics of this type of noise are determined by the rotational speed, the amplitude increases proportionally to the total volume of the blade. This type of noise is especially relevant at high speeds.

The loading noise relates to the forces that are produced by the blade, thrust and torque, which are the result of a pressure field around the blades that is induced by its shape and its motion. This pressure disturbance will propagate as noise, and is mainly relevant at low to moderate speeds.

These two noise sources are linear for moderate blade section speeds. However, when the flow over the blade sections reaches transonic speeds, non-linear effects such as shockwaves start to become significant. Quadrupole sources are used to model these effects. The quadrupoles will enhance the linear thickness and linear loading noise sources at transonic conditions for unswept, high-tip-speed propellers, and cause a noise increase.

Unsteady noise sources are also time dependent, however they are not constant over time and include periodic or random variations of loading on the blades. An unsteady noise source exists for example when a propeller shaft has a certain angle of attack with respect to the incoming flow. This leads to a variation in blade loading during the revolution, and thus in a variation of pressures surrounding the blade throughout the rotation, which cause the noise. Depending on the type of inflow distortion, the blade loading might even change several times per revolution. Unsteady noise sources are mainly the result of aerodynamic interactions with non-uniform flow as a result of the airframe (installation effects) or flight conditions. Unsteady noise sources are especially dominant during low-speed operations, while at higher flight speeds steady sources become more dominant. Since they are often periodic in nature, but usually with slight variations in the period, this noise source often presents itself as narrow-band noise.

Random noise sources are the sources that cause broadband noise. There are two random noise sources that are particularly relevant for propellers. The first source is a result from the interaction between the leading edge of the propeller blades and an incoming turbulent flow. Since the inflow is turbulent, the noise that results is random. The significance of this noise source depends on the magnitude of the turbulence in the inflow. The second source of random noise comes from the area near the trailing edge of the blades. Typically, a turbulent boundary layer is formed over the blade surfaces. This turbulent boundary layer can result in fluctuating blade loading at the trailing edge, which causes the noise. The noise profile is influenced by the boundary layer properties. Blade tip vortices can also cause this type of noise when interfering with the boundary layer at the trailing edge. It has been established in research by Dobrzynski et al.[23] that the broadband noise, which is caused by random noise sources, is a relatively unimportant noise source for full-scale propellers in flight.

Aeroacoustic Performance Indicators

To actually measure the aeroacoustic performance of a propeller, a performance indicator or metric has to be identified that represents the amount of noise a propeller creates, and makes comparison between different propeller designs easy. A parameter often used in the measurement of noise is the acoustic pressure at a position relative to a propeller. Since the pressure fluctuations of sound waves are experienced as sound by humans, it makes sense to use pressure as a metric to measure sound. The equation for the acoustic pressure, here shown in its root-mean square form, can be written as follows[24]:

$$p_{rms} = \sqrt{\frac{1}{2T}\int_{-T}^{T}(p(t)-p_0)^2 dt} \tag{2.5}$$

The root-mean square pressure represents the time average of the square of the fluctuating pressure. Looking at the equation, parameter $p(t)$ represents the pressure at a certain point in space and time and p_0 is the mean background pressure, thus $p'(t) = p(t) - p_0$ refers to the pressure perturbation at this same point.

Although the metric is used often, the pressure level on its own is not very intuitive. Therefore, a more common performance metric that is used is the sound pressure level (SPL). This metric compares the acoustic pressure p_{rms} with a reference pressure p_{ref}, and represents the noise level in terms of decibels. The SPL can be calculated by equation 2.6[24].

$$SPL = 20\log_{10}(p_{rms}/p_{ref}) \tag{2.6}$$

In most aerospace research that deals with aeroacoustics, the standard reference pressure that is used is $p_{ref} = 20\mu Pa$. This pressure level is considered the threshold of hearing for humans, and therefore ensures that the sound pressure level is scaled for the human ear.

Although often used, the metric of SPL is not related to the noise-generating source. If one wants to make a fair comparison between noise-producing propellers, a different metric is required that takes into account the diameter of the propeller and the thrust it produces. The TSSP (see equation 2.7) takes into account the pressure jump over the propeller disk (T/D^2) which allows for a better comparison between different propellers with different thrust-settings[16].

$$TSSP = 20\log_{10}(p_{rms} \cdot \frac{D^2}{T}) \tag{2.7}$$

2.3 Installation Effects

In propeller analysis, it is generally assumed that the propeller is subjected to a uniform inflow. However, when operating on an aircraft, there are numerous interaction effects at play between the propeller and the airframe, causing the propeller to actually experience a non-uniform flow. These interaction effects have an influence on the performance of both the propeller and the airframe. The kind of impact it has depends on many factors, such as the location and configuration of the propeller, and its positioning with respect to the freestream, among other things. Interaction effects between propellers and the airframe have been dealt with extensively in literature, such as in the dissertations by Veldhuis[1] and Sinnige[6], as well as a paper by van Arnhem[5]. These studies form the main sources for this section.

Depending on the location of the propeller on the airframe, there are several different types of non-uniform inflow that the propeller could encounter. A graphical overview of a number of cases is shown in figure 2.9.

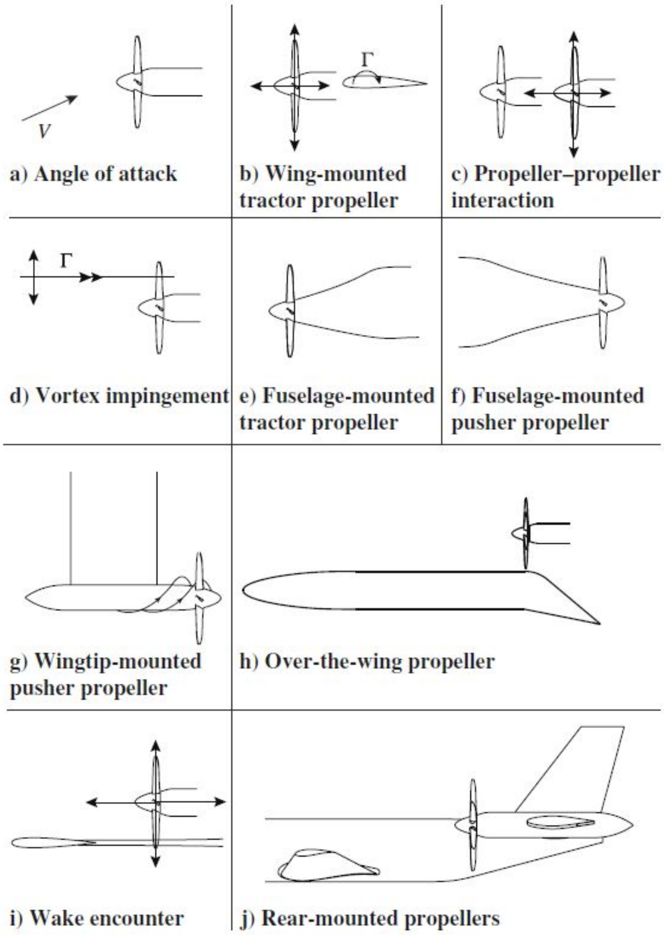

a) Angle of attack

b) Wing-mounted tractor propeller

c) Propeller–propeller interaction

d) Vortex impingement

e) Fuselage-mounted tractor propeller

f) Fuselage-mounted pusher propeller

g) Wingtip-mounted pusher propeller

h) Over-the-wing propeller

i) Wake encounter

j) Rear-mounted propellers

Fig. 2.9 Typical cases of propellers experiencing non-uniform inflow. [5]

Each of these cases has its own unique circumstances and interactions, and thus a different effect on the aerodynamic and aeroacoustic performance of the propeller and the airframe. For this thesis work the focus has been on the analysis of case (a), an inflow under an angle of attack, which has lots of similarities with case (b), where the propeller will experience an inflow under an angle due to the wing-induced upwash. The inflow under an angle of attack is naturally a very common phenomenon during aircraft operation, in particular during the climb phase, which is a critical phase to analyze when it comes to noise pollution around airports.

The interaction between the propeller and airframe does not only go one way. The propeller will also influence the performance of the aircraft. The slipstream of the propeller will cause a change in the aerodynamic performance of the surfaces downstream, and pusher propellers can create a suction effect on upstream surfaces. These effects should be taken into account during design as they have the potential to make the aircraft unstable. Designed intelligently however, these interaction effects can also be used to benefit the aerodynamic performance of the aircraft. In this thesis work, the focus will be on the effects of the airframe on the propeller only. The effects of the propeller on the airframe will not be taken into consideration.

Installation effects will cause a change in blade loading and performance along the azimuth of the propeller. As a result, the blade loading becomes a function of the azimuthal angle, rather than a constant value in the case of a propeller in uniform flow. This affects both the aerodynamic and aeroacoustic performance of the propeller. Additionally, it introduces unsteady effects which add an extra layer of complexity to the analysis. With an aerodynamic model for non-uniform flow (discussed in more detail in section 5.3), the change in the aerodynamic performance can be determined.

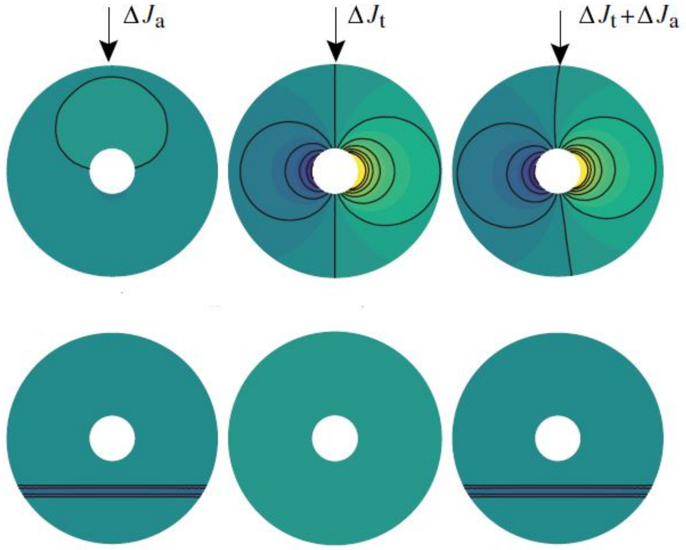

Fig. 2.10 Top: Propeller under an angle of attack, $\alpha = 5°$, $J_\infty = 1.8$. Bottom: Wake encounter, wing at $z/R_p = 0.5$, $J_\infty = 1.8$. Adapted from van Arnhem. [5]

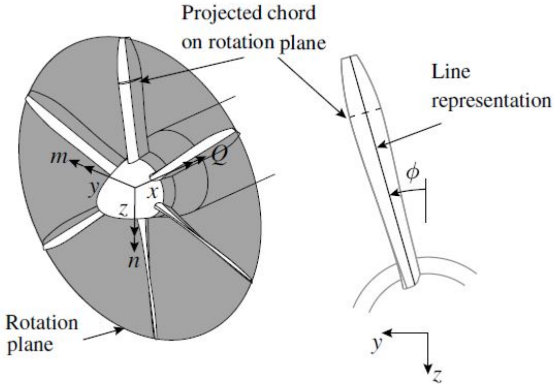

Fig. 2.11 Definition of the propeller rotation plane on which the inflow is determined and its axis system. [5]

Figure 2.10 shows an example of the difference in the axial and tangential advance ratios J_a and J_t as a result of two types of non-uniform flow as determined by the aerodynamic model by van Arnhem, and figure 2.11 shows the coordinate system used throughout the paper by van Arnhem[5]. The definition of these advance ratios will be discussed more in detail in section 5.3. However, for the current discussion it suffices to say that the axial advance ratio J_a only changes due to a change in the axial velocity, which corresponds to a change in the velocity pointing in the direction of the x-axis in figure 2.11. The tangential advance ratio J_t only changes due to a change in the tangential velocity V_t, which is calculated using equation 2.8, in which Δv corresponds to a velocity change along the y-axis, Δw to a velocity change along the z-axis, and ϕ the azimuthal angle of the propeller blade (all shown in figure 2.11).

$$\Delta V_t = -\Delta v \cos\phi - \Delta w \sin\phi \tag{2.8}$$

The unsteady loading that results also requires an adaptation of the noise model, which has to be able to take into account unsteady effects in order to accurately predict the produced noise by the propeller. Later on in chapter 6 the noise model will be discussed in more detail as well as the distinction between the steady and unsteady versions of the model. Since this work specifically focuses on analyzing the performance of a propeller with an inflow under a non-zero angle of attack, the next section will cover in more detail the theoretical background and literature on this phenomenon and its impact on performance.

Propeller Under an Angle of Attack

A propeller under an angle of attack is perhaps the most common type of non-uniform inflow, and therefore an interesting situation for investigation. In the top row of figure 2.10, taken from the study of van Arnhem[5], the change in local advance ratio at the propeller disk can be seen for a propeller at an angle of attack of 5 degrees, and a freestream advance ratio of 1.8. The left disk shows the change in axial advance ratio, the middle disk the change in tangential advance ratio, and the right disk the combined effect.

As can be observed in the figure, there is very little variation in the axial advance ratio. However, an interesting effect can be observed in the disk representing the variation in the tangential advance ratio. On one side of the propeller disk, the tangential velocity is in the same direction as the rotation direction, while other side it is opposite to the rotation direction. As a result a symmetric situation occurs where on one side there is a local increase in advance ratio and on the other side a decrease of similar magnitude. A change of up to 35% in effective advance ratio can be observed, with maxima at the azimuthal angles of $\phi = 90°$ and $\phi = 270°$, which leads to a cyclic variation in blade loading. The cause of this can be explained as follows.

When operating under an angle of attack, the upcoming blade will experience a different effective angle of attack compared to the down-going blade. This is illustrated in figure 2.12. As a result, the down-going blade will experience a load increase while the upcoming blade experiences a load decrease.

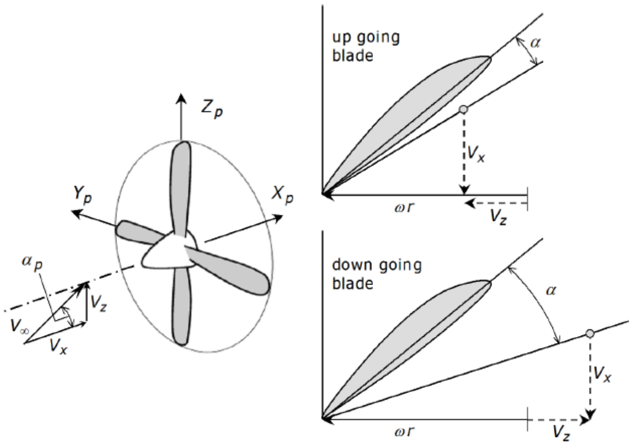

Fig. 2.12 Blade angle of attack variation due to the propeller pitch angel. [1]

The forces created on the blade due to this non-uniform flow are periodic in nature. In figure 2.13, adapted from the dissertation of Sinnige[6], the change of the blade normal force coefficient is shown for all azimuthal angles. As can be seen, the blade loading displays a sinusoidal-like variation. The frequency of this variation is equal to the rotational speed of the propeller.

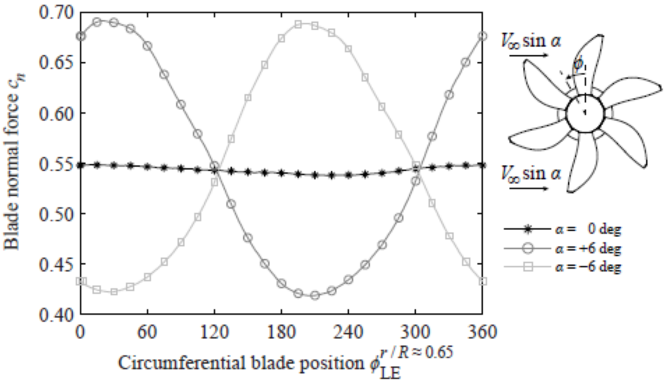

Fig. 2.13 Non-uniform blade loading as a result of an inflow under angle of attack. [6]

As stated in the dissertation by Veldhuis[1], this type of non-uniform inflow results in a net time-averaged force and moment around all three axes. The in-plane forces that are generated as a result can create a moment which can effect the stability and trim characteristics of the aircraft. Previous studies such as those by Kuhn[25] and Bencze et al.[26] have demonstrated that the resulting moment coefficients are relatively small when compared to the total values of the aircraft in question. However, even though the contribution might be small, the effect may still be noticeable, as was shown in the study by Veldhuis et al.[7]. In figure 2.14, taken from this study, one can see the effect of the propeller on the longitudinal stability of a Fokker 27 model measured in a windtunnel. Another study by Stuermer[27] found that the propeller under investigation at an angle of attack of 10 degrees generated a lift force equal to 7% of the thrust force and lateral forces equal to approximately 2% of the thrust.

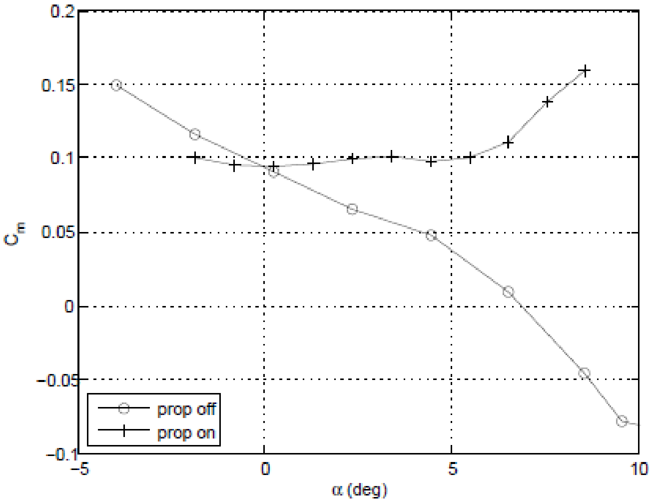

Fig. 2.14 Effect of propeller on the static longitudinal stability of the Fokker F27 aircraft model in the windtunnel. The pitching moment coefficient was taken with reference to the model pivot point in the wing (not c.g.). [7]

A study by Sinnige et al.[8] showed that the effect of the angle of attack on the propeller thrust coefficient depends a lot on the advance ratio. In figure 2.15, the change in thrust coefficient as a function of the angle of attack for different advance ratios is shown. As can be seen, the thrust coefficient is barely influenced for lower advance ratios, and becomes more sensitive to a change of angle of attack with higher advance ratios. The reason for this decrease in sensitivity at higher thrust settings (lower advance ratios) is related to the associated increase in rotational velocity. As a result of this increase in velocity, the effective angle of attack perturbation at the blade decreases for a given angle of attack of the global inflow.

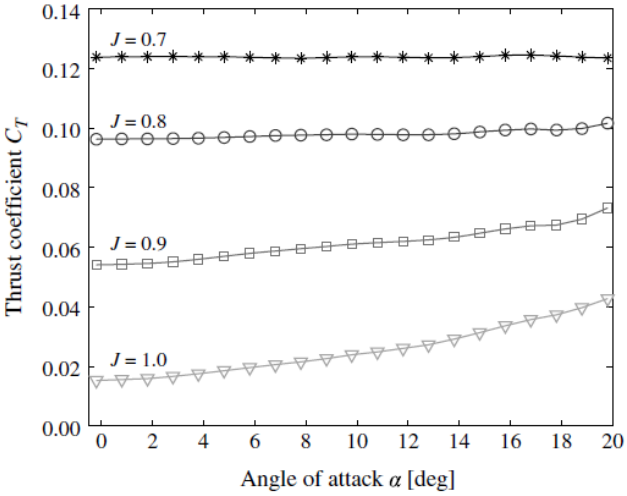

Fig. 2.15 Effect of angle of attack on the propeller thrust at $Re = 620,000$. [8]

In the study by Veldhuis et al.[7], the influence of the angle of attack on the propeller efficiency was determined. In figure 2.16, the results can be seen for two different advance ratios. As can be observed, the effect on the efficiency is relatively small. For the advance ratio of $J = 1$, a maximum efficiency increase of 1.1% was found, while for the case of $J = 0.75$ the maximum increase was found to be only 0.3%. This is according to expectations based on what the findings presented in figure 2.15, since the influence of the angle of attack on the thrust coefficient is larger for higher advance ratios.

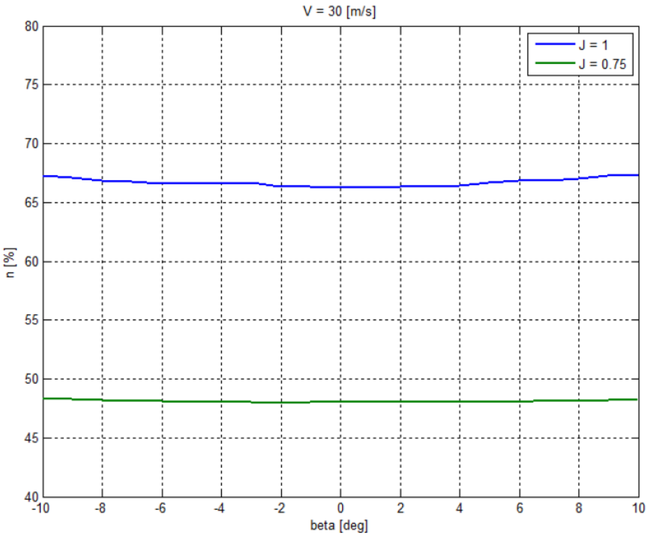

Fig. 2.16 Efficiency change with respect to angle of attack (beta) for two advance ratios, determined by experiment. [7]

Since there is a periodic change in loading, an increase in noise is also expected. A study by Heidelberg and Woodward[9] aimed to quantify the noise increase as a function of the angle of attack, and they found an increase of approximately 0.6 dB per degree of increase in angle of attack. As can be seen in figure 2.17, this correlation was very consistent even for propellers that were configured at different droop angles. Besides this study, the author is not aware of studies that quantify the effect of this type of non-uniform inflow on the aeroacoustic performance of the propeller. Since the change in loading is distributed over the entire azimuth and changes gradually, the noise penalty is expected to be lower compared to a sudden change in blade loading. But this should be investigated further before definite conclusions can be drawn.

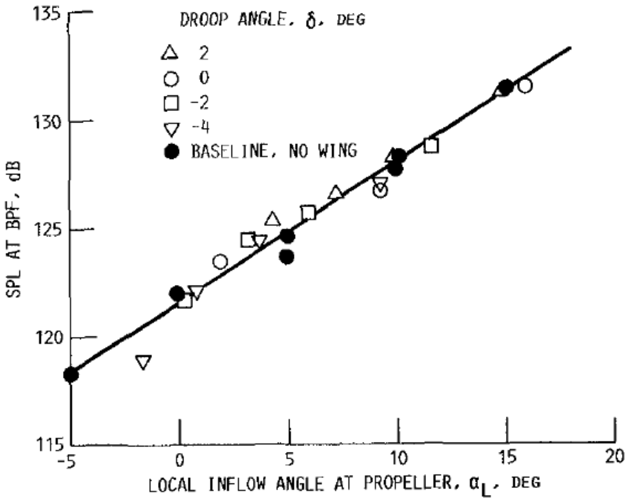

Fig. 2.17 Maximum flyover tone noise as a function the local propeller inflow angle for straight wing and no wing, $J = 0.88$, $M_\infty = 0.2$ [9]

Chapter 3

Propeller Design Considerations

This chapter covers propeller design considerations. Section 3.1 covers a number of the most prominent propeller design studies found in the literature and discusses the relevant conclusions from these studies regarding this work. After that, section 3.2 discusses multidisciplinary propeller design, covering design considerations for both aerodynamic and aeroacoustic performance and some of the design variables that play a major role.

3.1 Previous Work on Propeller Optimization

In the past few decades, a number of propeller design optimization studies have been published. With a few notable exceptions, most of these studies only considered the propeller in uniform flow, and did not include a structural model in their analysis. What follows is a brief overview of the most notable studies in this field and their findings.

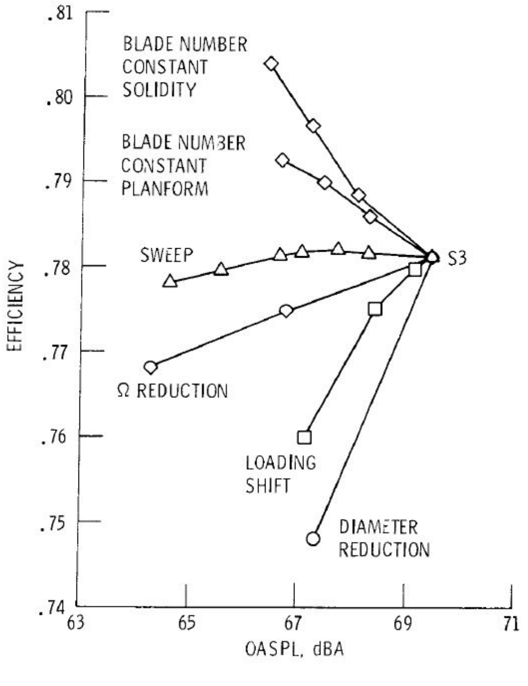

Fig. 3.1 A graphic representation of the sensitivities of various propeller design parameters with respect to efficiency and noise, measurement conditions at $J = 0.8$ and $C_p = 0.154$. [10]

One of the first notable design optimization studies is the one by Miller and Sullivan, published in 1985[10]. In the published article the development of a preliminary design tool for the combined optimization of efficiency and noise is described. In the tool, a vortex lattice method is used for the aerodynamic analysis and a time-domain method for the aeroacoustic analysis. A number of design parameters are varied to receive an optimal design, among which are the sweep, propeller diameter, and number of blades. The most notable result from this study is that the authors carried out a sensitivity study for several design parameters regarding efficiency and noise. The results can be seen in figure 3.1. As the figure shows, an increase in blade number has a positive effect on both the aerodynamic and aeroacoustic performance. Another interesting observation is that significant noise reductions can be realized with sweep, while the efficiency is not much affected.

The paper also elaborates on the methods to mitigate noise. Two methods are pointed out. The first method is phase cancellation, which can be achieved mainly through changing the sweep and increasing the blade count. Adding blade sweep introduces a phase lag between the pressure signals emitted from the different radial blade segements. The interference caused by this phase lag can result in a significant noise reduction. This phenomenon has been extensively covered by Hanson[11], and is illustrated in figure 3.2.
The second method is through a reduction in noise source strength. This can mainly be done by reduction of the effective Mach number, either through lowering the rotational speed, decreasing the propeller diameter, or changing the blade geometry.

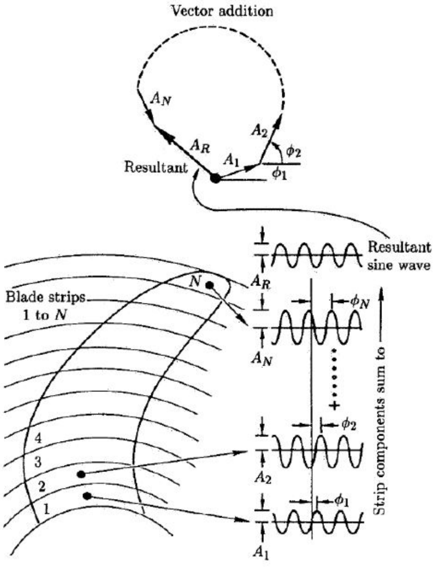

Fig. 3.2 An illustration of the noise interference due to blade sweep. [11]

The design optimization study published in 2008 by Pagano et al.[12] is notable since it is perhaps the only study that optimizes the propeller geometry in an installed condition, in this particular case the installed propeller of a Piagio P180 Avanti. For the aerodynamic analysis, a BEM method was combined with a surrogate model based on the full potential equation for which the data was generated by CFD. While the BEM method was used for an initial simple aerodynamic analysis, the surrogate model was used for modelling the impact on aerodynamic performance due to three-dimensional effects or unsteadiness. A FEM model was used for the structural analysis, and weak coupling between the aerodynamic and structural performance was implemented. For the aeroacoustic analysis, the Farassat 1A model was used for the tonal noise, and broadband noise was estimated based on statistics of a RANS solution of the 3D blades. A Pareto front was generated, out of which two designs were picked and can be seen in figure 3.3. The first design (green) is the design with the maximum reduction in acoustic energy (1.5 dB for this research). The second design (red) is the design with the maximum efficiency gain, which was found to be equal to two counts while still realizing a very small reduction in the acoustic energy. As can be seen, the sweep angle at the blade tip is the most notable difference compared to the baseline propeller. It should be noted that this study encountered some robustness issues in the grid generation of the model, as a result of which the flow and acoustic effects of the inboard section of the blade and the hub region could not be captured.

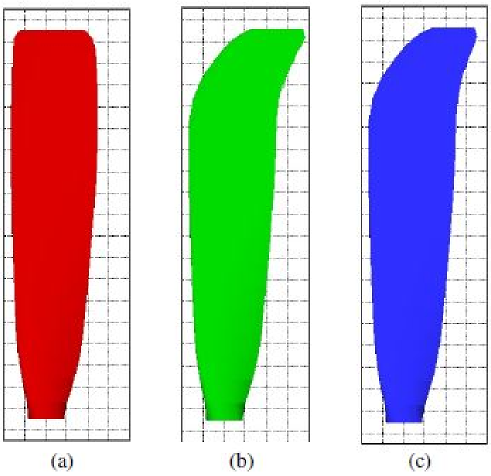

Fig. 3.3 Comparison of blade geometries: (a) Baseline (b) Design for maximum reduction in acoustic energy (c) Design for maximum efficiency gain. [12]

The in 2011 published PhD dissertation from Marinus[4] presents a propeller optimization study in which aeroelasticity is taken into account. For the aerodynamic analysis a RANS CFD model was implemented, of which the results were used to create a surrogate model. The aeroacoustic analysis was based on the Farassat 1A model. The aeroelastic analysis was based on a FEM solver and decoupled from the aerodynamic analysis. As such it was only used as a sanity check from a structural point of view. Unfortunately, issues were encountered with the implementation of the CFD analysis in the optimization tool, leading to convergence and mesh failures in 53% of the analysed cases. Some optimized designs could still be generated, and are shown in figure 3.4. Similarly to the results from Pagano, a sweep near the blade tip can be seen. Notable in these results is also the change in chord length along the length of the blade. This caused the loading the move inboard, thereby potentially reducing the noise due to the fact that the loading noise on the inboard section is radiated less effectively, as noted by the author. This supports the use of chord length as a design variable to impact both aerodynamic and aeroacoustic performance.

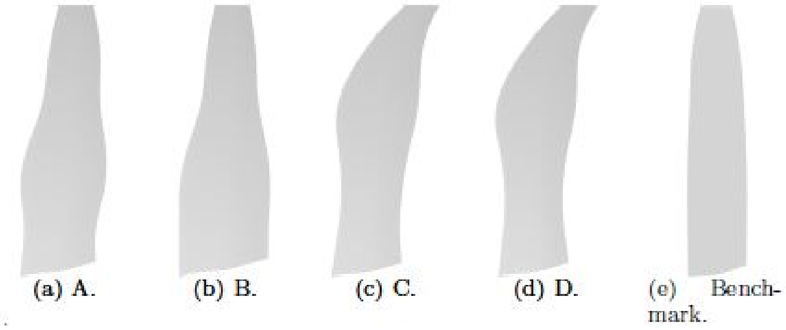

Fig. 3.4 Propeller blade shapes optimized for A: Propeller power at three advance ratios B: The Sound Pressure Level (SPL) in the propeller plane both in cruise and landing/take-off C & D: The SPL at three receiver locations both in cruise and landing/take-off. [4]

A study by Hu[13] used a BEM model with an adaptation to account for sweep, and Hanson's helicoidal surface theory to predict the propeller noise. The propeller geometries in this study were optimized specifically to minimize the thrust specific noise level $p_{rms}D^2/T$. A constraint was set on the propeller efficiency and the thrust coefficient. The chord distribution, pitch angle distribution and sweep were set as design variables. Two of the resulting geometries are shown in figure 3.5.

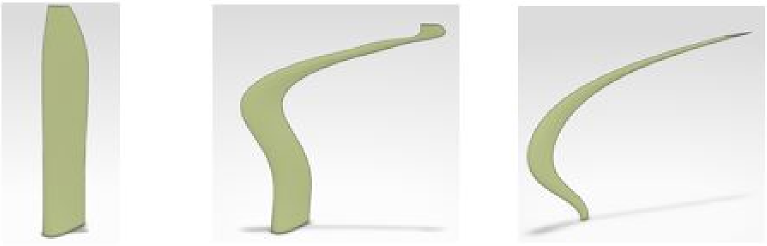

Fig. 3.5 Two optimized blade geometries and the reference blade from the optimization study of Hu. [13]

The optimized designs realized a substantial decrease in the predicted noise production of over 20 dB compared to the baseline, while keeping the change in efficiency minimal. However, the practical application of the results is questionable, since the resulting geometries are not very suitable for manufacturing due to their extremely complex geometries. Furthermore, it is doubtful whether these geometries would be structurally feasible. Although the research once again highlights the immense influence sweep can have on noise reduction, it also clearly shows the necessity of implementing a form of structural constraints to make sure the optimized geometries stay within feasible boundaries.

In general it can be observed from the literature that the sweep angle is an especially effective manner of reducing noise while simultaneously keeping the reduction in efficiency relatively low. Furthermore, most studies do not include installation effects, thereby highlighting the gap in research the thesis aims to make a contribution to. Aside from the work of Miller and Sullivan[10], not many sensitivity studies have been carried out that show the effectiveness of the change in various parameters or operational conditions on the aerodynamic and aeroacoustic performance of propeller blades. Lastly, it seems that the incorporation of some form of structural constraints is recommended to prevent the generation of impractical and unfeasible blade designs.

3.2 Multidisciplinary Propeller Design

As becomes apparent from previous design studies, there are a number of propeller geometry variables that can be changed in order to achieve better performance in terms of aerodynamics or aeroacoustics. Furthermore it is clear that some variables can have opposite effects in terms of improvement of these types of performance, where some improve aerodynamic efficiency, but simultaneously increase noise production, or the other way around. This means that in order to find a compromise between aerodynamic and aeroacoustic performance, a multitude of variables should be considered in the design process. The following design parameters are of particular interest:

- Propeller diameter
- Blade number
- Blade twist distribution
- Blade pitch
- Blade thickness distribution
- Blade chord length distribution
- Blade sweep distribution
- Airfoil type

Another design variable of interest that does not relate to the propeller geometry is the propeller rotational speed, which has been used in the work by Miller and Sullivan[10]. Furthermore, the operational condition of the propeller should be considered, which also determines the relevant range of advance ratios. Next, a brief overview of the effect of some of these design parameters on the propeller performance will be given.

Design Considerations For Aerodynamic Efficiency

Reviewing the graph from Miller and Sullivan (see figure 3.1), it shows clearly that increasing the blade count increases propeller efficiency. This is mainly due to the fact that increasing blade count reduces the blade tip losses. An increase in diameter can also increase efficiency, as it allows for moving a larger amount of air for a smaller velocity increment. More precisely, there is a lower disk loading for a given thrust requirement, which reduces axial induction losses. Both are however limited by structural and manufacturing constraints. The blade count is generally limited by the complex integration of the blades in the hub. The propeller diameter is limited by clearance issues, but also by the airflow reaching velocities near the transonic regime at the tip if the diameter gets large enough, which could result in shock waves and associated aerodynamic and aeroacoustic penalties. Since increasing the blade count benefits both aerodynamic and aeroacoustic performance, but is limited by structural considerations, this parameter is usually fixed up front during the design optimization.

To operate at a maximum efficiency, the thrust-to-torque ratio of each blade should be maximized. This can be achieved by adapting the blade geometry through the chord and twist distribution, pitch angle, and airfoil type. These parameters can be optimized in the optimization routine such that the operational requirement for thrust is met while achieving maximum efficiency.

Design Considerations for Aeroacoustic Performance

As mentioned in section 3.1, there are two main methods of realizing a reduction in noise. The first method is phase cancellation, which is primarily achieved by increasing the blade count or applying blade sweep. As can be seen in figure 3.1, both methods can realize significant reductions in noise, while either benefiting or only marginally reducing aerodynamic efficiency.

Reducing the noise source strength, the second main method, can be achieved in several ways, most of which are focused on a reduction of the tip Mach number. A reduction in the rotational speed of the propeller (for a given freesteeam velocity) leads to a lower tip Mach number. However, due to the lower rotational speed, a higher pitch setting is required to maintain the same amount of thrust. A higher pitch setting and reduced rotational velocity generally indicate an increase in the inflow angle. The increased inflow angle causes a larger part of the lift vector to point in the torque direction, thereby reducing the thrust-to-torque ratio. As a result, the decrease in rotational speed comes with a slight decrease in aerodynamic efficiency as well. Reducing the propeller diameter is another method to decrease the tip Mach number, if the advance ratio is not maintained. However, it increases the disk loading for a given thrust requirement, resulting in reduced propeller efficiency due to increased induced losses associated with the axial acceleration. A shift in loading can also reduce noise. By moving the loading away from the tip, the significant influence of the tip section on the sound levels is decreased. This inward loading shift however also reduces the effective diameter of the propeller, dividing the loading over a smaller effective disk, which leads to a significant decrease in efficiency. As figure 3.1 already suggests, beyond blade number, and in some cases sweep, other design and operational variables can not benefit both aerodynamic efficiency and better aeroacoustic performance at the same time. When designing, the weighted importance of these two performance objectives will determine how these variables should be balanced out in an optimal way.

Part II

Methodology

Chapter 4

Propeller Blade Parametrisation

The propeller and propeller blade geometry can be defined with a large number of parameters. This chapter will discuss these design parameters in more detail and in the context of this thesis work. Section 4.1 contains a summation of the most notable design parameters for this work, a discussion on the expected impact of the parameters on the propeller performance, and the reason to include or exclude these parameters in the design study. Section 4.2 goes more in-depth on the parametrisation of radially distributed design parameters, such as the chord length, and how these design parameters can be included optimally in the optimization framework.

4.1 Propeller Design Parameters

The propeller design parameters can be divided into two categories. The first category of parameters define the overall propeller design, irrespective of the blade geometry, such as blade count and propeller diameter. The second category of parameters concern the blade geometry itself, such as chord and twist distribution. In this thesis work, optimization methods were used to generate novel propeller designs optimized for a certain performance objective. For optimization purposes, it is beneficial to have the propeller design defined by a minimal number of variables. The larger the number of variables, the larger the computational effort required for each iteration. Furthermore, the type of optimization methods that can be used differs when discrete variables such as the blade count are among the design variables during optimization. What follows is a list of the design variables and their role in this work.

- **Number of Blades**
  Increasing the number of blades is one the design considerations that will benefit both aerodynamic and aeroacoustic performance (as discussed in section 3.2). However, the number of blades is limited by the complexity of structural integration at the hub. Furthermore, it is a discrete variable, which would introduce additional complexity in the optimization setup. Besides, it is likely that the optimizer will always choose the largest number of blades anyway, which makes it an uninteresting variable to include in the optimization setup as design variable. Therefore, in this thesis work, propellers with 3 to 6 blades were separately optimized, such that for each blade count there was a unique optimized design. This allowed for a comparison between blade count without using the blade count as a design variable that could be controlled by the optimizer.

- **Propeller Diameter**
  The propeller diameter will influence aerodynamic performance by determining the mass flow, and the aeroacoustic performance by influencing the tip Mach number (when the advance ratio is not fixed). The maximum diameter is however limited because of clearance and positioning constraints. In this work, comparisons were made to a fictional case of an aircraft from the work of de Haan [28], from which results were used as a foundation for this work. The case presented in his work used a fixed propeller diameter, and for consistency purposes the diameter was therefore also not included as a variable in this thesis.

- **Airfoil**
  Similar to a wing, the propeller blade cross-section has an airfoil shape. The shape of the airfoil influences the chordwise loading distribution, as well as the radial loading distribution through influencing the section loading, both of which can influence the aeroacoustic and aerodynamic performance of the overall blade. Including the airfoil shape as a design variable in optimization introduces significant complexity. Lift and drag polars and the pressure distribution will have to be calculated for each cross-section at every iteration, introducing a large amount of computational effort. Furthermore, several other works on propellers, such as those of van Arnhem, de Haan, and Burger[5][28][29], have used a Delft University of Technology reference airfoil taken from the TUD-XPROP design (see details in van Arnhem [5]). To make comparisons between these works easier, and to save computational time, it was therefore decided to not vary the airfoil shape, but rather stick to the TUD-XPROP airfoil geometry.

- **Chord Distribution**
  The chord distribution is defined as the distribution of the chord length along the radius of the blade. The chord length influences the lift and drag forces on the respective element it applies to. Varying the chord length can therefore be used to change the blade loading along the radius of the blade. The chord distribution has been included in the design variables of this work.

- **Twist Distribution**
  The twist angle is the angle between the chord line of the airfoil section and a reference airfoil section which is typically located at 70% of the radius of the blade. The twist distribution thus defines the range of these angles for each blade section along the radius of the blade with respect to this reference position. The twist angle influences the local angle of attack with respect to the inflow angle, and thus the loading generated by that section. The blade loading can be optimized by varying these angles. The twist distribution has been included in the design variables of this work.

- **Sweep Distribution**
  In propeller design, the sweep is typically defined using mid-chord alignment, which measures the offset between the mid-chord point of each element and the mid-chord point of the root element. As discussed in chapter 3, sweep has the potential to reduce noise while keeping the loss of aerodynamic efficiency minimal, and is therefore an interesting variable to consider. However, due to time and complexity constraints, it was decided not to include

sweep as a design variable in this work. Moreover, the numerical models selected for this work are not able to handle the effects of a sweep angle very well.

- **Pitch angle**
  The pitch angle is an angle equally applied to the entire blade, and defined as a rotation around the pitch change axis of the root airfoil section. Typically, this angle is added after the twist distribution, and can be measured at 70% of the blade radius, where the twist initially is 0 degrees. The pitch setting is an interesting variable, as it can be changed depending on the flight condition when the aircraft employs a variable-pitch propeller, while the twist distribution remains the same. As such, the inflow angle can still be changed, despite the fixed blade geometry. The pitch is used as a design variable in this study.

Other propeller design parameters not included in this list are the design features of the spinner and the nacelle. Both of these were however not of interest to this particular thesis work, and therefore the spinner and nacelle designs of the TUD-XPROP were used throughout the entirety of the study. For the radially distributed parameters, the propeller blade was divided up into sections with a certain length dR. The exact method of the parametrisation of these variables is discussed in section 4.2.

4.2 Parametrisation of Radial Distributions of Design Parameters

Two sets of the design variables used in this study are radial distributions, namely the chord and the twist distributions. Theoretically, one could cut the propeller blade into a very large number of radial sections, leading to a large range of radial points, which each could have a different chord length or twist angle. This wouldn't be ideal, as the computational effort of the optimization grows with the number of design variables and it would lead to non-smooth distributions. In this particular study, 23 blade elements are defined, based on the normalized radial locations at which the TUD-XPROP airfoil profiles are defining. Determining a twist angle and chord length for each radial station would thus lead to 46 different design variables.

To minimize the number of design variables, a Bézier curve approach is used to describe the distributions. A Bézier curve can be described using only a small number of control points. Using these control points as design variables can therefore significantly decrease the number of design variables, and reduce the computational effort required for optimization. An example of control points and the resulting Bézier curve can be seen in table 4.1 and figure 4.1

Table 4.1 Control point coordinates for the Bézier curve in figure 4.1

X-Coordinate	Y-Coordinate
0.23	50
0.8	40
0.2	10
1	0

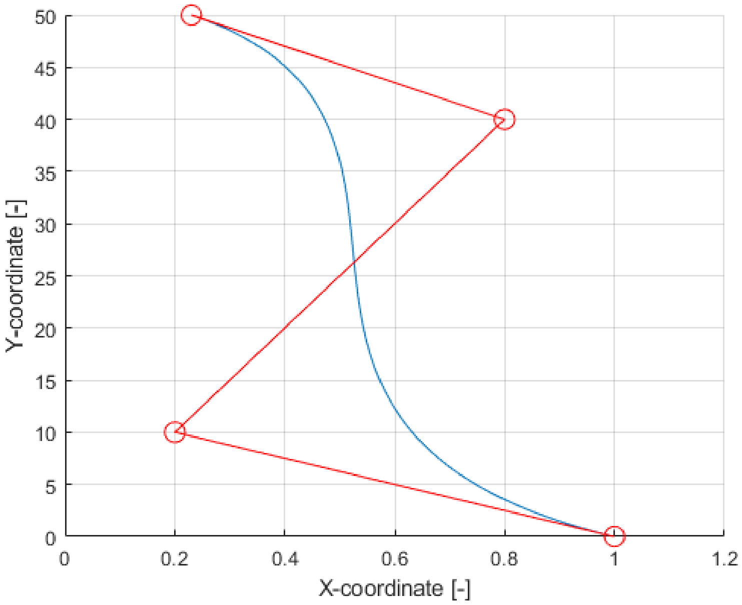

Fig. 4.1 Control points (red) and resulting Bézier curve (blue) based on table 4.1

As one can see, the first and the last control point form the beginning and the end of the Bézier curve, while the other control points serve as poles that pull the curve to a certain direction. The Bézier curve is a weighted sum of the control points P and a set of Bernstein Polynomials B, determined using equation 4.1.

$$P(t) = \sum_{i=0}^{n} P_i B_{n,i}(t) \tag{4.1}$$

The control points P are a set of coordinates on an X-Y grid, and n represents the degree of the curve, which is equal to the amount of control points plus one. The Bernstein polynomials are determined using the equation below. They essentially function as weights for the control points, determining the contribution of each control point to the shape of the curve.

$$B_{n,i}(t) = \begin{bmatrix} n \\ i \end{bmatrix} t^i (1-t)^{n-i}$$

Using the Bézier curve representation, the number of design variables is reduced from 46 to 16, as both the chord and twist distributions are described by 4 control points (with an x and y coordinate each). Four control point are required to describe a cubic curve, which was found to be accurate enough to describe the distributions in this work. After the optimizer adjusts the control points, the resulting Bézier curve is then interpolated at the 23 radial locations at which the TUD-XPROP airfoils are defined, to find the twist angle and chord length relevant for that section, creating a complete set of radially distributed geometric variables that can be used for the performance calculations.

Chapter 5

Aerodynamic Performance Model

In this chapter the aerodynamic performance model is discussed, starting with the reasoning behind the chosen model in section 5.1. Next, the selected model is discussed in detail in section 5.2, including all the relevant performance parameters that are used in the study. The chapter closes with section 5.3, which discusses in detail the aerodynamic model used for the propeller exposed to non-uniform flow.

5.1 Aerodynamic Model Selection

There is a wide variety of models available that are capable of evaluating the aerodynamic performance of a propeller. Because this study uses design optimization methods which rely on a large number of iterations, it was decided early on to focus on low-order numerical models, rather than high-order models such as CFD. This is essentially a trade-off between accuracy and time, for which it was decided that slightly lower accuracy is acceptable for this work such that a larger number of cases can be analysed, and thus a wider design space can be covered. If the results from such a low-fidelity optimization approach are of interest, further analysis can be done by others at a later stage, using more accurate aerodynamic models. Still, a number of low-order models were left to consider. This section will present each model and the trade-off that was made to lead to the selection of the model used in this work.

The aerodynamic models under consideration should have the ability to evaluate the aerodynamic performance of an isolated propeller in a uniform flow. The discussion of the aerodynamic model for the installed propeller (subjected to non-uniform inflow) is discussed later in section 5.3. The most basic aerodynamic model available for this purpose is the actuator disk model. However, since the model does not take into account the specific blade geometry and the specific aerodynamic performance along the blade, which is essential for determining the aeroacoustic performance later on, this model is too simplistic for this work.

Low-order models that do take into account the blade geometry that were considered for this work are the Blade-Element Momentum Model (BEM), a method based on Prandtl's Lifting Line theory, and a Vortex-Lattice Method (VLM). As presented in the work by Branlard et al.[30], the BEM model calculates results in a matter of seconds, while the VLM method and the Lifting

Line method take in the order of minutes. Thus the BEM model is more attractive in terms of computation time. Furthermore, works as those of Gur and Rosen[31] and Dufour[17] show that the results of the BEM model are generally in good agreement with experimental results, especially when tip and hub correction factors are applied. The BEM model does however not include the possibility to account for sweep. A VLM method is more capable of accounting for sweep and more complex 3D shapes. However, since blade sweep has not been not included in this thesis, the blade geometries are not very complex. Combined with the fact that the BEM method is significantly faster compared to the other considered models, this is the method chosen for this work.

5.2 Aerodynamic Performance Prediction Method

This section will discuss the chosen aerodynamic performance model, the Blade Element Momentum Model (BEM), in more detail, as well as the precise implementation of the model in the optimization setup used in this thesis work. First, a the theoretical background of BEM is discussed, and after that the implementation.

5.2.1 The Blade Element Momentum Model (BEM)

The BEM-model is a model that combines two theories, namely the actuator disk theory, also known as the momentum theory, and the blade element theory. Both theories will be briefly discussed here, including their relevant assumptions. The Blade Element Momentum Model implementation used in this work is based on the implementations presented in the work of Liu et al.[32].

Actuator Disk Theory

The actuator-disk model is a basic model, based on momentum theory, that gives some insight into the fundamental relationship between the thrust, shaft power, propulsive efficiency and airspeed when analyzing the propeller aerodynamics. The method is discussed in detail in the textbooks by Ruijgrok[2] and Gudmundsson[33]. For this analysis, the assumption is made that the flow that passes through the propeller forms a well-defined streamtube, as can be seen in figure 5.1. Furthermore, the propeller is represented by an actuator disk, which is where the model gets its name from.

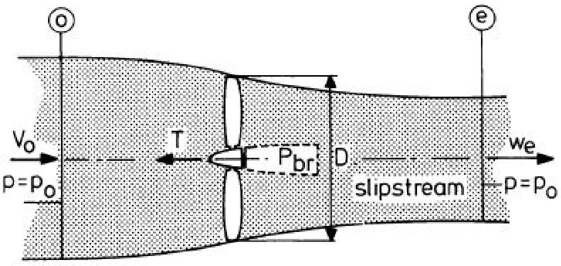

Fig. 5.1 Streamtube as a result of propeller propulsion. [2]

Besides that, a number of other simplifying assumptions are made. Namely:

- The flow is assumed to be incompressible.
- The flow is assumed to be irrotational.
- The flow is assumed to be inviscid.
- The flow is assumed to be steady.
- The pressures and velocities are evenly distributed over the area of the actuator disk.
- Across the disk, the pressure changes discontinuously, but the velocity changes in a continuous sense.

The actuator disk model and its parameters are graphically represented in figure 5.2.

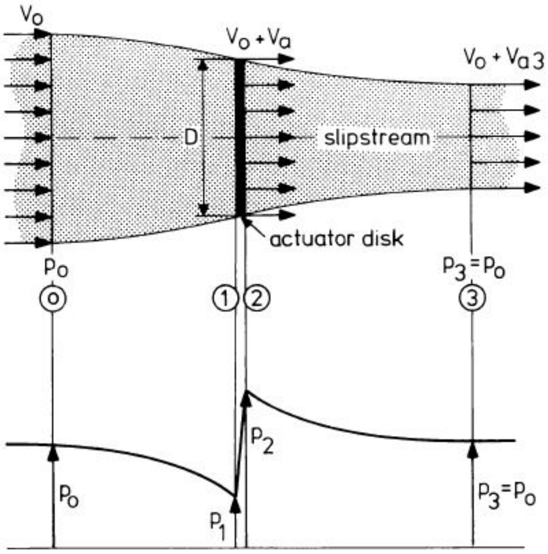

Fig. 5.2 Graphical representation of the streamtube model used for actuator disk theory and the static pressure change along the the streamtube. [2]

Analyzing this figure physically and mathematically, one can derive a set of useful expressions. The most important one for this conversation is shown below. For the full derivation, one is referred to Ruijgrok[2].

$$V_a = \frac{1}{2} V_{a3} \tag{5.1}$$

This expression shows that at the actuator disk the velocity increase is halve the total velocity increase that is obtained at the end of the slipstream. This is an important conclusion that is used in the Blade Element Momentum model.

5.2.2 Blade Element Theory

Instead of looking at the propeller as a disk, Blade Element Theory looks at individual radial sections of the propeller with a certain radial extent dr, and analyzes these separately to come to a total performance picture of the propeller. It is assumed that there are no forces acting in the radial direction (in other words, there are no radial interaction effects), such that each element can be considered individually, and that each element is subjected to a fully two-dimensional flow. The following other assumptions are also made in Blade Element Theory:

- The flow that passes through the propeller is separate from the surrounding air, and forms a streamtube similar to the one shown in figure 5.1.
- The inflow is assumed to be steady, incompressible and inviscid.
- The blade forces generated on an individual element are the only forces that are considered to have an influence on the momentum of the air that passes over that element.

Lastly, in Actuator Disk Theory the assumption is made that there is a uniform velocity and loading over the entire disk. When Actuator Disk Theory and Blade Element Theory are combined in the Blade Element Model, this assumption is no longer valid. Instead, the disk is divided into smaller annuli with radial extent *dr*, and it is assumed that there is uniform loading and uniform velocity in each separate annulus.

Figure 5.3 shows how an element of radial extent *dr* is isolated from a propeller blade to be analyzed separately.

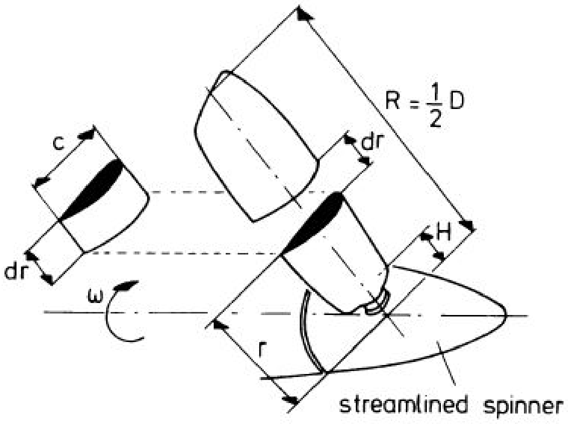

Fig. 5.3 Graphic representation of a blade element, adapted from Ruijgrok. [2]

Taking this approach, each section with length *dr* can be analyzed as an airfoil in 2D. Figure 5.4 shows a blade element in 2D, including relevant forces, velocities and geometric markers.

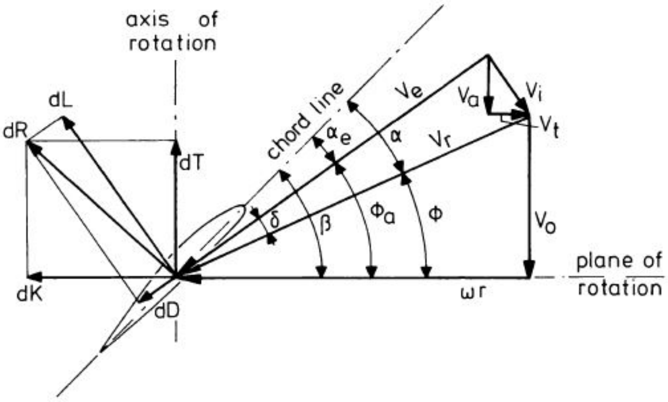

Fig. 5.4 A 2D representation of a blade element, adapted from Ruijgrok. [2]

In this figure, dK refers to the torque force. The initial velocity vector V_r results from the freestream velocity V_0, and the rotational velocity ωr. Due to the influence of the forces produced by the propeller blade, there is an induced velocity V_i present. As a consequence, the resulting velocity vector shifts to the position of V_e, known as the effective velocity. The angle δ is the angle between the initial resulting velocity vector V_r and the final effective velocity vector V_e. As can be seen in the figure, the induced velocity causes the effective velocity to shift, resulting in a lower angle of attack compared to the initial angle of attack occurring at the velocity V_r. The essential objective in the BEM method is to find the effective angle of attack α_e, or the complementary angle ϕ_a for each radial element, such that the aerodynamic forces on that element can be determined. However, this angle is dependent on the induced velocity, the magnitude of which is not known a priori, and needs to be determined iteratively.

This is done by means of a method called the Newton-Raphson method. After this method has found the correct angle and subsequent loading coefficients, the induction factors and non-dimensional thrust and torque can be computed. When these values are known for all radial sections, the aerodynamic performance of the entire propeller can be determined. The whole procedure is schematically shown in figure 5.5. The next subsections will discuss the implementation in more detail.

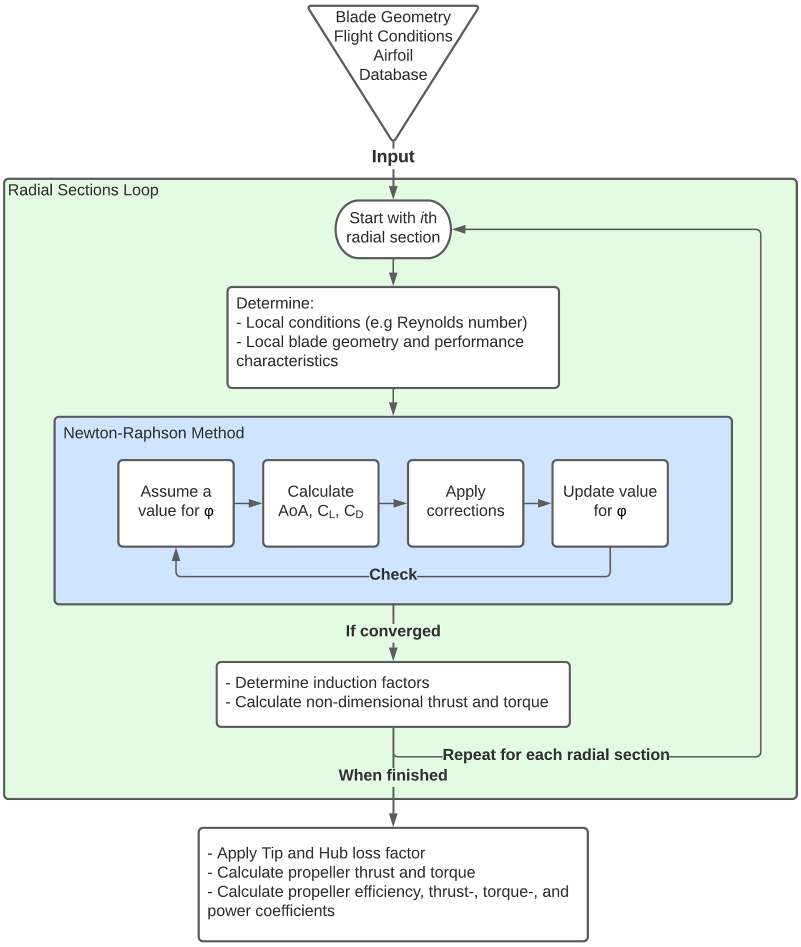

Fig. 5.5 Flow chart of the implemented BEM procedure from input to output.

Step 1: Gathering Initial Data

As can be seen in the figure, the model receives the flight condition (e.g. altitude and flight speed), blade geometry (e.g. airfoil, chord length, twist angle), and airfoil polar database as an input. This airfoil polar database contains the lift, drag, and pressure coefficient data for the TUD-XPROP airfoil, the airfoil used in this study, at a range of Reynolds numbers. It should be noted that the TUD-XPROP has a different airfoil defined at a number of stations along the blade radius. The database had been calculated beforehand for the work of Willemsen[34] using XFOIL. Having the database ready beforehand, compared to performing the airfoil analysis inside the iterative procedure, saves significant computational time. For these airfoil analyses, the N_{crit} was set to 1, and the transition point from laminar to turbulent flow was forced at $x/c = 0.05$, such that the entire airfoil would be subjected to turbulent flow. This was done for two reasons. Firstly such that a better comparison could be made with CFD data. Secondly, it is hard to predict the exact location of transition in the actual propeller analysis, and the blade section analysis used is a 2D analysis, which does not translate well to a 3D situation. As such, an assumption of the transition point simplifies the analysis. Given that the expected operation for which will be optimized is not significantly impacted by possible laminar flow effects at the blade sections that are somehow neglected by this simplification, it is deemed an acceptable one.

Before entering the loop, the propeller blade is divided into 23 radial elements. Within the loop, several performance variables will be calculated for each radial element separately. Using the inputs, the model calculates the rotational speed ω, and the local Reynolds number at every section using equations 5.2 & 5.3. For reference of the angles and velocities used in these equations, one can look at figure 5.4.

$$\omega = 2\pi \frac{V_o}{JD} \tag{5.2}$$

$$Re = \frac{\rho V_r c}{\mu} \tag{5.3}$$

In which μ is the dynamic viscosity of the atmosphere at the flight altitude, and c the local chord length of that element. The velocity V_r is simply calculated with Pythagorean theorem based on figure 5.4. It should be noted that at this point, induced effects are ignored.

$$V_r = \sqrt{(V_o)^2 + (\omega r)^2} \tag{5.4}$$

Furthermore, the solidity σ is calculated using equation 5.5 and the initial angle ϕ using equation 5.6.

$$\sigma = \frac{Bc}{2\pi r} \tag{5.5}$$

$$\phi = \arctan \frac{V_\infty}{\omega r} \tag{5.6}$$

Step 2: The Newton-Raphson Method

The next step in the process is to determine the angle ϕ_a. As mentioned before, due to forces produced by the propeller blade, there is an induced velocity V_i present, which causes the effective velocity V_e to have a different inflow angle than the velocity V_r. To calculate the correct forces produced by the blade section, the angle ϕ_a needs to be found. This can be done using the Newton-Raphson method.

First, the problem has to be stated properly. As mentioned earlier, the BEM model combines Actuator Disk Theory and Blade Element theory. From Actuator Disk Theory the following expressions can be derived for the incremental thrust dT and incremental torque dM ($dM = dK \cdot r$)[35].

$$dT = 4\pi r \rho V_\infty^2 a_a (1 + a_a) dr \tag{5.7}$$

$$dM = 4\pi r^2 \rho V_\infty (2\pi r n) a_t (1 + a_a) dr \tag{5.8}$$

In which a_a and a_t represent the axial and tangential induction factors respectively. For a more detailed derivation, one can refer to the work of Adkins and Liebeck[35] or the book by Ruijgrok[2]. From BEM theory, two different expressions for the incremental thrust and torque can be derived.

$$dT = \frac{1}{2}\rho V^2 \frac{C_l b(1 + a^2)}{\sin^2(\phi)\cos(\gamma)} \sin(\phi + \gamma) dr \tag{5.9}$$

$$dM = \frac{1}{2}\rho V^2 \frac{C_l b(1 + a^2)}{\sin(\phi)\cos(\gamma)} \sin(\phi + \gamma) r dr \tag{5.10}$$

In which the angle ϕ is the angle between dT and dL, and the angle γ is the angle between dL and dR. For the full derivation one can look at the work of Liu et al.[32]. Combining the expressions from both theorems, a new expression can be derived.

$$C_l \sigma = \frac{3\sin(\phi_0 + \phi_i)\tan(\phi_i}{1 - \frac{C_d}{C_l}\tan\phi_i} \tag{5.11}$$

In this equation, there is only one unknown, namely the angle ϕ_i, which is the same angle as the angle δ in figure 5.4. To find this angle, the Newton-Raphson iteration method is used. The equation to be solved is:

$$f(\phi_i) = C_l \sigma - \frac{3\sin(\phi_0 + \phi_i)\tan(\phi_i)}{1 - \frac{C_d}{C_l}\tan\phi_i} = 0 \tag{5.12}$$

At the start, an initial value for ϕ_i is assumed. Next, the local angle of attack is calculated:

$$\alpha = \theta - \phi - \phi_i \tag{5.13}$$

In this equation, the angle θ is equal to the twist angle plus the collective pitch angle, which in combination forms the angle between the plane of rotation and the chord line (see figure 5.4 for reference). With the angle of attack and the previously calculated local Reynolds number, the values for C_l and C_d can be determined based on the airfoil database. After these values have been found, corrections need to be applied. If sweep were to be included, this is where a correction of the loading coefficients C_l and C_d for sweep should be done. In this work, only a Karman-Tsien compressibility correction is applied, to account for compressibility effects, see equation 5.14. It should be noted that in the XFOIL generated airfoil data, compressibility was not taken into account, since it was part of the BEM procedure to do so.

$$C_l = \frac{C_l}{\sqrt{(1-M^2)} + \frac{M^2}{1+\sqrt{1-M^2}} \cdot \frac{C_l}{2}} \tag{5.14}$$

After this correction has been applied to the lift and drag coefficient, all variables are known to update the value of ϕ_i, which is done with the following equation:

$$\phi_{i+1} = \phi_i - \frac{f(\phi_i)}{f^{'}(\phi_i)} \tag{5.15}$$

In which $f^{'}(\phi_i)$ is the derivative of equation 5.12. As can be seen in this equation, when $f(\phi_i)$ approaches zero, the difference between ϕ_i and ϕ_{i+1} approaches zero as well. When the value of $\frac{f(\phi_i)}{f^{'}(\phi_i)}$ passes a certain threshold which is set beforehand, the solution is considered converged. The value of ϕ_i that is found is then used to calculate the actual loads on that respective blade element.

Step 3: Calculating Element and Blade Performance

Knowing the induced angle ϕ_i, the angle ϕ_a can be determined.

$$\phi_a = \phi + \phi_i \tag{5.16}$$

With this angle, the axial induction can be calculated.

$$a = \frac{\tan(\phi_a)(1+\tan(\phi)\tan(\phi_a+\gamma))}{\tan(\phi)(1+\tan(\phi_a)\tan(\phi_a+\gamma))} - 1 \tag{5.17}$$

Using Blade Element theory, one can then calculate the thrust and torque of the blade elements, and integrate them over the blade to calculate the performance of the entire blade.

$$T = \frac{1}{2}\rho V_\infty^2 N_b \int_{r_{hub}}^{R} \frac{C_l b(1+a)^2}{\sin^2(\phi)\cos(\gamma)} \cos(\phi+\gamma) \tag{5.18}$$

$$M = \frac{1}{2}\rho V_\infty^2 N_b \int_{r_{hub}}^{R} \frac{C_l b(1+a)^2}{\sin^2(\phi)\cos(\gamma)} r\sin(\phi+\gamma) \tag{5.19}$$

Before integrating however, first a tip and hub loss correction factor are applied to the list of radial thrust and torque values. These correction factors were formulated by Prandtl[36] to account for the fact that the BEM model originally neglected these loss factors. When included, the BEM model's aerodynamic performance predictions are much more in line with experimental results. To calculate the tip and hub loss factors, first the variable f has to be calculated.

$$f_{tip} = \frac{B}{2}\frac{R-r}{r\sin\phi} \tag{5.20}$$

$$f_{hub} = \frac{B}{2}\frac{r - r_{hub}}{r \sin\phi} \tag{5.21}$$

When both the tip and hub loss factor have to be taken into account, the variables f are multiplied.

$$f = f_{tip} \cdot f_{hub} \tag{5.22}$$

The final tip and hub loss factor is calculated as follows.

$$F = \frac{2}{\pi}\cos^{-1}\left(e^{-f}\right) \tag{5.23}$$

As can be seen, the variables f are a function of the radial position r. The correction factor thus differs for each radial element, and is therefore applied before integration.

Once the thrust and torque are known, the propeller efficiency and loading coefficients, which form the final output of the BEM model, are calculated as follows.

$$C_T = \frac{T}{\rho_\infty n^2 D^4} \tag{5.24}$$

$$C_Q = \frac{Q}{\rho_\infty n^2 D^5} \tag{5.25}$$

$$C_P = \frac{2\pi Q}{\rho_\infty n^3 D^5} \tag{5.26}$$

$$\eta = J\frac{C_T}{C_P} \tag{5.27}$$

Additional Calculations

Although not directly relevant for the optimization, additional performance parameters can be calculated from the BEM model that can provide a deeper insight into the aerodynamic performance of the propeller, which comes in useful when explaining the results later on. The total efficiency η can be split into profile and induced efficiency, according to a method present by Drela in the QPROP Formulation[37].

$$\eta = \eta_{ind}\eta_{prof} \tag{5.28}$$

In which the induced efficiency can be calculated as follows:

$$\eta_{ind} = \frac{1 - a_t}{1 + a_{ax}} \tag{5.29}$$

These parameters a are the axial and tangential induction factors, determined in the BEM calculation procedure. The formula for the axial induction factor was already presented in equation 5.17. The tangential induction factor can be determined with the following equation:

$$a_t = a_{ax} \cdot \tan(\phi_0) \cdot \tan(\phi + \gamma) \tag{5.30}$$

$$\gamma = \arctan \frac{c_d}{c_l} \tag{5.31}$$

With the induced and total efficiency known, the profile efficiency is easily found by rewriting equation 5.28. However, to better understand what the profile efficiency refers to, it is helpful to give its full equation as well (see equation 5.32)[37].

$$\eta_{prof} = \frac{1 - \frac{c_d}{c_l}\frac{V_a}{V_t}}{1 + \frac{c_d}{c_l}\frac{V_t}{V_a}} \tag{5.32}$$

In which V_a refers to the axial velocity, which is equal to the freestream velocity, and V_t to the tangential velocity, which is equal to the rotational velocity Ωr.

Another useful metric often used in discussions regarding propeller design and performance is the solidity. The solidity can be defined as the ratio between the area of propeller disk that when viewed from the front is solid (the blades) and the area in between the blades. In this study, propeller designs with 3-6 blade counts are studied. To compare these propellers, it can be more insightful to look at the solidity instead of the chord distribution of the blades. Because although chord length could decrease for a propeller with a higher blade count, its solidity might be the same as a propeller with a lower blade count and wider blades. The solidity σ can be calculated as follows[1].

$$\sigma = \frac{4B}{3\pi}\left(\frac{\bar{c_b}}{D}\right) \tag{5.33}$$

In which B is the number of blades, and $\bar{c_b}$ is the average chord length of the blade.

5.3 Aerodynamic Performance Model in Non-Uniform Flow

The BEM model analyzes the aerodynamic performance for an isolated propeller operating in a uniform flow. When the propeller is installed on the aircraft however, it will experience different forms of non-uniform flow. A separate aerodynamic model is required to calculate the aerodynamic performance characteristics in this situation. Such a method was proposed in literature by van Arnhem[5], and this is the method chosen to be used in this work. Several reasons led to this decision. To begin, the method is relatively simple and fast, which makes it a great model for the implementation in an optimization framework. Secondly, the propeller used in the published results was a version of the TUD-XPROP, the base propeller design used in this work as well, which made verification of the implemented model much easier. On top of that, the non-uniform inflow data used in the paper was also available to the author, which made verification of the method very easy. Finally, the method showed great accuracy in comparison with higher-fidelity CFD data[5]. With these facts being known in the early stages of the project, no other models were explored that analyze the aerodynamic performance of a propeller operating in a non-uniform flow.

The rest of this section will discuss the model in more detail.

In the paper by van Arnhem it is assumed that the propeller performance of the isolated propeller in uniform flow and the non-uniform propeller inflow field are known in advance. In this study, the isolated propeller performance is calculated using the BEM model. Since the propeller blade will experience a range of advance ratios as a result of the non-uniform inflow, the BEM model runs for a range of advance ratios, creating a grid of aerodynamic data of the propeller operating in uniform flow. This data is then fed to the non-uniform flow model.

In the study by van Arnhem, the propeller inflow field and the propeller performance in isolated and installed condition are determined by CFD, and an experiment was performed as a means of validation. This experimental data is subsequently also used as a means to validate the proposed method. The same inflow data used in this publication was made available to be used for this work by the authors.

The method mainly rests on the assumption that a change in local advance ratio $\Delta J'$ at the location r/R_p, and at a certain azimuthal angle ϕ, results in a local change in loads $C_T^{'}$ and $C_Q^{'}$. As a result an induced velocity field with a magnitude equal to $\Delta J'$ is applied to the full propeller disk as $\Delta J = \Delta J'(r, \phi)$. The prime in this case indicates a local quantity on the propeller disk defined by its azimuthal and radial position. A number of other assumptions are made as well, amongst which are:

- The redistribution of loading due to shed vorticity induced upwash or downwash on adjacent sections is assumed to be a second-order effect, and is thus neglected.
- For the quasi-steady solution it is assumed that a blade response to a disturbance is confined to the same azimuthal angle at which the disturbance is encountered by the blade. An analysis of the full annulus, which would require considerable computational effort, is thereby avoided.

What follows will be a condensed walkthrough of the method. The paper itself can be consulted for more in-depth details about the assumptions and their motivations as well as the development and validation of the method.[5]

The proposed approach treats the propeller load distribution as linear superposition of the response to in-plane and out-of-plane disturbances, which is permissible as long as the disturbances are small. The out-of-plane disturbance is defined as Δu, while the in-plane disturbances are defined as Δv and Δw. The reason the in-plane and out-of-plane disturbances are treated separately is that give an insight into each of their relative contributions. These disturbances can be obtained from the non-uniform inflow data that was generated by means of CFD, and can be used to calculate the effective axial and tangential advance ratio as follows:

$$J_{eff,axial}(r, \phi) = \frac{\Delta u(r, \phi)}{nD_P} + \frac{V_\infty}{nD_P} \tag{5.34}$$

$$J_{eff,tangential}(r, \phi) = \frac{V_\infty}{[n + \Delta V_t / 2\pi r] D_P} + \frac{V_\infty}{nD_P} \tag{5.35}$$

With ΔV_t being defined as:

$$\Delta V_t = -\Delta v \cos\phi - \Delta w \sin\phi \tag{5.36}$$

In which ϕ is the local phase angle. To clarify these terms, the coordinate system used is show in figure 5.6. In this coordinate system, the velocities u, v, and w correspond with the axes x, y, and z respectively.

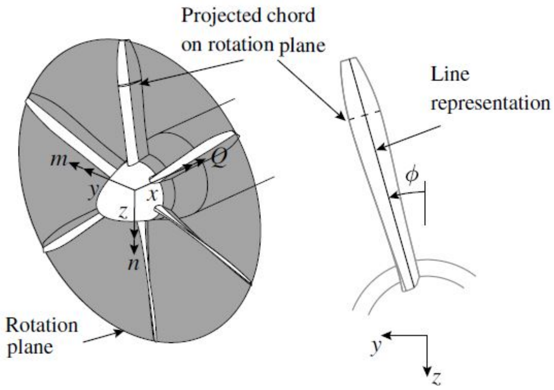

Fig. 5.6 Definition of the propeller rotation plane on which the inflow is determined and its axis system. [5]

Using these effective advance ratios, the corresponding changes in the local thrust and torque can be calculated. This is again done separately for the axial and tangential situation. The full equations for this procedure can be found in the paper. Once these are known, they can be summed to compute the total change in normalize propeller loading at a particular blade section (r,ϕ):

$$\Delta C_T^{'}(r,\phi) = \frac{\Delta T_a^{'} + \Delta T_t^{'}}{\rho_\infty n^2 D_p^4} \tag{5.37}$$

$$\Delta C_Q^{'}(r,\phi) = \frac{\Delta Q_a^{'} + \Delta Q_t^{'}}{\rho_\infty n^2 D_p^5} \tag{5.38}$$

When the load distribution is found for the propeller blades at each phase angle, the integral propeller forces can be computed by integration. With the results the change in the propeller efficiency can also be calculated.

$$\Delta\eta_p = \frac{(\Delta T + T_\infty)}{(\Delta P_s + P_{s_\infty})} V_\infty - \frac{T_\infty}{P_{s_\infty}} V_\infty \tag{5.39}$$

Up to this point, the method was developed using a quasi-steady assumption. However, a correction for unsteady effects was later included in the model. It was shown by Sears[38], that a downwash is induced by the bound and wake vorticity at the leading edge of a two-dimensional airfoil, which reduces the section lift coefficient and introduces a phase difference between the unsteady motion of the inflow and the response to the disturbance. For an accurate prediction, it is important to account for these unsteady effects. In the presented approach this is done in the following way: the quasi-steady thrust and torque forces are transformed to the frequency domain and multiplied with the Sears function to account for the unsteady effects. Furthermore, a compressibility correction is applied to the reduced frequency based on literature[39]. More details on the procedure and the full equations can be found in the paper[5].

Besides the aforementioned assumptions, there are another two caveats that should be mentioned regarding this method. The first one is that the proposed method becomes less suitable with increasing blade sweep angles, as an increase in sweep angle will lead to a more pronounced coupling between adjacent sections along the radius. This coupling is currently assumed not to be there. Since blade sweep is not considered in this work, this is not an issue. However, future authors should be mindful of this. Furthermore, the proposed method evaluates the inflow along a line that describes the propeller blade, passing the infinitely think disk only at one point rather than over the entire chord. The representation of the inflow could therefore possibly be improved if the inflow at location (r, ϕ) would be determined using a weighted velocity along the projected chord in the plane of rotation. However, it is deemed that this assumption does not have a significant effect on the results presented in this work.

The method was validated by comparison to CFD and experiment for four different cases of non-uniform inflow, namely an angle of attack, wake encounter, over-the-wing propeller, and wingtip-mounted pusher propeller. The comparison with validation data was considered acceptable for this study. More on the verification and validation of this model can be found in chapter 8.

Chapter 6

Aeroaocustic Performance Model

This chapter introduces the aeroacoustic performance model used in this work. Just like the last chapter, the first section starts with a brief summary of the relevant theory and the motivation behind the aeroacoustic model chosen for this work. After that, section 6.2 will discuss the exact implementation of the aeroacoustic model for this work, both in isolated and installed conditions.

6.1 Aeroaocustic Model Selection

As was the case for the aerodynamic model, there are multiple models available for aeroacoustic performance analysis of a propeller. Similar selection criteria compared to the selection criteria for the aerodynamic model are also relevant, namely the accuracy of the model, and the computational effort required to obtain results. Furthermore, since this thesis work will take into account installation effects, the model has to be able to model the aeroacoustic effects as a result of uniform and non-uniform flow.

As has been mentioned previously (in section 2.2), it has been established that harmonic noise is generally more relevant than broadband noise when it comes to the analysis of propeller noise. As such, the prediction methods that will be discussed and used for the remainder of this thesis only consider tonal noise sources, and the broadband component will be ignored. The majority of the noise prediction methods that are in use nowadays are based on the Ffowcs-Williams and Hawkings equation[3]. Equation 6.1 shows the linear form of the Ffowcs-Williams/Hawkings equation, which is the relevant form that is considered in this work. In this form of the equation, the quadrupole source term is not shown. This is a non-linear source, which will not be considered in this work.

$$\nabla^2 p - \frac{1}{c^2}\frac{\partial^2 p}{\partial t^2} = -\frac{\partial}{\partial t}[\rho_0 v_n |\nabla f| \delta(f)] + \frac{\partial}{\partial x_i}[l_i |\nabla f| \delta(f)] \tag{6.1}$$

On the left hand side of this equation, one can see the linear wave operator acting on the acoustic pressure p. The right hand side of the equation contains two elements. The first element represents the thickness noise, and the second element represents the loading noise. Within this equation, c is the ambient speed of sound, ρ_0 is the ambient density, v_n represents the local velocity of the surface normal to itself, $\delta(f)$ is the Dirac-delta function, x_i the position of the observer, and l_i is the ith component of the surface force. The variable f represents the presence of the surfaces, with $f = 0$

being equal to the equation of the blade surface. However, unless high frequencies are considered at which the wavelengths become the of the same order as the blade thickness, the details of the airfoil section can generally be ignored, which allows a simplification of equation 6.1 shown in equation 6.2[3]. The models that have been developed to solve this equation are divided into two categories, frequency domain methods, and time domain methods.

$$\nabla^2 p - \frac{1}{c^2}\frac{\partial^2 p}{\partial t^2} = -\rho_0 \frac{\partial q}{\partial t} + \nabla \cdot \bar{F} \tag{6.2}$$

6.1.1 Time-Domain Methods

When using time-domain methods, equation 6.1 is solved directly in terms of space-time variables. Farassat[40][41] has been the main proponent of this method, and developed it extensively. The outcome of this method is a prediction of the acoustic pressure waveform $p(t)$. To get to this outcome, one must determine where every element of surface was at the moment it emitted the soundwaves that are registered by the observer at point t. A reconstruction of the planform surface by connecting all the blade edges at their retarded times is known as the "acoustic planform", and this phenomenon plays a key role in the method. The appeal of this method is that it can treat the blade geometry with any desired level of precision, as opposed to the frequency-domain methods. However, the method is generally much more computationally expensive. Several formulations have been derived[42], of which the Farassat 1A model is frequently used in propeller optimization studies. Nevertheless, the implementation is less suitable for an optimization study within the given timeframe of the thesis due to its complexity and higher computational cost compared to the frequency domain methods which will be discussed next. Therefore, this and other time-domain methods were not considered further. For a more in-depth discussion of this method it is recommended to take a look at the work of Farassat[40][41] and Hanson[43].

6.1.2 Frequency-Domain Methods

In the frequency domain, it is no longer necessary to compute the retarded blade locations, which gives an advantage to this method in terms of computational load. A possible downside of frequency-domain methods is that the simplification of the blade geometry (see *Thin Blade Assumption* in section 6.2 could lead to a loss in precision. However, this simplification was found to be reasonably accurate in the far-field[3]. A number of frequency-domain methods have been developed over the years. Perhaps the first successful one was developed by Gutin[44]. However, this model did not account for the effects of either forward flight or non-compactness. The theory was later extended by Hanson, who did include the effects of non-compactness, sweep, and non-axial flow[3].

A study by Kotwicz Herniczek et al.[20] compared several acoustic frequency-domain methods, including the model by Hanson. Each method was compared to 14 test cases that originated from nine separate experimental studies. In these studies, a wide range of propeller geometries, blade numbers, microphone locations, tip speeds and forward Mach numbers were considered. The model by Hanson was found to be the most accurate in this comparative study with an average error of 5.9 dB, and the authors noted that the acoustic models demonstrated reasonable agreement with the experimental data. Although the average error of 5.9 dB is not insignificant, the model is suitable for predicting trends and making initial estimations in the early stages of design. The model also has a relatively low computational cost, and can be adapted for non-uniform inflow, as demonstrated in other papers by Hanson and Magliozzi[3][14]. For this reason, Hanson's Helicoidal Surface Theory[15] was chosen for this thesis project.

6.2 Aeroaocustic Performance Prediction Method

This section will discuss the chosen aeroacoustic method in more detail, as well as the exact implementation for this work. It is important to note that Hanson's Helicoidal Surface Theory only applies in the far field. Findings in the Hanson study[15] pose that reasonably accurate predictions can be made up to about one propeller diameter distance from the propeller. For this work however, the noise will be modeled as observed from the ground when the noise source is either in climb or cruise (at a certain altitude), and therefore near-field predictions are not relevant to discuss. Two other assumptions that are made in this theory are:

- Thin Blade Assumption: The noise sources are assumed to act on the mean surface of the blade instead of the blade's upper and lower surfaces. Given that the method is used to predict noise levels in the far field, the distance between the upper and lower surface is negligibly small compared to the distance between the blade and the observer. Therefore this assumptions is deemed valid in this case.
- Non-linear effects due to Mach numbers above $M = 1$ at the local blade section are neglected. This is a reasonable assumption since these Mach numbers generally do not exceed $M = 0.7$ in this study.

In the Helicoidal Surface Theory, three forms of noise are calculated, each represented by a separate Fourier coefficient as shown in equation 6.3. The first component P_{Vm} is the thickness noise component, which is the noise caused due to volume displacement. The second and third components, P_{Dm} and P_{Lm} are the loading noise components, caused by the drag and lift forces.

$$P_{mB} = P_{Vm} + P_{Dm} + P_{Lm} \tag{6.3}$$

These different components can be calculated by means of the large equation presented below. For the full derivation of this formula, the reader is referred to the works of Hanson and Magliozzi[15][3].

$$\begin{bmatrix} P_{Vm} \\ P_{Dm} \\ P_{Lm} \end{bmatrix} = -\frac{\rho_0 c_0^2 B \sin\theta e^{imB\left(\frac{\Omega r}{c_0} - \frac{\pi}{2}\right)}}{8\pi(y/D)(1 - M_x\cos\theta)} \times \int_{root}^{tip} M_r^2 e^{i(\phi_s + \phi_o)} J_{mB}\left(\frac{mBzM_t}{1 - M_x\cos\theta}\right) \begin{bmatrix} k_x^2 t_b \Psi_V(k_x) \\ ik_x(c_D/2)\Psi_D(k_x) \\ -ik_y(c_L/2)\Psi_L(k_x) \end{bmatrix} dz$$

ρ_0 = free-stream air density
c_0 = speed of sound
B = number of propeller blades
θ = radiation angle from propeller axis to observer point
m = harmonic of blade passing frequency
Ω = angular speed propeller
r = radial coordinate
y = observer distance from propeller axis
D = propeller diameter
M_x = free-stream Mach number
M_r = relative Mach number of the radial section
M_t = tip Mach number
ϕ_s = phase delay due to sweep
ϕ_o = phase delay due to lean
J_{mB} = Bessel's function of the first kind with order $m \cdot B$
k_x = chordwise wave number
k_y = thickness wave number
C_l = lift coefficient of radial section
C_d = drag coefficient of radial section
t_b = maximum thickness-to-chord ratio of radial section
Ψ_V, Ψ_D, Ψ_L = normalized source transforms
z = radial coordinate

A few parameters are of note here. As stated, the angle θ is the angle between the propeller axis and the observer point. A graphical representation of how the angle θ is measured can be seen in figure 6.1. In this figure two propellers are shown, but for a single propeller setup only the rear propeller (propeller 2) is relevant. The parameter r_1 in this figure is equal to the parameter y in equation 6.2.

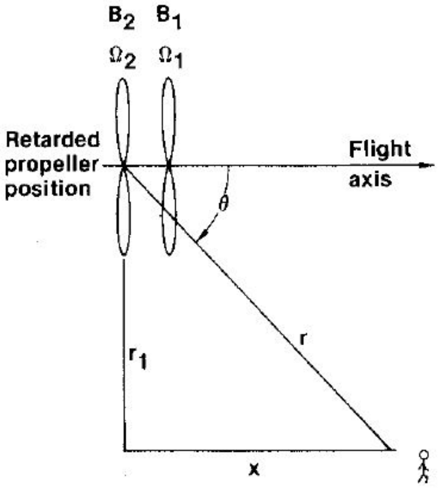

Fig. 6.1 Schematic of observer angle θ for a double propeller set-up.[14]

Given this definition of the angle θ, one can see only a certain range of angles is relevant for analysis when the objective is to minimize the noise for observants on the ground in a situation where the aircraft is overhead. In this thesis work, it was decided to focus on the range between 60 and 120 degrees. The distance r between the noise source and the observer can simply be calculated with trigonometry.

$$r = \frac{r_1}{\sin\theta} \tag{6.4}$$

The next parameters of notice are the phase delay factors ϕ_s and ϕ_o. Their definitions are given in equations 6.5 & 6.6.

$$\phi_s = \frac{2mBM_t}{M_r(1 - M_x\cos(\theta))}\frac{MCA}{D} \tag{6.5}$$

$$\phi_o = \frac{2mB}{zM_r}\left(\frac{M_r^2\cos(\theta) - M_x}{1 - M_x\cos(\theta)}\right)\frac{FA}{D} \tag{6.6}$$

In which *MCA* stands for the Mid-Chord Alignment, which is another way of expressing sweep, and *FA* for Face Alignment, the definition of which can be seen in figure 6.2.

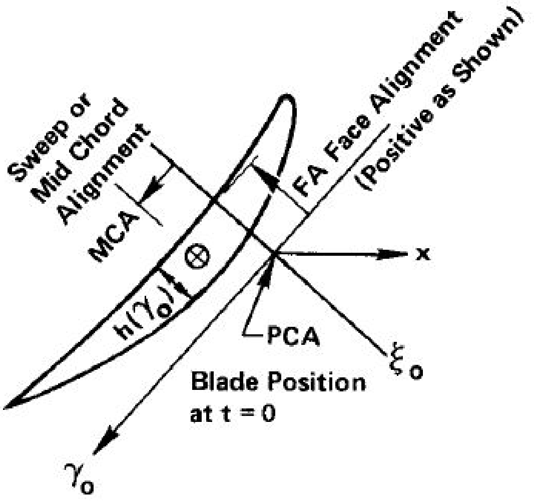

Fig. 6.2 Schematic showing the geometric definitions of *MCA* and *FA*.[15]

As mentioned before, sweep is not considered in this work, and as such *MCA* and ϕ_s are by definition always equal to zero. Furthermore, *FA* is set to be zero, and also not further considered in this work, resulting in ϕ_o being equal to zero at all times.

The parameter J_{mB} is a Bessel's function of the firs kind with the order $m \cdot B$, and with the argument between the brackets. The Bessel's function characterises the radiation efficiency of the sound-waves. Given its dependency on $\cos\theta$, the parameter causes the noise to diminish steeply near 0 and 180 degrees.

The last parameters of note are wave numbers k_x and k_y, as well as the normalized source transforms Ψ_V, Ψ_D, Ψ_L. The wave numbers k_x and k_y are defined as follows:

$$k_x = \frac{2mBB_D M_t}{M_r(1-M_x\cos\theta)} \tag{6.7}$$

$$k_y = \frac{2mBB_D}{zM_r}\left(\frac{M_r^2\cos\theta - M_x}{1-M_x\cos\theta}\right) \tag{6.8}$$

In which B_D is the chord-to-diameter ratio. The source transforms are defined as follows:

$$\begin{bmatrix} \psi_V(k_x) \\ \psi_D(k_x) \\ \psi_L(k_x) \end{bmatrix} = \int_{-\frac{1}{2}}^{\frac{1}{2}} \begin{bmatrix} H(x) \\ f_D(x) \\ f_L(x) \end{bmatrix} e^{ik_x x} dz \tag{6.9}$$

In this formulation, the shape function $H(x)$ represents the sectional thickness distribution, which is normalised such that the maximum thickness is equal to one. An example of the shape function $H(x)$ can be seen in figure 6.3.

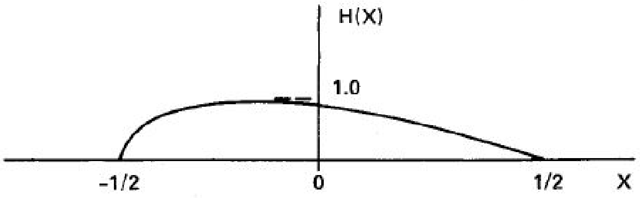

Fig. 6.3 Normalized thickness distribution.[15]

This thickness distribution is determined based on the airfoil shape. Besides the sectional thickness distribution $H(x)$, the chordwise lift and drag distributions ($f_L(x)$ and $f_D(x)$) also need to be determined for each section. These distributions are computed using polar data from the airfoil database. This database contains a pressure distribution for each radial section at a range of Reynolds numbers and angles of attack. The noise model receives as an input the aerodynamic performance characteristics generated by the BEM model, which contains the relevant angle of attack for each radial section. The Reynolds number can be calculated with the velocity of the incoming flow at the radial section, the chord length of that radial section, and the atmospheric parameters at the operating altitude. With the relevant pressure distribution known, the lift and drag shape functions can be determined. Given that only the pressure distribution data is used to determine these distributions, it is assumed that the shear stress contribution can be neglected. It should be noted that this assumption is only made for the chordwise distribution. The integrated value contains all contributions, including the chordwise distribution. The shape functions $f_L(x)$ and $f_D(x)$ are subsequently normalised such that each function integrates to unity.

Now all parameters are known, the individual Fourier coefficients for thickness and loading noise can be computed. The Fourier coefficients are then added up (see equation 6.3) and transformed to the time domain using either equation 6.10 or equation 6.11, depending on whether the signal is symmetric or not.

$$p(t) = 2\mathrm{Re}\sum_{m=1}^{\infty} P_{mB}e^{-imB\Omega t} \tag{6.10}$$

$$p(t) = \sum_{m=-\infty}^{\infty} P_{mB}e^{-imB\Omega t} \tag{6.11}$$

With the time-dependent acoustic pressure known, the root-mean squared acoustic pressure can be determined using equation 6.12. This pressure is subsequently used to determine the acoustic performance in decibels, either with respect to a reference pressure (equation 6.13) or normalised with respect to the propeller thrust and diameter (equation 6.14). For more background on these equations one is referred back to section 2.2.

$$p_{rms} = \sqrt{\frac{1}{2T}\int_{-T}^{T}(p(t)-p_0)^2 dt} \tag{6.12}$$

$$SPL = 20\log_{10}(p_{rms}/p_{ref}) \tag{6.13}$$

$$TSSP = 20\log_{10}(p_{rms}\cdot\frac{D^2}{T}) \tag{6.14}$$

These values are the final outputs of the aeroacoustic model. Since the noise is measured at several observer angles θ and several observer distances r, the average of the noise values found in this range of angles is used in the optimization objective. To calculate this average correctly, the average of the root-mean-square acoustic pressure values is calculated first, after which this value is used in the logarithmic operations in the SPL and $TSSP$ equations.

If the propeller is subjected to a non-uniform inflow, a number of adjustments need to be made to Hanson's model in order to compute the aeroacoustic performance correctly. These adjustments will be discussed next.

Aeroacoustic Performance Prediction in Non-Uniform Flow

An important noise-generating mechanism in propeller aeroacoustics is linked to the change in blade loading during the blade's rotation. Therefore, one can imagine that when the propeller is exposed to a non-uniform inflow more noise is generated compared to when the propeller is operating in isolation exposed to a uniform inflow. A non-uniform inflow will result in non-uniform loading during the rotation of the blade, sometimes with large gradients and amplitudes, depending on the type of disturbance. To capture the effects of non-uniform flow on the aeroacoustic performance, Hanson expanded the theory discussed in the previous section. In a paper on the noise of counter-rotation propellers[14], an adaptation of equation 6.2 is discussed. A case in which a single propeller is operating in a fixed inflow distortion is equivalent to a double propeller layout in which the front propeller is stationary and distorting the inflow of the rear propeller. The latter situation is one of the cases discussed in the paper by Hanson[14], and can therefore be applied in this work. The equation for this case, which is an adaptation of equation 6.2, can be seen below. It should be noted that this formulation only considers the loading sources.

$$p(t) = -\frac{\rho_0 c_0^2 B \sin\theta}{8\pi(y/D)(1-M_x\cos\theta)} \sum_{m=-\infty}^{\infty} \sum_{k=-\infty}^{\infty} \exp\left\{ i\left[(mB-k)B\left(\phi - \phi^{(2)} - \frac{\pi}{2}\right) + mB\left(\frac{r}{c_0} - \Omega t\right)\right]\right\}$$
$$\times \int_{root}^{tip} M_r^2 e^{i(\phi_s+\phi_o)} J_{mB-k}\left(\frac{mBzM_t}{1-M_r\cos\theta}\right)\left[k_x \frac{C_d}{2}\Psi_{Dk}(k_x) + k_y \frac{C_l}{2}\Psi_{Lk}(k_x)\right] dz$$

This equation will calculate the time-dependent acoustic pressure of the propeller subjected to a non-uniform inflow. It does not matter for this equation whether the inflow is distorted due to a stationary propeller in front of the operating propeller, or due to the fact that it is installed on an aircraft. As such, this equation is useful for this work, in which a single propeller is examined that is exposed to a non-uniform inflow as a result of installation on an aircraft.

A few differences between the equation above and its steady version (equation 6.2) are of note, and will be discussed next. To begin, the equation is already formulated in the time domain, which means that the step described by equation 6.11 is already incorporated in the formulation. It should be noted that this is simply a choice of formulation, as both equations can be written in the frequency- and the time-domain. Furthermore, as mentioned, the equation only considers the loading sources, and as such the volume component is absent from the equation. This component is not neglected in the computation of the noise, but remains unchanged compared to the steady formulation, and is added when the complete aeroacoustic performance is calculated.

The next few differences are more specific differences introduced to account for unsteady effects. To begin, one can see that in addition to harmonics m, another set of harmonics k have been introduced. While the harmonics m are known as the sound harmonics, the harmonics k are known as the loading harmonics. Since the propeller is now subjected to unsteady loading, the loading coefficients C_l and C_d are now also expanded in harmonic form as follows:

$$C_l = \sum_{k=-\infty}^{\infty} C_{lk} \exp(-i\omega_k t) \tag{6.15}$$

In this formulation, the variable ω_k is equal to $\omega_k = k\Omega$[3]. A similar expression exists for C_d. This equation gives the loading history experienced by a propeller blade during its revolution in terms of the lift or drag harmonics C_{lk} and C_{dk}. In this summation, $k = 1$ corresponds to the fundamental frequency, while $k = 0$ is identical to the steady loading as used in equation 6.2. The number of harmonics m and k that are required to get an accurate result is something that will be discussed later in chapter 8. With the introduction of k, some other elements of the equation are also slightly altered. While the observed frequencies are still multiples of the BPF, the mode orders were found to be $mB-k$[14]. Therefore, the order of the Bessel's equation J is now equal to $mB-k$ instead of mB. This factor $mB-k$ also makes its appearance in the first exponent.

A new angle is also introduced, in the equation denoted by $\phi - \phi^{(2)}$. In this notation, the angle $\phi^{(2)}$ represents the blade location at $t = 0$, while the angle ϕ itself is an observer angle, defining the angle between the propeller axis and the observer in a different plane compared to the angle θ. The definition of observer angle ϕ can be seen in figure 6.4.

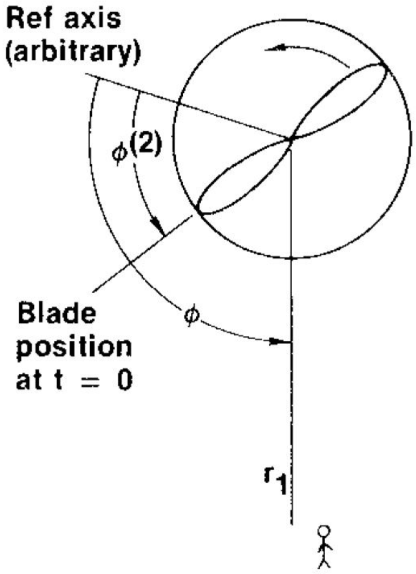

Fig. 6.4 Schematic showing the geometric definition of ϕ and $\phi^{(2)}$ with respect to the propeller. [14]

In this work, both the reference axis and the blade position at $t = 0$ are chosen to be straight up, such that $\phi^{(2)} = 0°$ and $\phi - \phi^{(2)} = 180°$ when r_1 is straight down. Since there are two observation angles at play now, the distance r has to be calculated differently. Using trigonemetry, the following expression is derived for the distance r between the noise source and the observer at an arbitrary angle θ and ϕ.

$$r = \sqrt{y^2 + \left(\sqrt{(\frac{y}{\tan\theta})^2 + (y\tan\phi)^2)}\right)^2} \tag{6.16}$$

Since this work is only concerned with the noise experienced by an observer on the ground in a certain area below the noise source, it was chosen to only consider the angle ϕ in a range of 150 to 210 degrees.

Lastly, there is a change in the equations for k_x and k_y.

$$k_x = \frac{2M_t}{M_r}\left[\frac{mB}{1 - M_x\cos\theta} - k\right]B_D \tag{6.17}$$

$$k_y = \frac{-2}{z_0 M_r}\left[\frac{mB(M_r^2\cos\theta - M_x)}{1 - M_x\cos\theta} + kM_x\right]B_D \tag{6.18}$$

The equations for ϕ_o and ϕ_s also change, but remain zero in this work due to their dependency on MCA and FA. Their formulations can be found in the work of Hanson[14]. With all the parameters known, the time-dependent acoustic pressure can be calculated. Similar to the steady case, the root-mean square pressure is determined for each of the analyzed angle combinations θ and ϕ. The mean value of these root-mean square pressure values is subsequently used to calculate the mean TSSP, which forms the optimization objective.

Chapter 7

Propeller Design Optimization Setup

This chapter will discuss the design optimization setup. In the optimization setup, all of the previously discussed models are combined such that an automatic optimization workflow can be realized that optimizes a propeller geometry for a given objective. The discussion of the setup is divided over several sections, each discussing a separate key element of the entire setup, starting with the objective function, in section 7.2. Section 7.3 discusses the design variables used in this study and their bounds, followed by section 7.4 which discusses the constraints and the conditions for convergence. In section 7.5 the optimization algorithm that was used in this work is discussed and the chapter conclude with the complete and final definition of the optimization setup, presented in section 7.6.

7.1 Optimization Problem Definition

Whether an optimization study is successful and delivers valuable results does not just depend on the models used. The setup itself is also of vital importance. The objective of the optimization, the design variables and their bounds, the constraints, the optimization algorithm, and the convergence conditions all play a role. This section will discuss each of these elements of the optimization setup, and the considerations behind their choice.

The first step in designing the optimization workflow is connecting all the models together, such that a propeller geometry can serve as an input for the model, and the model will return key aerodynamic and aeroacoustic performance indicators. An overview of the entire optimization workflow can be seen in appendix A.

The optimization works as follows. First, a baseline propeller design is fed to the workflow, and its key performance indicators are determined, which serve as a baseline throughout the optimization process. This means that for every new design that is proposed by the optimization model, the performance of this new design is compared to the performance of the baseline design. Next, a randomized initial design is fed to the model. The randomized design variables of this design are within the range specified by the author (see 7.3). The key performance indicators of this randomized design are then compared to the baseline design. Furthermore, it is determined whether this random design satisfies all the constraints (discussed later in 7.4). Based on this information, the performance of the design compared to a baseline, and the severity of the constraint violation, the optimization algorithm will search for a better performing design with a lower or no constraint violation. This cycle continues until no significant improvement can be found for any possible change in the design variables. The range in which the optimization algorithm is allowed to change the design variables is specified beforehand. Whether this final result is a feasible result or not depends on the constraint violation, which has to be below a threshold that is specified beforehand as well. If no feasible result is found, the entire process will be repeated with a different initial random design. Next, a number of elements of this setup will be discussed in more detail.

7.2 Objective Function

The goal of the optimization algorithm is to minimize the objective function. The definition of this function is thus of vital importance for the outcome of the study. As stated numerous times already, the aim of this work is to optimize for both aerodynamic and aeroacoustic performance. The key performance indicators that need to be optimized for in the light of these two objectives are the propeller efficiency η and the Thrust Specific Sound Pressure (TSSP).

$$\eta_p = J\frac{C_T}{C_P} \tag{7.1}$$

$$TSSP = 20\log_{10}\left(p_{rms}\cdot\frac{D^2}{T}\right) \tag{7.2}$$

As discussed earlier as well, the TSSP in this study is measured over a range of angles. The final value of the TSSP which the optimization algorithm aims to minimize is the TSSP, which is found using the average RMS pressure over this range of angles. In this study, the range of angles chosen is $\theta = [60°, 90°, 120°]$, which is applicable for both the steady and the unsteady analysis. In the unsteady analysis, the noise also varies with an additional observer angle ϕ, for which the range of angles was chosen to be $\phi = [150°, 160°, 170°, 180°, 190°, 200°, 210°]$. This means that in the unsteady analysis there is a total of $3\cdot 7 = 21$ angle combinations of θ and ϕ. For the definition of these angles the reader is referred to chapter 6. The final value for the TSSP that is used for evaluation by the optimization algorithm is calculated using the mean p_{rms} from all of the angle combinations.

Since the objective of this work is to optimize the geometry for both aerodynamic and aeroacoustic performance, both of these objectives need to be included in the objective function at some point. There are two methods to do this. The first method is to include both performance indicators in the objective function with a given weight:

$$minimize\ f(x) = k\cdot(1-\frac{\eta}{\eta_0}) + (1-k)\cdot\frac{TSSP_0}{TSSP} \tag{7.3}$$

As you can see, both the efficiency η and the TSSP are both normalized with respect to a baseline value. Since the TSSP values are typically negative, a lower value of the TSSP (meaning a larger negative value) corresponds to lower noise. As such, the TSSP that results from the evaluation of new designs is in the denominator to ensure the value is getting smaller if the noise levels become lower. The value k is a value between 0 and 1, and serves as a weight factor. Depending on whether one wants to focus more on either optimizing for aerodynamic or aeroacoustic performance, this weight factor can be adjusted. The downside of this method is that it is difficult to make a distinction which design changes are made to accommodate either aerodynamic efficiency or aeroacoustic performance. Since this is a key insight to obtain for this work, another approach is chosen.

In the second approach, a single objective is chosen. The first design is optimized for aerodynamic efficiency only. Aeroacoustic performance is not taken into account. Furthermore, instead of looking at the efficiency η, the objective is to find the minimum amount of energy used for a particular case. In this thesis, the combined energy of a climb phase and a cruise phase is considered. The energy is calculated as follows.

$$E_i = \frac{T_i \cdot t_i \cdot V_i}{\eta_i} \tag{7.4}$$

$$E_{total} = E_{climb} + E_{cruise} \tag{7.5}$$

The thrust requirement T, the time spent in the flight phase t, and the flight speed V were set beforehand, their values will be discussed later in section 9.1. The aircraft operates with a different efficiency η during the two considered operations (climb & cruise), since the pitch angle β and advance ratio J are different between the phases. Optimizing solely for aerodynamic efficiency, the objective function becomes:

$$minimize\ f(x) = \frac{E_{total}}{E_{total,0}} \tag{7.6}$$

The outcome of this optimization will return a design with optimum aerodynamic performance for a given flight operation. Next, the optimizer is given the task to the design purely for aeroacoustic performance. However, an inequality constraint is set on the aerodynamic performance that sets how much more inefficient the aeroacoustically optimized design is allowed to be compared to the aerodynamic optimum. These constrains are discussed in more detail in subsection 7.4. The objective function for the aeroacoustic optimization simply becomes:

$$minimize\ f(x) = -\left(\frac{TSSP}{TSSP_0}\right) \tag{7.7}$$

7.3 Design Variables & Bounds

The design variables are the variables the optimization algorithm is allowed to change to achieve its objective. In this work, the design variables are the chord distribution $c(r)$, the twist distribution $\theta(r)$, the collective pitch angle β, and the advance ratio J (see table 7.1 for an overview). This combination of design variables will allow the optimization algorithm a decent amount of freedom in creating different blade geometries. Furthermore, the collective pitch angle β and advance ratio J are allowed to be changed for the different flight phases climb and cruise, which allows the optimization algorithm to make operational adaptations that are optimal for the specific flight phase it operates in.

Table 7.1 Overview of the design variables used in this design optimization study.

Symbol	**Variable Name**	**Unit**
J_{climb}	Climb advance ratio	-
J_{cruise}	Cruise advance ratio	-
β_{climb}	Climb pitch angle	deg
β_{cruise}	Cruise pitch angle	deg
$c(r)$	Chord distribution	m
$\theta(r)$	Twist distribution	deg

As was discussed in section 4.2, the chord and twist distribution parametrisation is done by means of a Bézier curve. The twist and chord distributions each contain 23 values divided over 23 equally spaced radial stations. Using the Bézier curve, each of these distributions can be described with 4 control points, an example of these control points and the resulting curve can be seen in figure 7.1.

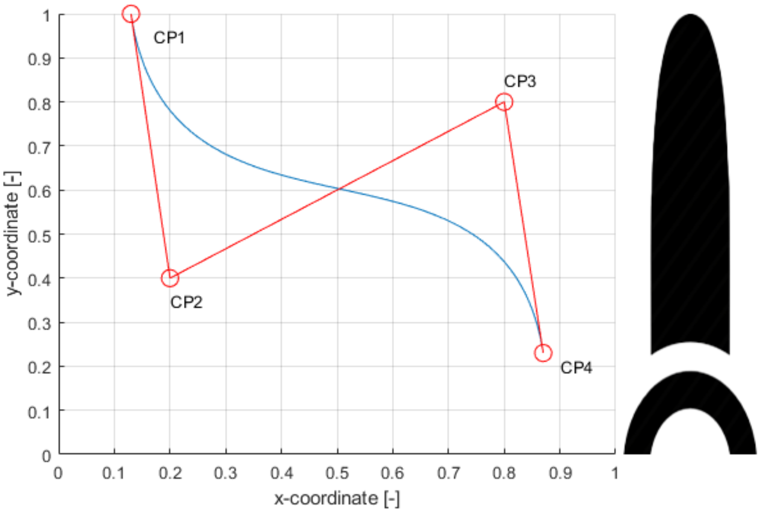

Fig. 7.1 Graphic example of Bézier curve control point locations.

The y-axis in this figure represents the normalized radial position, which goes from 0.23 (the normalized radial location of the first radial station) to 1 (the full radial length). The x-axis represents the normalised twist or chord length. This means that $x = 1$ is equal to the upper bound of the twist or chord and $x = 0$ equal to the lower bound of the twist or chord. The values of these bounds will be discussed shortly. Since it is essential that the distributions are defined at the first radial station and at the tip, the y-values of the first and last control point are fixed at $y_{CP1} = 0.23$ and $y_{CP4} = 1$. This leaves only 6 coordinates as design variables for each of the distributions. Furthermore, it was decided for the twist distribution to fix the twist value of the tip at zero. The collective pitch is added to the twist distribution when calculating the inflow angles at the blade. To make it easier for the optimization algorithm, it is useful to create a point where the angle of the blade is purely influenced by the collective pitch alone. As a result, the x-coordinate of the 4th control point is also fixed for the twist distribution. The full design vector then becomes:

$$x = [x^c_{CP1}, x^c_{CP2}, y^c_{CP2}, x^c_{CP3}, y^c_{CP3}, x^c_{CP4}, x^\theta_{CP1}, x^\theta_{CP2}, y^\theta_{CP2}, x^\theta_{CP3}, y^\theta_{CP3}, \beta_{climb}, \beta_{cruise}, J_{climb}, J_{cruise}]$$

Bounds

The optimization algorithm is allowed to change the design variables in order to find a more optimal design. These changes can only occur within a range delimited by an upper bound and a lower bound set for each of the design variables. The design variables that the optimizer works with are all normalized with respect to these bounds, such that 1 corresponds with the upper bound, and 0 corresponds to the lower bound. In table 7.2 an overview of the upper and lower bounds for each of the design variables is presented. Table 7.3 shows the upper and lower bound of the chord variable when normalized with respect to the diameter ($D = 1.5m$ in this work), which is a more useful reference for feature work that intends to use similar bounds but with a different propeller diameter.

Table 7.2 Overview of the upper and lower bounds of the design variables

Parameter	**Lower bound**	**Upper bound**
θ [deg]	0	60
c [m]	0.05	0.30
β_{climb} [deg]	10	50
β_{cruise} [deg]	10	50
J_{climb} [-]	0.76	1.52
J_{cruise} [-]	1	2

Table 7.3 The upper and lower bound of the chord normalized with respect to the diameter.

Parameter	**Lower bound**	**Upper bound**
c/D [-]	0.033	0.2

The bounds for these values are chosen as such that there is a reasonably large design space, while simultaneously sticking to a range that is realistic and will not lead to problems in the analytical models. The lower bound for the twist angle θ is set to 0 degrees, since it is bounded to be 0 degrees at the tip, as discussed in the previous section, and it was found that the twist is generally the lowest at the tip. For the upper bound, a value of 60 degrees was chosen for the twist angle. This was done based on a significant number of test optimizations with different upper bound values, in which it was found that the twist angle generally did not go above 40 degrees. To allow some design space for unforeseen cases, the upper bound was decided to be 60 degrees. The lower bound of the chord is set to 0.05 m, keeping in mind the propeller diameter used in this work, which was set at 1.5 meter. Given this diameter, going below 0.05 m chord length would lead to unrealistic structures. Similar to the upper bound for the twist angle, the upper bound of the chord length was set based on a number of observations done during testing of the model, and chosen such that there would be sufficient design space for unforeseen cases. The bounds for the advance ratio are determined by the operating conditions of the use case, which operates at a velocity of 38 m/s in climb, and 50 m/s in cruise, has an RPM range of 1000-2000, and uses a propeller with the aforementioned diameter of 1.5 m (these operating conditions are discussed in more detail in section 9.1). Aside from these bounds, the y-coordinate of the control points, which denotes the normalized radial position along the blade, has a lower bound of 0.23. This is to ensure that the resulting Bézier curve does not dip below the radial position of the root of the blade.

7.4 Constraints & Convergence

Constraints are required to limit operational parameters that are not part of the design variables, but which are still impacted by the changes in the design variables. In this thesis work, the propeller design optimizations were done for a specific aircraft in specific predefined flight conditions (see section 9.1 for more information). Given this case, the aircraft had a thrust requirement for the climb and cruise phase that needed to be met. To ensure the optimizer would take this into account, an equality constraint was set on the thrust for both flight phases.

$$T_{cruise} - T_{cruise,required} = 0 \tag{7.8}$$

$$T_{climb} - T_{climb,required} = 0 \tag{7.9}$$

The propeller used also had a power limit for both the climb and cruise phase. To make sure this power limit was not exceeded, two inequality constraint were introduced.

$$P_{cruise} - P_{cruise,limit} \leq 0 \tag{7.10}$$

$$P_{climb} - P_{climb,limit} \leq 0 \tag{7.11}$$

Furthermore, it was found during testing of the models that there was a possibility to end up with unrealistic values for the efficiency η (namely values below 0 or above 1). This could occur when a design vector formed a very unusual combination of geometry and operational conditions, which presented the model with a situation that led to convergence issues. Therefore, inequality constraints were added such that the efficiency values for both climb and cruise could not exceed 1 or go below 0.

$$\eta - 1 \leq 0 \tag{7.12}$$

$$-\eta \leq 0 \tag{7.13}$$

Finally, as discussed in section 7.2, an inequality constraint is put on the total energy use when optimizing for purely aeroacoustic performance, such that the new design is only allowed to be a certain percentage less aerodynamically efficient than the aerodynamic optimum.

$$E_{calculated} - (1+p) \cdot E_{optimum} \leq 0 \tag{7.14}$$

The factor p determines how many percentage points more the total energy expenditure is allowed to be compared to the total energy expenditure of the aerodynamic optimum design. Multiple optimizations are done in which only the factor p is changed. The values for p used in this work are 0.01, 0.02, and 0.05. This allows one to observe the changes that are made specifically to benefit aeroacoustic performance and exactly know the energy penalty that would come along with that.

It should be noted that the constraints were implemented exactly in the manner they are presented above, which means that the constraints are not normalized. Normalized constraints are common practice in the setup of optimization routines, since they can be beneficial when scaling the problem. However, in this work the current implementation of the constraints did not lead to any complications, and made a direct assessment of the absolute constraint violation easier, which in the overwhelming majority of cases was a constraint violation in the thrust requirement constraint.

A result was deemed acceptable if the absolute constraint violation did not exceed 0.01. Typically, the limiting constraint was found to be the thrust constraint. The optimizer would stop if the changes in design variables would be smaller than a certain threshold. If, at that point, the maximum constraint violation was less than 0.01, the result was saved.

7.5 Optimization Algorithm

For this work it was decided to use MATLAB's FMINCON to control the optimization process, an off-the-shelf gradient-based method[45]. The FMINCON set-up is able to optimize using multiple design variables and non-linear constraints. Furthermore, it is rather easy to implement parallel computing with this set-up, which significantly sped up the process. The algorithm used with FMINCON was chosen to be the sequential quadratic programming (SQP) algorithm. This algorithm is chosen for its relative speed of optimization and its robustness, being able to recover from unfeasible results such as ∞. For more in-depth info on the SQP algorithm, the reader is referred to the work of Nocedal et al.[46]. As was discussed earlier in chapter 4, distinct variables were purposely avoided, such that a gradient-based optimization method could be used, since gradient-based optimization methods are known to be faster than alternative methods. It should be noted that this method will find a local optimum, and is not guaranteed to find a global optimum. Given the time and resources available for this project, this was deemed acceptable. To maximize the chance of finding a global optimum, typically 3 to 5 optimization runs were performed using different randomized initial points, and the results were compared.

7.6 Final Definition

In the final definition of the optimization problem, all the previously discussed elements are combined. This definition simply serves as a useful and clear overview of the optimization problem that is being solved. As discussed, the optimization is divided into two stages. Stage 1 focuses on aerodynamic optimization only. The problem is defined as follows:

$$\textit{minimize: } f(x) = \frac{E_{total}}{E_{total,0}}$$

$$x = [x^c_{CP1}, x^c_{CP2}, y^c_{CP2}, x^c_{CP3}, y^c_{CP3}, x^c_{CP4}, x^\theta_{CP1}, x^\theta_{CP2}, y^\theta_{CP2}, x^\theta_{CP3}, y^\theta_{CP3}, \beta_{climb}, \beta_{cruise}, J_{climb}, J_{cruise}]$$

$$\begin{aligned} \textit{subject to: } T_{cruise} - T_{cruise,required} &= 0 \\ T_{climb} - T_{climb,required} &= 0 \\ \eta - 1 &\leq 0 \\ -\eta &\leq 0 \\ P_{cruise} - P_{cruise,limit} &\leq 0 \\ P_{climb} - P_{climb,limit} &\leq 0 \end{aligned}$$

Once the aerodynamic optimum is known for a given blade count, stage 2 starts, in which aeroacoustic performance becomes the objective with a constraint on the maximum energy expense.

$$\textit{minimize: } f(x) = -\left(\frac{TSSP}{TSSP_0}\right)$$

$$x = [x^c_{CP1}, x^c_{CP2}, y^c_{CP2}, x^c_{CP3}, y^c_{CP3}, x^c_{CP4}, x^\theta_{CP1}, x^\theta_{CP2}, y^\theta_{CP2}, x^\theta_{CP3}, y^\theta_{CP3}, \beta_{climb}, \beta_{cruise}, J_{climb}, J_{cruise}]$$

$$\begin{aligned} \textit{subject to: } T_{cruise} - T_{cruise,required} &= 0 \\ T_{climb} - T_{climb,required} &= 0 \\ \eta - 1 &\leq 0 \\ -\eta &\leq 0 \\ P_{cruise} - P_{cruise,limit} &\leq 0 \\ P_{climb} - P_{climb,limit} &\leq 0 \\ E_{calculated} - (1+p) \cdot E_{optimum} &\leq 0 \end{aligned}$$

Part III

Model Validation & Results

Chapter 8

Verification & Validation of Tools

Verification and validation are essential steps to ensure that the models used will generate results that have a certain degree of accuracy and are indicative of what would be observed in experiment or real-life operation. This chapter will present the verification and validation of the modelling tools used in this work, starting with BEM model in section 8.1. Next, the aerodynamic model for non-uniform flow will be covered in section 8.2, and the chapter will finish with the discussion of the aeroacoustic model in section 8.3.

8.1 Blade Element Model

The aerodynamic performance model used in this work is a Blade Element Model implementation based on the work of Liu et al.[32] Several other authors have used this model in their respective publications, and published verification and validation data to support the use of this model. These publications include the works of Geng et al.[16], Hu[13], Dufour[17], and de Haan[28]. In figures 8.1-8.3 the validation data from the work of Geng et al.[16] can be seen. In these graphs, the data generated by the BEM model is compared to experimental data generated by wind tunnel tests conducted in Beihang's D5 acoustic windtunnel. The publication can be referred to for the full experimental setup[16]. The data was generated using a constant RPM of 2300, and a freestream velocity range of 9 - 35 m/s, with a propeller diameter of 0.6 m.

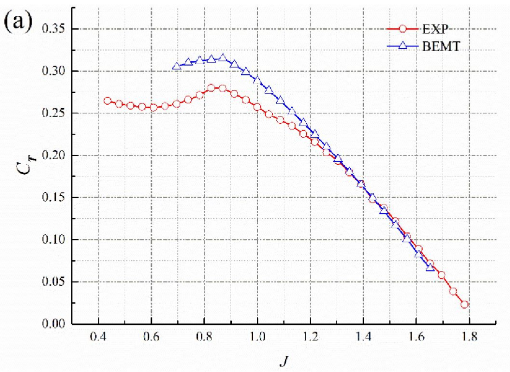

Fig. 8.1 Comparison of the thrust coefficient between experiment and the BEM-model. [16]

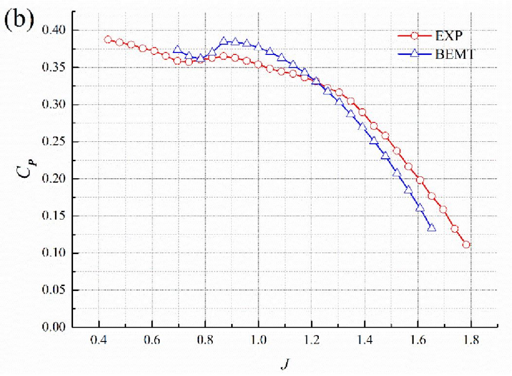

Fig. 8.2 Comparison of the power coefficient between experiment and the BEM-model. [16]

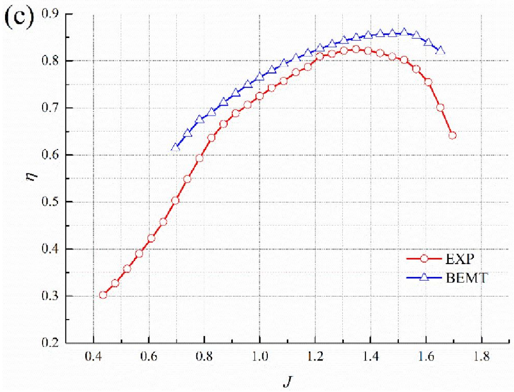

Fig. 8.3 Comparison of the efficiency between experiment and the BEM-model. [16]

As can be seen, there is reasonable agreement between experiment and the BEM model predictions (denoted as BEMT in the figure legend), in particular when it comes to the slope of the curves. A larger discrepancy occurs at lower advance ratios. This can be explained by the fact that radial forces become more dominant at lower advance ratios, which are assumed to be absent in the BEM model, and the fact that the onset of three-dimensional stall is not captured by the model. As figure 8.3 shows, the efficiency is over-predicted, and the point of maximum efficiency occurs at a higher advance ratio compared to the experiment. This should be taken into consideration when examining the results of the optimization. Overall, there is acceptable agreement between experiment and results in the range of advance ratios $J \in [0.9, 1.3]$, corresponding to a thrust setting of $C_T \in [0.30, 0.20]$. It should be noted that the thrust setting is the relevant metric here, since the range of advance ratios in which good agreement is found will different based on pitch setting.

Figure 8.4 from the work of Dufour compares the model by Hu (a BEM implementation based on the work of Liu[32]), with a BEM model implementation from the work of Gur and Rosen, and experimental data from an experiment in the wind tunnel at the TUD Open-Jet Facility in 2017[18].

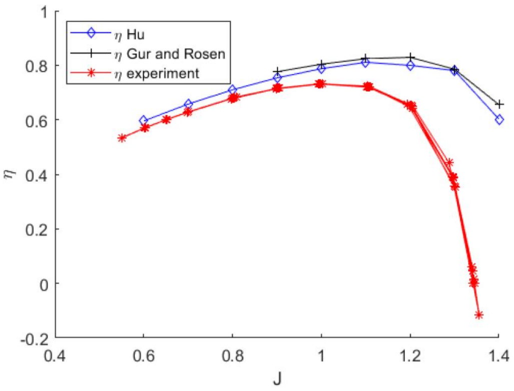

Fig. 8.4 Comparison of the efficiency between experiment and BEM-models. [17]

This figure shows reasonable agreement between the BEM model and experimental data in the range of advance ratios $J \in [0.6, 1]$. Similar to the results from Geng et al.[16], it can be seen that at higher advance ratios the model predictions and experimental data start to diverge, and that the advance ratio for maximum efficiency is over-predicted. An explanation for this behavior is that at higher advance ratios, the blade operates at lower Reynolds numbers, which typically increases viscous effects which aside from those that were included in the 2D airfoil analysis are not captured by the BEM model. For the large part however, the predictions by the BEM model are in reasonable agreement with the experimental results. The BEM implementation of Hu also shows very close agreement to the BEM implementation of Gur and Rosen, further increasing confidence in the model.

Figure 8.5 shows a comparison between the prediction of the thrust coefficient by the BEM model and experimental data[18] of the TUD-XPROP propeller at $V_\infty = 30\ m/s$ and $D_{prop} = 0.4046\ m$. The paper cited can be consulted for full details of the experiment. As can be seen, there is a reasonable agreement between the slopes from $J = 0.5$ until $J = 0.8$. After this point however, the slopes start to deviate and become quite different with respect to each other. This deviation could be because the Reynolds numbers become low with increasing advance ratio which, as mentioned earlier, typically increases viscous effects which aside from those that were included in the 2D airfoil analysis are not captured by the BEM model. As such it can be observed that in this comparison the model data does not match the experimental data very well. A difference in the gradient of $C_T - J$ will have an impact on the prediction of the installed performance of the propeller. However, the propeller designs that were optimized in this study were significantly larger in scale ($D_{prop} = 1.5\ m$ instead of $D_{prop} = 0.4046\ m$), and operated at higher freestream velocities ($V_\infty = 38\ m/s$ (climb) and $V_\infty = 50\ m/s$ (cruise) instead of $V_\infty = 30\ m/s$), compared to the propeller used for the experiment and modelling data presented in figure 8.5. As a result, the designs that were optimized in this study operate at a much higher Reynolds number compared to the Reynolds numbers that were present in this comparison, which is likely to decrease the deviation between model data and experiment. Furthermore, a more extensive comparison between the $C_T - J$ gradient from the BEM-model and a CFD RANS model is presented later in section 8.2, which also showed minimal differences. Combining these observations, it is very likely that the deviation between experiment and model data as presented here did not have a significant effect on the results.

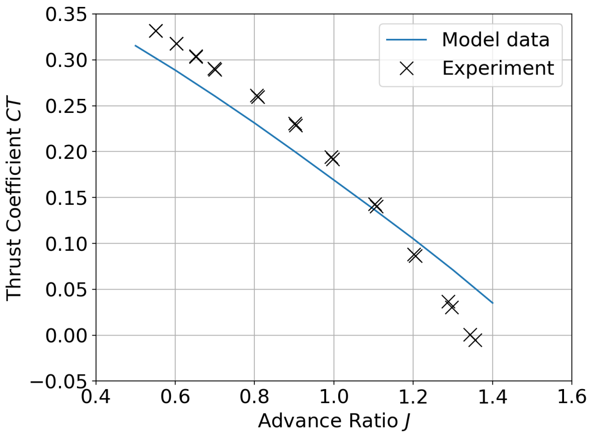

Fig. 8.5 Comparison of the thrust coefficient between experiment and implemented BEM-model. [18]

Overall, despite slightly over-predicting efficiency values, the model seems to be able to accurately predict the slope and trend of the performance indicators. When reaching higher advance ratios however, blade loading tends to be lower, and the Reynolds number becomes low enough such that viscous effects are starting to play a significant role. At this point, the BEM predictions start to deviate substantially, because viscous effects, aside from those that were included in the 2D airfoil analysis, are neglected by the model. Therefore, when regarding the BEM predictions, it should be kept in mind that the efficiency is likely over-predicted, and results occurring at low Reynolds numbers and low blade loading should be regarded with more caution. Predicting the trend correctly is the main aim of this work, as the choice was made early on to sacrifice a degree of accuracy for faster models. This can be achieved with this BEM model. Furthermore, since the propeller in this work has a substantially larger diameter than the TUD-XPROP used in the experiments ($D_{prop} = 1.5m$), and thus blade chord lengths are larger, the blades are operating at higher Reynolds number than in the experiment, thereby avoiding the problematic region seen in the validation data occurring at low loading and low Reynolds numbers.

8.2 Aerodynamic Model for Non-Uniform Flow

To model the non-uniform flow effects on the aerodynamic performance characteristics of the propeller, a model proposed by van Arnhem[5] was used. This model and the validation procedure are extensively covered in the paper. In the paper, two methods of validations are used, namely comparison to a CFD analysis, and to an experiment. While the paper covers four cases, this section will only cover the case for a propeller under an angle of attack of 5 degrees, since that is the only case that was analyzed in this work. Two versions of the method are developed, a quasi-steady method, and an unsteady method that employs the Sears equation for an unsteady correction. The model used in this work only uses the unsteady method. In figure 8.6, a comparison can be seen between the two methods and the full-blade CFD analysis data. It should be noted that the x-axis of the graphs in this figure represent a full rotation of the propeller from 0° to 360°. The parameter η_B on the y-axis of the graph on the right represents the difference in blade efficiency throughout the blade revolution with respect to the efficiency value computed by the full-blade CFD simulations[5].

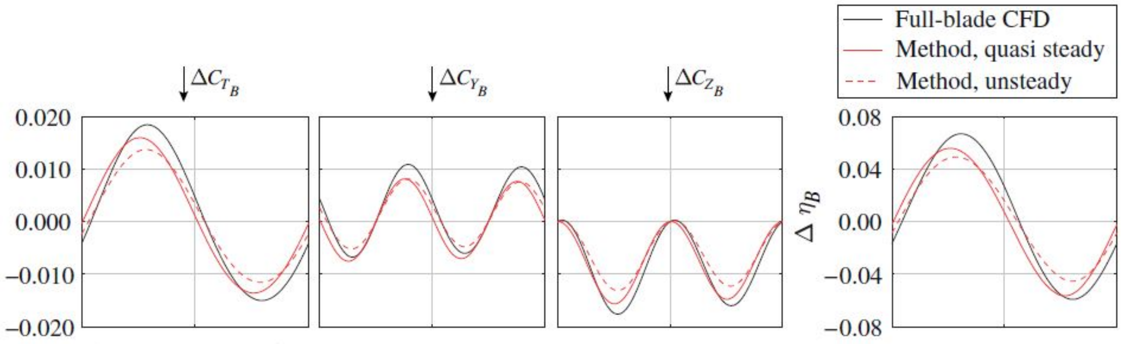

Fig. 8.6 Comparison of the change of the integral blade forces between method predictions and full-blade CFD simulations ($\alpha = 5°, J = 1.8$). [5]

As can be seen in the figure, a significant phase difference exists between the quasi-steady method and the CFD data. For the unsteady method however, this phase lag is reduced by a large margin. Due to fact that the predicted load distribution has a phase advance, the relative integral in-plane forces are inaccurate. This can be seen quite clearly in figure 8.7, in particular by the difference in ΔC_Y. While the unsteady prediction comes much closer to the CFD data, there is still a significant error. Since there is a strong variation of loading over the propeller disk, a non-uniform slipstream would be present, which would lead to an increase in the force magnitude experienced by the propeller blades. This effect is captured by the CFD simulation, but the slipstream is not computed in the proposed method, and as a result the loads are underpredicted. The unsteady correction further reduces the magnitude of the predicted loads and increases the error in magnitude. This difference can clearly be seen in the amplitude difference in figure 8.6. Altogether, total underprediction errors of 12% and 24% were found for the root-mean square of the blade thrust for the quasi-steady and unsteady methods respectively. Nevertheless, the integral thrust and torque values that were calculated were nearly identical between the predictions and CFD. This is likely due to the fact that the loading curves behave very much like a sinusoid, and the differences in magnitude extend both in the positive and in the negative, therefore partially equalling each other out.

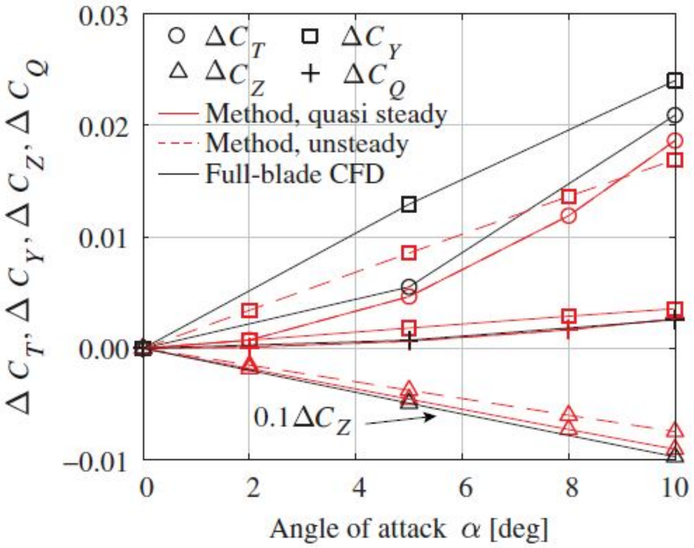

Fig. 8.7 Comparison of the change in loading coefficients (integrated values) between the model of van Arnhem and a full-blade CFD for validation purposes. [5]

One of the other limitations of the method is that it evaluates the inflow along a line that describes the propeller blade, therefore effectively assuming that the chord length is zero. In the future, the representation of the inflow could therefore be improved if the inflow at location (r, ϕ) would be determined using a weighted velocity along the projected chord in the plane of rotation[5]. This could further improve the accuracy of the model. Overall however, it can be concluded that the integral forces on the individual blades over a full revolution and the integral propeller forces compare reasonably well to the validation data in magnitude and when comparing trends. Therefore, this model is deemed accurate enough to be used in this work.

To use the model, two datasets are required. A dataset describing the isolated propeller performance for a range of advance ratios, both through a variation of the rotational velocity with constant freestream velocity and for constant rotational velocity with a varying freestream velocity, and a dataset describing the non-uniform inflow. The only difference between the implementation used in this study and the implementation proposed in the paper is the method by which the dataset that describes the isolated propeller performance is generated. In the paper, CFD methods are used to generate this data, while in this work the BEM-method is used to generate this data. In the paper, a number of graphs are shown that visualize the isolated propeller performance dataset used. To verify whether the BEM-model can generate this dataset accurately, the BEM-model was used to recreate this dataset with the exact inputs used in the paper. The reader is referred to the paper to find the details of the propeller and simulation setups that were used. Figures 8.8, 8.9, and 8.10 show a comparison between the graphs from the paper by van Arnhem[5], and the graphs generated by the model used in this thesis work.

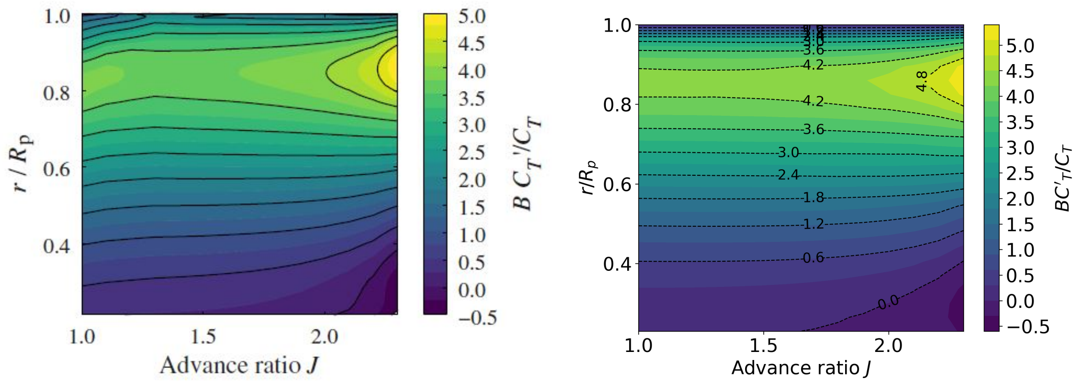

Fig. 8.8 Comparison of the normalized radial thrust coefficient from the paper by van Arnhem[5] (left) and the data generated by the model used for this thesis (right).

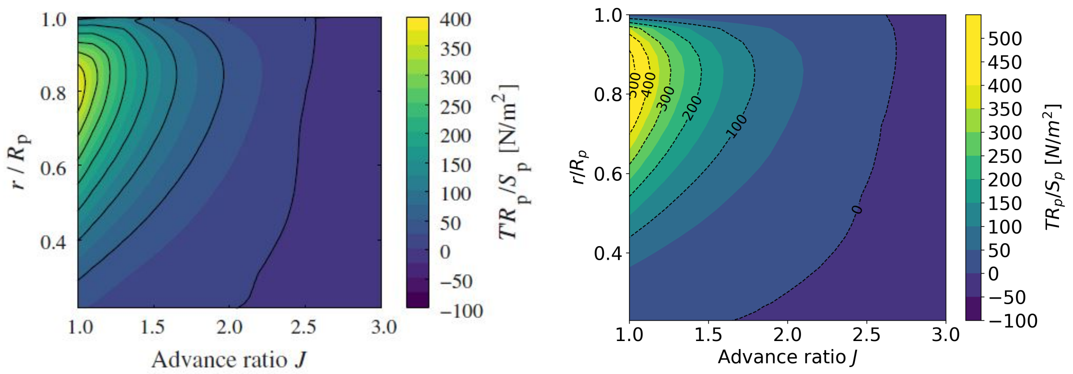

Fig. 8.9 Comparison of the sectional disk loading with constant freestream velocity ($V_\infty = 40$ m/s) from the paper by van Arnhem[5] (left) and the data generated by the model used for this thesis (right).

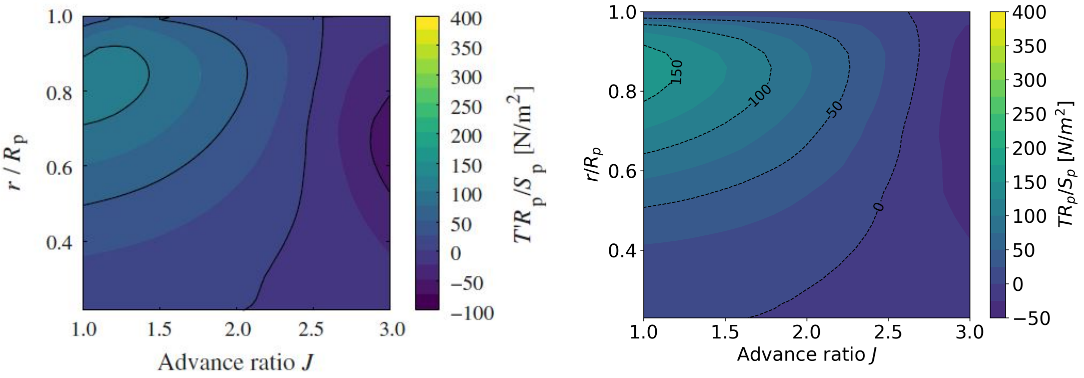

Fig. 8.10 Comparison of the sectional disk loading with constant rotational velocity ($n = 109.4$ Hz) from the paper by van Arnhem[5] (left) and the data generated by the model used for this thesis (right).

As can be seen, the figures look very similar, but a few differences require mentioning. Looking at the right graph of figure 8.9, it can be seen that there is a notable difference compared to the left graph at $r/R_p = 0.8$ and $J \in [1.0, 1.5]$. The color scheme has been adjusted such that the color schemes of the left graph and right graph are identical, despite the right graph having a larger range of values (i.e. the values above 400 in the right graph are all the same yellow color). This shows that the force concentration in the right graph at $r/R = 0.8$ for low advance ratios is slightly larger, and reaches higher forces. In the left graph of figure 8.10 this is seen as well, and in this graph forces at high advance ratios do not reach as low of values as in the graph from the work of van Arnhem either. This difference is caused by the inaccuracies of the BEM model. As shown earlier in the section about BEM-model validation, the BEM-model is accurate in predicting trends, but tends to overestimate the actual values. Moreover, at low thrust coefficients, which typically correspond to the high end of the range of advance ratios used, it showed that the BEM-model can start to deviate significantly from experiment. Given these inaccuracies of the BEM-model, the likeness between the graphs and the values is still remarkably good. In addition, the most relevant gradient to determine the installed performance is the $C_T - J$ gradient, represented in a different form in figure 8.8. In this figure the best agreement is seen between the left graph, taken from the paper by van Arnhem, and the right graph, generated by the BEM-model used in this thesis. Little to no meaningful difference can be spotted in this comparison. Combining these observations, it was deemed that the BEM-model input is sufficiently accurate.

8.3 Helicoidal Surface Theory

Finally, the aeroacoustic model needs to be subjected to verification and validation. As presented earlier in chapter 6.2, this work uses a method based on calculating the noise in the frequency domain known as Hanson's Helicoidal Surface Theory (HST)[15]. Two versions of this theory are implemented in this work, namely one for a propeller in uniform flow, and one for a propeller subjected to a non-uniform flow. Both implementations will be discussed.

To verify the steady implementation of the model, a number of methods were used. To begin, a comparison was made between the outcome of the model created for this work and the model used by de Haan[28], who implemented the same model and also made use of the TUD-XPROP propeller design. It was found that both models led to the exact same results in magnitude and in the shape of the directivity plot.

Next, a qualitative assessment was made in which the directivity plots for volume, thrust, and torque noise generated by the model were compared to the general shapes expected by theory[19].

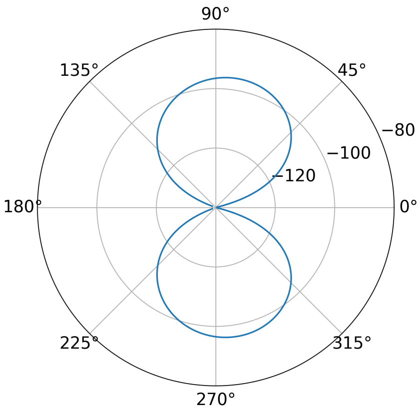

Fig. 8.11 Volume noise directivity plot generated by the HST model.

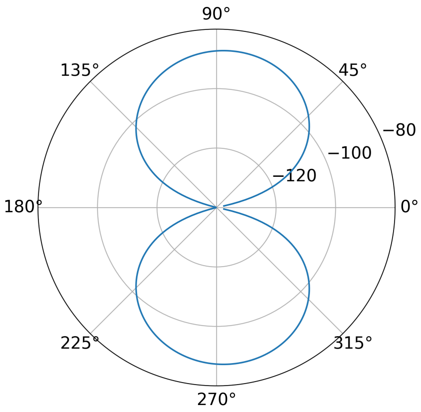

Fig. 8.12 Torque noise directivity plot generated by the HST model.

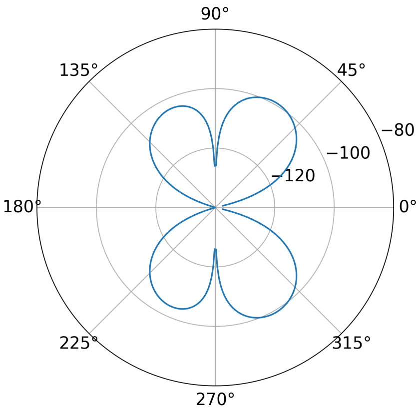

Fig. 8.13 Thrust noise directivity plot generated by the HST model.

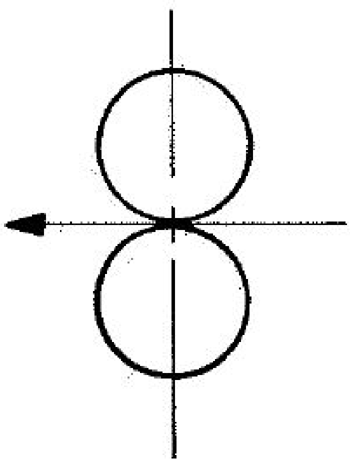

Fig. 8.14 General shape volume noise directivity plot. [19]

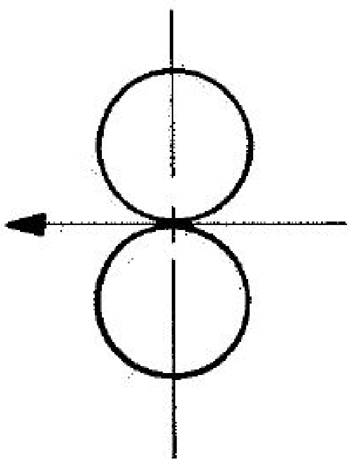

Fig. 8.15 General shape torque noise directivity plot. [19]

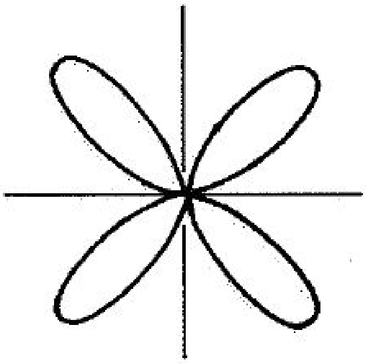

Fig. 8.16 General shape thrust noise directivity plot. [19]

Comparing these figures, it can be seen that they qualitatively match. All three graphs display the same number of lobes compared to what is expected based on theory, and form roughly the same shape. The difference in shape, in particular visible when comparing the thrust noise, can be explained by the fact that a real and specific cases analysis is compared to a theoretical ideal. Another cause of the difference could be that convection effects are accounted for in the simulations, but not in the theory, which only describes the noise generation at the source. Judging the comparison, it can be concluded that there is a qualitative match, and that the model predictions take the shape that would be expected based on theory[19].

Steady HST Harmonics Verification

The magnitude of the calculated maximum noise is partly dependent on the number of sound harmonics m. Typically, the first couple of harmonics are dominant, while the higher harmonics have little to no contribution to the overall noise emissions. However, it is important to determine the number of harmonics required to get an accurate result, while keeping it low enough to limit computational effort. A sensitivity study was carried out to measure the effect of the number of harmonics on the maximum TSSP predicted by the model. For this study, the 6-bladed TUD-XPROP was used with diameter of 1.5 m, a pitch angle of 30°, operating at an advance ratio of $J = 1$. The results can be seen in figure 8.17, and table 8.1. As the figure and table data clearly demonstrate, the error is already practically negligible when including two harmonics, and at that point also becomes smaller than the resolution of the model, and thus irrelevant. This study used seven harmonics to be consistent with the amount of harmonics used for the unsteady noise analysis. Based on this sensitivity study, it can be established with certainty that a sufficient number of harmonics was used such that there was no loss in accuracy.

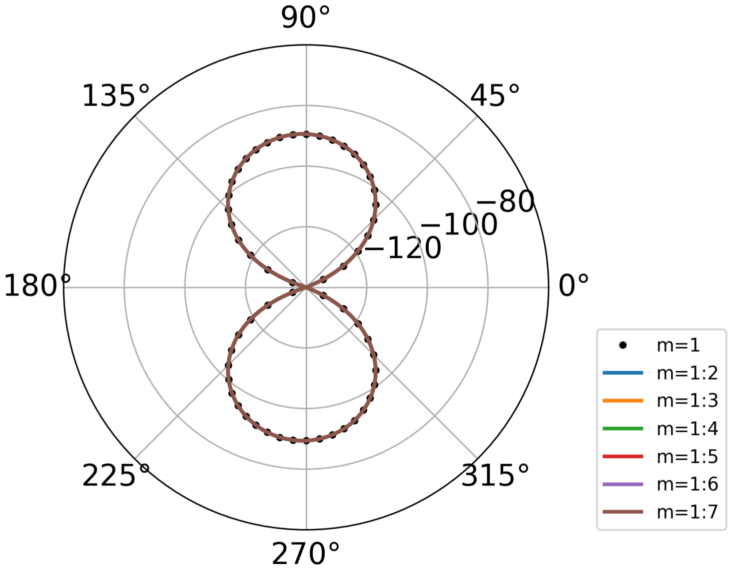

Fig. 8.17 TSSP directivity plot with respect to observer angle θ for an increasing amount of sound harmonics m.

Table 8.1 Comparison of maximum TSSP and the difference in maximum TSSP with respect to the previous row for increasing harmonics m.

	Maximum TSSP	$\Delta\, TSSP_{max}$
m = 1	-89.38613	0
m = 1:2	-89.37715	0.008987
m = 1:3	-89.37712	2.45E-05
m = 1:4	-89.37712	8.23E-08
m = 1:5	-89.37712	3.21E-10
m = 1:6	-89.37712	1.38E-12
m = 1:7	-89.37712	0

Steady HST Validation

A paper published by Kotwicz-Herniczek et al.[20] made an attempt at validating several noise models, among which Hanson's model, by comparing predictions to a large number of experiments. In this paper, the steady HST model was coupled with a BEM model, making it particularly relevant as a reference for this work. The predictions by Hanson's HST model were compared to a total of 14 experiments which covered measurements for a wide range of propeller designs, flight conditions, and microphone locations. The paper covers in detail the comparison between the model predictions and each of the experiments, and the reader is encouraged to consult this work for more in-depth information. In figure 8.18, an overview is shown of the prediction error between the model predictions and the test cases at the location of maximum tonal noise.

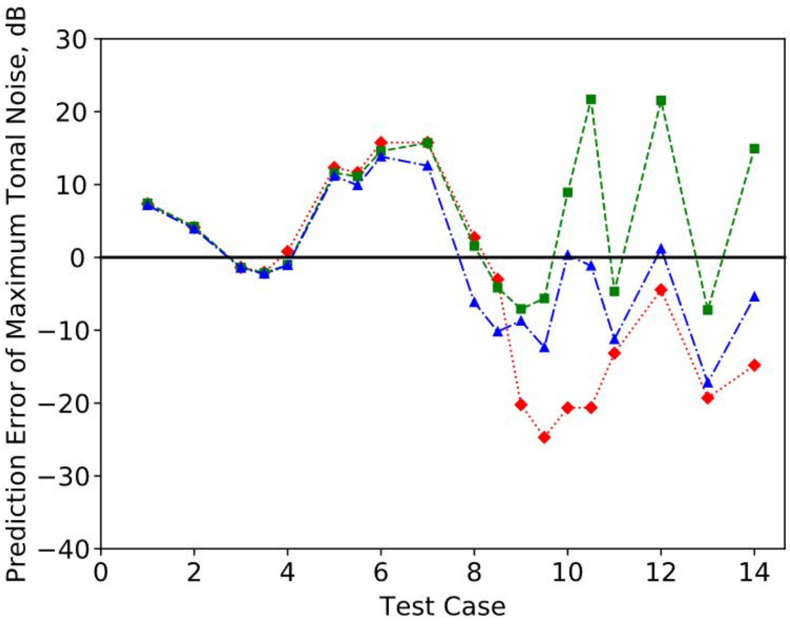

Fig. 8.18 Overview of the prediction errors between model predictions and experiment at the location of maximum tonal noise. Models used: Gutin and Deming (Red), Barry and Magliozzi (Green), Hanson's HST model (Blue). [20]

The figure shows that the model both under- and over-predicts the maximum noise level depending on the experiment. Over all experiments, Hanson's model performed with an average absolute error of 5.9 dB. Although this is a significant error, the model showed a reasonable capability of predicting the correct trends in aeroaocustic performance, and was the most consistent and accurate model out of the three models evaluated in the paper. From this data, it can be concluded that the model is only useful in preliminary design studies to form an initial estimate of the trends and performance, but the exact values can not be relied upon with a sufficient degree of confidence. This is line with the conclusion drawn by Kotwicz-Herniczek et al. who state that *"The implemented acoustic methods correctly predicted acoustic trends for low-order harmonics and, as such, are useful for initial design and optimization studies, despite substantial (5–10 dB) acoustic error."*[20]. Since this study is an initial design and optimization study, the model is deemed suitable for this work.

8.3.1 Unsteady HST

As discussed previously in chapter 6, the unsteady version of the HST model is a modification of the original model. In this modification, an extra factor k is introduced, which represents the load harmonic. When this k factor is set to zero, the result of the unsteady HST model should be the same as that of the steady HST model, given the same input. This check was performed and verified. Next, a study was performed as to how many factors k are necessary to accurately represent the loading curves C_l and C_d. The C_l and C_d that are being reconstructed are the curves that were determined using the aerodynamic model for non-uniform flow, as a result of an inflow under an angle of attack of 5 degrees. Figures 8.19-8.22 show presentable results from this study.

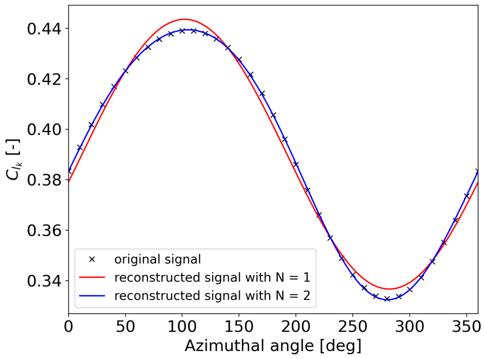

Fig. 8.19 Comparison of the Fourier representation of the time-dependent loading C_l for 1 and 2 coefficients.

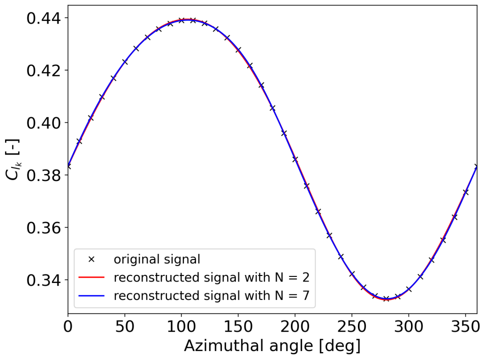

Fig. 8.20 Comparison of the Fourier representation of the time-dependent loading C_l for 2 and 7 coefficients.

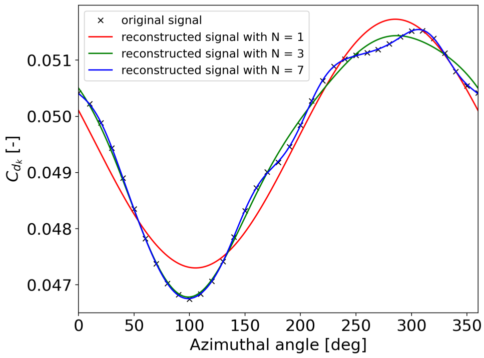

Fig. 8.21 Comparison of the Fourier representation of the time-dependent loading C_d for 1, 3, and 7 coefficients.

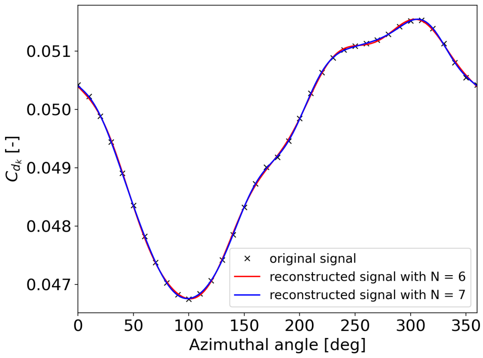

Fig. 8.22 Comparison of the Fourier representation of the time-dependent loading C_d for 6 and 7 coefficients.

As can be seen in the figure, just one coefficient k is not sufficient for an accurate representation of the original signal, especially in the case of C_{dk}. For C_{lk}, just two coefficients seems to be enough to already get a good representation, as the difference between 7 and 2 coefficients is hardly observable. For C_{dk}, it can be seen that more coefficients are necessary for an accurate representation. In this study it was chosen to use a total of 7 coefficients k, which was found to be sufficient to represent the C_{dk} and C_{lk} curves with an acceptable accuracy for a number of test cases (different radial stations were tested for two separate propeller designs). Given these figures, which represent a typical test case, it can be verified that a total of 7 coefficients is sufficient.

Similar to what has been done for the steady HST method, a sensitivity study was carried out with respect to the coefficient m (sound harmonic). Except this time, the noise varies with two observer angles instead of one. In figure 8.23, the observer angle ϕ is set to $\phi = 180°$, which corresponds to the location right underneath the propeller, while the observer angle θ is varied over the entire 360 degrees with steps of 1 degree. Similarly, in figure 8.24, the angle θ is fixed to $\theta = 90°$, which corresponds to the propeller plane, while the angle ϕ is varied over the entire 360 degrees with steps of 1 degree. The maximum value for TSSP and the difference with respect to the previous row are accumulated in table 8.2. The data clearly shows that even two coefficients would likely be enough for a sufficiently accurate result, as the difference becomes small after 2 coefficients.

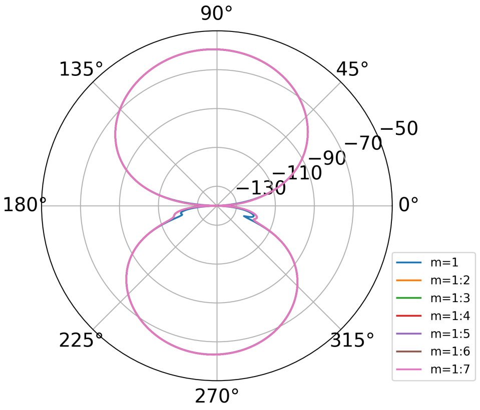

Fig. 8.23 TSSP directivity plot with respect to observer angle θ for an increasing amount of sound harmonics m.

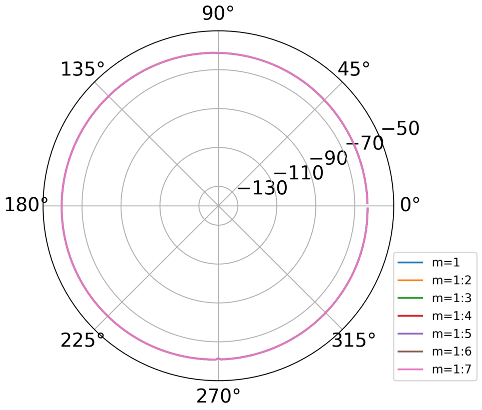

Fig. 8.24 TSSP directivity plot with respect to observer angle ϕ for an increasing amount of sound harmonics m.

Table 8.2 Comparison of maximum TSSP and the difference in maximum TSSP with respect to the previous row for increasing harmonics m.

	Varying θ / Fixed ϕ		**Fixed θ / Varying ϕ**	
	Maximum TSSP	Δ TSSP	Maximum TSSP	Δ TSSP
m = 1	-59.4884	0	-59.4874	0
m = 1:2	-59.4319	0.056475	-59.4315	0.05595
m = 1:3	-59.4311	0.000741	-59.4307	0.000764
m = 1:4	-59.4311	1.10E-05	-59.4307	1.13E-05
m = 1:5	-59.4311	1.59E-07	-59.4307	1.45E-07
m = 1:6	-59.4311	2.66E-09	-59.4307	2.81E-09
m = 1:7	-59.4311	3.77E-11	-59.4307	4.53E-11

Aside from the aforementioned efforts in verification, some basic sanity checks were performed to ensure the model was working correctly. Among these were checking whether the unsteady noise model would actually predict louder maximum noise compared to the steady model, checking whether the imaginary part of the Fourier coefficients would cancel out in the final step when the signal was converted to the time domain, and critically reflecting on the directivity plots using basic knowledge of aeroacoustic physics. The result of these checks were all positive. Unfortunately, the author is unaware of other the work of other authors who had successfully incorporated this model, so no direct comparison of results could be made. However, given that all the other checks had positive results, a satisfactory confidence in the model implementation has been established.

By the author's knowledge, there are no detailed and comprehensive studies similar to that of Kotwicz-Herniczek et al.[20] that validate the adaptation of Hanson's theory used in this work by means of comparison to CFD or experiment. Moreover, a validation effort of that kind could not be part of this work due to time limitations. Therefore, the results generated by this model should be considered with the knowledge that the exact value of the noise prediction is likely inaccurate, and that the results are likely only useful in the context of preliminary design studies and for predicting trends, just as the results from the steady noise prediction model. As the unsteady modification of the HST model introduces additional layers of complexity, it is unlikely that the model would be more accurate than the steady HST model, which showed significant prediction errors in terms of the noise magnitude, but was deemed to be accurate enough to do preliminary predictions for design purposes. The results should be used with caution until more is known about the validity and accuracy of the model for the use case presented in this work.

Chapter 9

Optimization Results

This chapter will present the exact details of the design optimization studies performed for this work, and the results of these studies. First, in section 9.1, the specific use-case and operational conditions that were used during the study will be discussed, as well as other necessary information for the interpretation of the results. Next, in section 9.2, the results will be presented and extensively analyzed.

9.1 Evaluation Setup

To ensure the design optimization has a link to an actual use-case, several operational parameters of this study were based on data from Project Dragonfly[47]. This project aims to build a small 2-seater aircraft, whose design is based on the Viking Dragonfly MKII model, with an electrically powered propeller as a powerplant. The operational data used for the propeller design optimization studies carried out for this work are presented in table 9.1.

Table 9.1 Operational parameters used in the design optimization study.

Parameter	**Climb**	**Cruise**
Measurement altitude [m]	100	1000
Velocity [m/s]	38	50
Thrust requirement [N]	830	480
Time mission segment [min]	6	30
Maximum available engine power [kW]	45	30
Propeller diameter [m]	1.5	1.5
RPM range	1000-2000	1000-2000

The operating velocities, thrust settings, engine power requirement, propeller diameter, and RPM range were based on data from the Dragonfly project. The measurement altitudes of 100 meter was determined by the author to allow comparison with results from a different author not available to the public. The measurement altitude of 1000 meter is simply the cruise altitude of the Project Dragonfly aircraft. Furthermore, a set number of minutes was assigned to each mission segment according to the mission profile that was part of Project Dragonfly. This time is necessary to compute the total energy used, which forms one of the optimization objectives. By setting the cruise time to be five times the climb time, the cruise segment will have a larger impact on the efficiency of the aircraft (total energy spent), such that it represents real aircraft operation. The ambient conditions of the atmosphere are based on the International Standard Atmosphere model, evaluated at the altitude of the two mission segments (see table 9.2).

Table 9.2 Atmospheric parameters used in the design optimization study.

Property	**Climb**	**Cruise**
T_{amb} $[K]$	287.5	281.651
p_{amb} $[Pa]$	100129.456	89876.2776
ρ_{amb} $[kg/m^3]$	1.21328	1.11166
μ $[N \cdot s/m^2]$	1.8592040e-05	1.8005977e-05
Speed of sound $[m/s]$	339.91	336.43

As discussed earlier in this work, a gradient-based optimization method was used in this design optimization study. A downside of using this type of optimization method is that it is possible to converge to a local optimum. To maximize the chance of finding a global optimum instead of a local optimum, typically 3 to 5 optimization runs were performed for each case with different randomized initial vectors, and the results were compared. The best results in terms of performance improvement and constraint violation are presented in this work.

The non-uniform inflow used in this work is an inflow under an angle of attack of 5° with respect to the propeller axis. The inflow data for this non-uniform inflow was determined in the work by van Arnhem[5], operating at a 40 m/s freestream velocity. The data used in the paper by van Arnhem[5] was provided to the author, and could be normalized and projected onto the propeller used in this work at the freestream speed defined for this work.

9.2 Optimization Results

In this section, the results of the design optimization study will be presented and discussed. To keep this discussion organized, the results are divided among several subsections. First, the results of the design optimization for a uniform inflow will be discussed. Within this subsection, a distinction is made between the optimization for aerodynamic performance and the optimization for aeroacoustic performance. Naturally, a comparison between the two is also discussed. Next, the design optimization results for a nonuniform inflow are presented, again subdivided in the results for aerodynamic and aeroacoustic performance optimization. Comparisons will be made with the results from the uniform inflow design optimization in this subsection as well. It should be noted that for all results the disk loading remained unchanged for each of the two mission segments, since both the diameter and the required thrust remained constant.

Design optimization studies were conducted for a three-, four-, five-, and six-bladed propeller. For each of these blade counts, a design optimization was conducted for aerodynamic performance. Since the aerodynamic optimization required a small computational effort, it was possible to do the analysis for four separate blade counts within a relatively short time-span. The aeroacoustic design optimization required a significantly higher computational effort, which forced the author to limit the blade counts for which a propeller design could be optimized. Based on the results from the aerodynamic optimization, it was decided that the three- and four-bladed propeller cases were the most interesting cases to use for the aeroacoustic optimization, since these cases were not limited in their aerodynamic performance optimization by reaching a bound in the design variables (the five- and six-blade propeller cases were). Therefore, for the aeroacoustic design optimization, only a three- and four-bladed propeller were used, and a design optimization was performed with three different energy penalty levels. These energy penalty levels were a 1%, 2% and 5% allowed increase in total energy expenditure with respect to the total energy expenditure at the aerodynamic optimum.

The noise levels presented in the results are given in terms of the TSSP. Given that the diameter and the thrust are constrained for both climb and cruise, direct relations can be defined between the TSSP and SPL for the two mission segments, and are provided here for reference such that the presented noise values can be interpreted in terms of SPL as well.

$$SPL_{climb} = TSSP_{climb} + 145.3 \text{ dB} \tag{9.1}$$

$$SPL_{cruise} = TSSP_{cruise} + 140.6 \text{ dB} \tag{9.2}$$

As mentioned in section 7.3, the total twist angle of a blade section is made up out of two components, namely the twist distribution θ, which is then translated over the entire length of the blade by adding the collective pitch angle β. Because of practical reasons, the twist distribution θ was constrained to be zero degrees at the tip during optimization, such that the total twist angle at the tip would be equal to the collective pitch angle β. However, it is conventional among propeller design literature that the twist distribution θ is constrained to be 0 degrees at 70% of the blade radius, such that the total twist angle at 70% blade radius would be equal to the pitch angle β. For this reason, the acquired optimization results were adapted to fit this convention, and will be presented as such.

A number of terms should be clarified before proceeding. When discussing the efficiency, it should be noted that only the propeller is considered, meaning that all the quantities are defined at the shaft. Typical losses in the power train, such as engine or transmission losses, are not accounted for.

In the discussions of the results, sometimes the term "installed propeller" or "installed design" will be used. When these terms are used, the author refers to the propeller designs that were optimized in the specified non-uniform flow.

Finally, the discussion of the results will contain a discussion of different efficiency components, namely induced and profile efficiency. How these components were calculated has been discussed in section 5.2.2. To be clear in the discussion however, it is helpful to explain more clearly what is meant by the profile efficiency. The profile efficiency is a measure of the losses due to profile drag. The equation for the profile efficiency as presented in section 5.2.2 is repeated here[37].

$$\eta_{prof} = \frac{1 - \frac{c_d}{c_l}\frac{V_a}{V_t}}{1 + \frac{c_d}{c_l}\frac{V_t}{V_a}} \tag{9.3}$$

If the lift-to-drag ratio would be infinite, the profile efficiency would be 1. The profile efficiency thus decreases with a decrease in lift-to-drag ratio. How much the lift-to-drag ratio impacts the thrust-to-torque ratio (which essentially determines the overall propeller efficiency) is influenced by the inflow angle, which is represented in the equation by the ratio of the axial and tangential velocities V_a and V_t. This means that for a fixed freestream velocity, an increase in the advance ratio will lead to an increase in the inflow angle, and therefore would contribute to a higher profile efficiency.

9.2.1 Uniform Inflow

This subsection presents the results of the design optimization studies for propellers in a uniform flow. In the presentation, the designs that were optimized in a uniform flow will sometimes be referred to as the isolated designs.

Aerodynamic Optimization

The objective of the aerodynamic optimization was to minimize energy expenditure during the specified mission. Propeller designs with 3, 4, 5 and 6 blades were optimized with this objective. The results are plotted in the left graph of figure 9.1, which shows the trend of the optimized energy consumption with increasing blade count. In this graph, the energy expenditure for each category (climb, cruise, total) is normalized with respect to the energy expenditure of that category for the optimized three-bladed design.

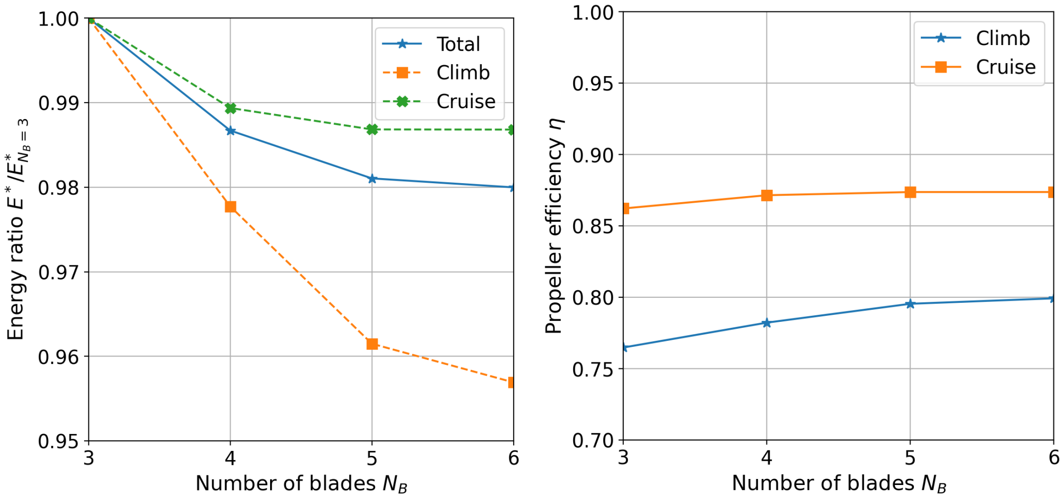

Fig. 9.1 Normalized energy expenditure (left) and propeller efficiency (right) for increasing blade counts.

The results clearly show a decrease in energy expenditure with increasing blade count. This decrease in energy expenditure is due to an increase in efficiency, as the right graph of figure 9.1

shows. An increase in blade count thus leads to a higher efficiency, and therefore a lower energy expenditure. To find out how exactly the increase in blade count leads to a higher efficiency, it is helpful to look at the efficiency components, induced and profile efficiency, which have been plotted in figure 9.2 for all blade counts, and for climb and cruise separately.

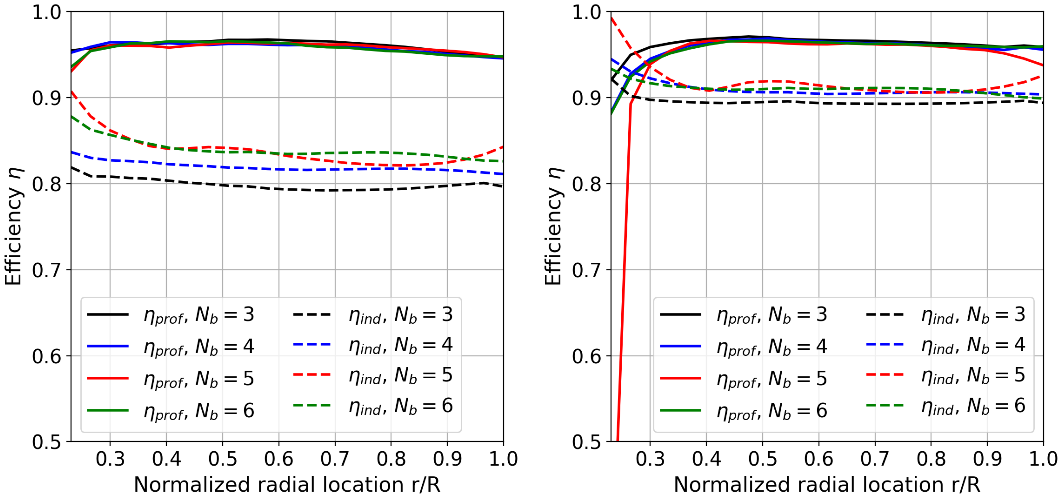

Fig. 9.2 Radially distributed induced and profile efficiencies for different blade counts in climb (left) and cruise (right).

The results in the figure indicate that the increased efficiency is almost entirely due to an increase in induced efficiency, while the profile efficiency remains nearly unchanged. Recalling the equation for induced drag ($C_{D,i} = C_L^2/\pi ARe$), this decrease in induced efficiency is likely to be caused either by a decrease in loading (C_L), or an increase in aspect ratio (AR). Figure 9.3 demonstrates that there is indeed a significant decrease in blade loading, both in terms of lift and drag. In this figure, the local lift- and drag loading are plotted ($L_{loc} = C_l \cdot c \cdot q_{loc}$ & $D_{loc} = C_d \cdot c \cdot q_{loc}$), using the local dynamic pressure found at that radial coordinate r/R, and the values are normalized with respect to the freestream dynamic pressure and the propeller diameter.

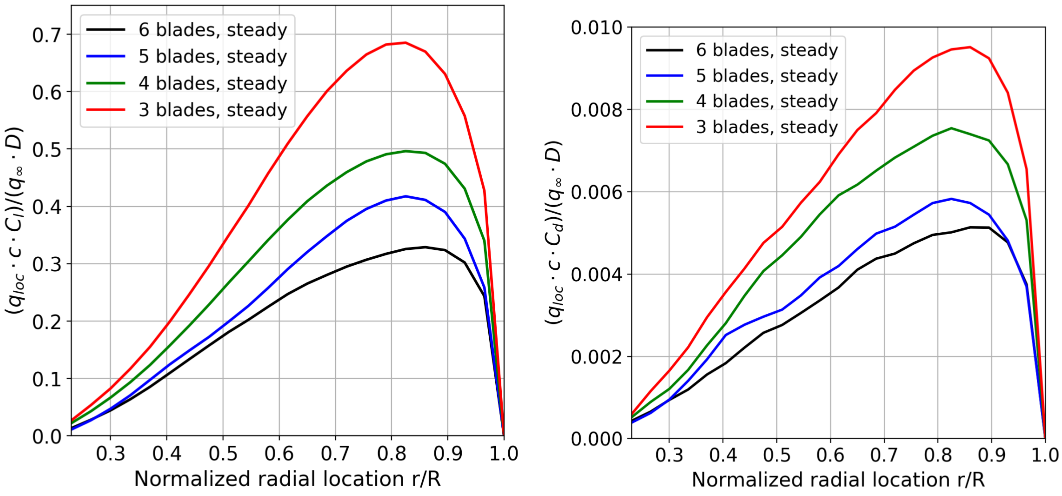

Fig. 9.3 Radially distributed lift- (left) and drag loading (right) for different blade counts in climb condition, normalized with respect to the product of the freestream dynamic pressure and the propeller diameter.

Moreover, figure 9.4 shows that the aspect ratio also increases, since the chord length decreases with increasing blade count, while the blade span remains constant, which means that both the decrease in loading and the increase in aspect ratio play a role in reducing induced losses. The decrease in lift- and drag loading can be explained as follows. For all blade counts, the thrust requirement and therefore the disk loading remains the same for both flight phases. When increasing the blade count, a lower blade loading is necessary to meet the thrust requirement, and thus the blade loading decreases with increasing blade count.

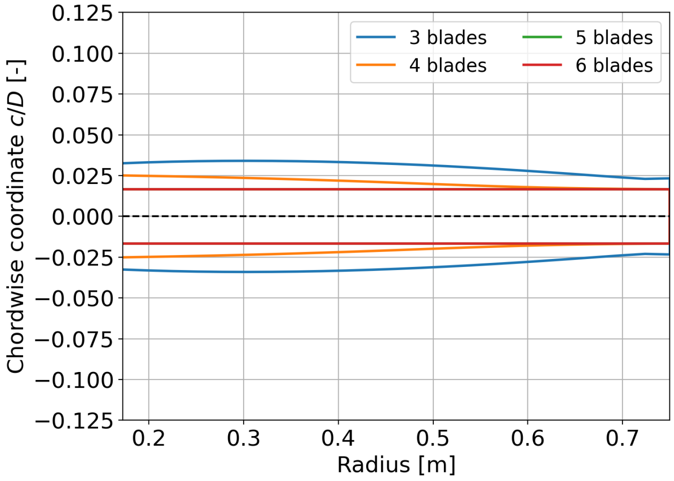

Fig. 9.4 Untwisted planforms for different blade counts.

Going back to figure 9.1, another two observations can be made. The first observation is that the increase in efficiency is larger for climb than for cruise. This can be explained by the thrust requirement, which is higher for climb than for cruise. As a result, an increase in blade count results in a larger reduction of the absolute blade loading in climb compared to cruise, and therefore larger increases in induced efficiency. The second observation is that the improvement in efficiency is flattening rapidly with increasing blade count, and is nearly flat already between the five- and six-bladed propeller designs, especially considering the range of the y-axis on the right graph in figure 9.1. This is mainly due to two reasons. Firstly, the relative decrease in blade loading becomes smaller with increasing blade count, thereby reducing the decrease in induced losses with increasing blade count. The second reason is that the chord length is already at its lower bound for the five-bladed design, and can thus not be decreased even more for the six-bladed design (see figure 9.4), which means that the aspect ratio is already at its maximum for the five-bladed propeller and cannot contribute anymore to the reduction of induced losses.

Next the trend of the other design variables will be discussed, starting with the advance ratio, which can be seen in figure 9.5. While the advance ratio remains at or near the lower bound for climb ($J_{lb} = 0.76$) for all blade counts, the cruise advance ratio increases with blade count.

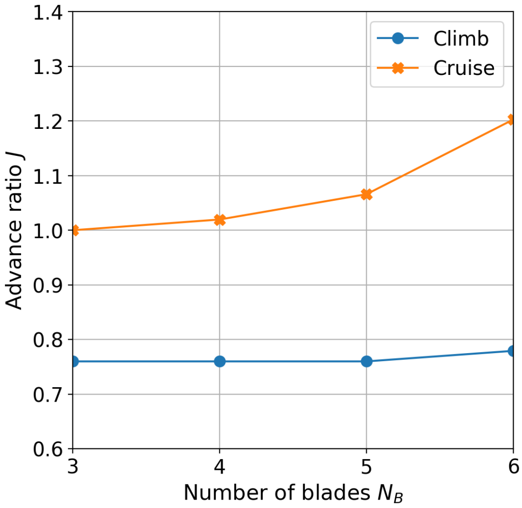

Fig. 9.5 Advance ratios at climb and cruise for different blade counts.

The advance ratio mainly influences the blade loading through two mechanisms. The first mechanism is through its influence on the inflow angle ϕ (see figure 2.1 for its definition). An increase in advance ratio with a constant freestream velocity means a decrease in the rotational velocity, and subsequently an increase in the inflow angle ϕ. Equation 9.4 shows the relationship between the local thrust T', and the local blade loading in terms of lift and drag. When the inflow angle ϕ increases, the cosine term decreases while the sine term increases, leading to a decrease in the local thrust that is produced.

$$T' = L' \cos\phi - D' \sin\phi \tag{9.4}$$

The second mechanism by which the advance ratio influences the blade loading is through its effects on the dynamic pressure. As mentioned, for a given freestream velocity (and constant diameter), a change in advance ratio leads to a change in rotational velocity. Increasing the advance ratio means a lower rotational velocity, and therefore a decrease in the dynamic pressure. This can lead to a decrease in both the lift and the drag loading. By staying close to the lower bound, the climb advance ratio is such that it maximizes dynamic pressure and minimizes the inflow angle ϕ, both of which are beneficial to maximize the produced thrust. This is necessary since the thrust requirement for climb is significantly higher than that of cruise (480 N for cruise and 830 N for climb). For cruise on the other hand, advance ratio increases with increasing blade count. This increase in advance ratio is required to decrease the produced thrust per blade with increasing blade count, since the cruise thrust requirement is easily met, especially given that the cruise freestream velocity is higher, therefore contributing to a higher dynamic pressure compared to the climb dynamic pressure from the start.

The following design variables to observe are the collective pitch angle and the twist distribution, both plotted in figure 9.6. As can be seen, the twist angle distribution barely changes between blade counts, and is therefore inconsequential in terms of its effects on the results. For the pitch on the other hand, a decrease can be seen in its value for climb with increasing blade count, while an increase is observed for the cruise value.

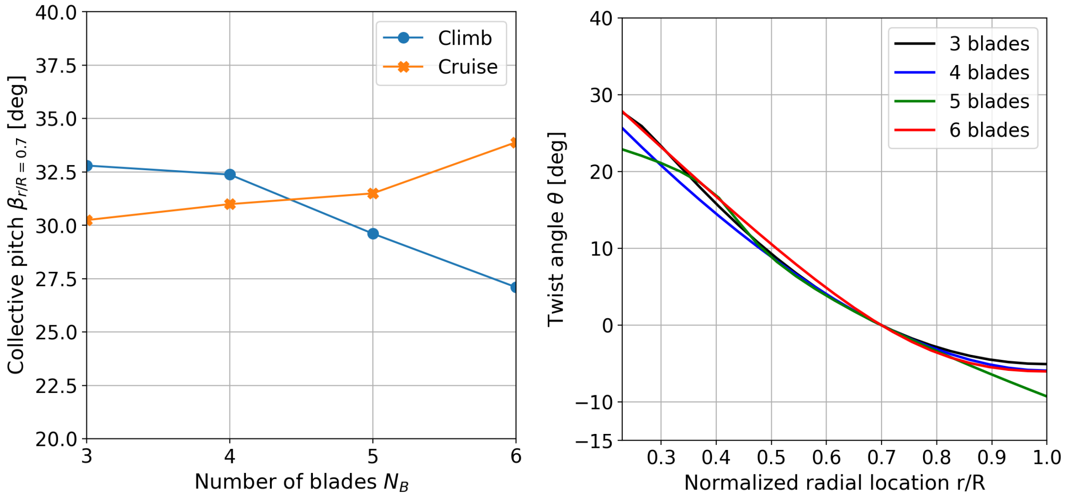

Fig. 9.6 Collective pitch at r/R = 0.7 (left) and twist distribution θ with $\theta_{r/R=0.7} = 0$ (right) for different blade counts.

Referring back to figure 2.1, it is known that the pitch angle can be decomposed in the inflow angle ϕ and the angle of attack α.

$$\beta = \phi + \alpha \tag{9.5}$$

As discussed earlier, the cruise advance ratio increases with increasing blade count, which leads to an increase in the inflow angle ϕ. The cruise pitch angle β follows a very similar trend compared to the cruise advance ratio, namely a steady increase with increasing blade count. This indicates that the pitch angle was increased alongside the inflow angle, such that the angle of attack remained relatively stable. For climb on the other hand, the advance ratio, and thus the inflow angle ϕ, remained almost unchanged for all blade counts. At the same time the climb pitch angle is decreasing with increasing blade count, indicating that the angle of attack in climb is decreasing with increasing blade count. The change in pitch is mainly used to control the angle of attack, such that the angle of attack is as close as possible to the angle of attack for maximum lift-to-drag ratio, which is beneficial for the profile efficiency.

As could be seen earlier in figure 9.2, the profile efficiency remained almost unchanged with increasing blade count. The profile efficiency is dependent on two things, namely the lift-to-drag ratio, and the ratio between the axial and tangential velocity (see equation 9.3). Figure 9.7 shows that the lift-to-drag ratio decreases in both climb and cruise with increasing blade count. The reason for this is twofold. Firstly, the lift loading decreases faster than the drag loading with increasing blade count, resulting in a lower lift-to-drag ratio. Secondly, the Reynolds number decreases with increasing blade count, as can be seen in figure 9.8. A decrease in Reynolds number typically means that the maximum achievable lift-to-drag ratio decreases as well. However, at these values for the advance ratio (e.g $J = 0.76$) and lift-to-drag ratio (e.g. $c_l/c_d = 60$), even a 10% decrease in lift-to-drag ratio makes a very minor (<1%) difference in terms of the profile efficiency.

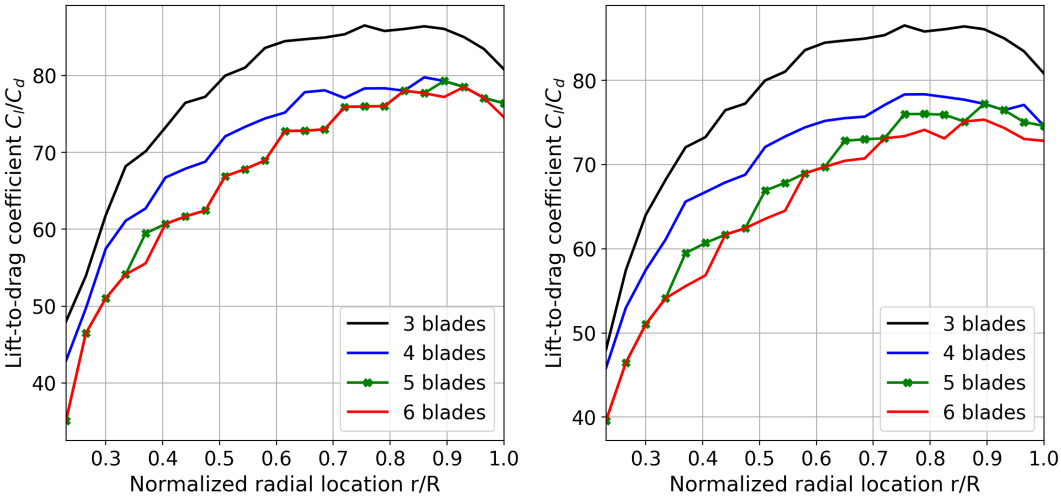

Fig. 9.7 Lift-to-drag coefficient distribution in climb (left) and cruise (right) for different blade counts.

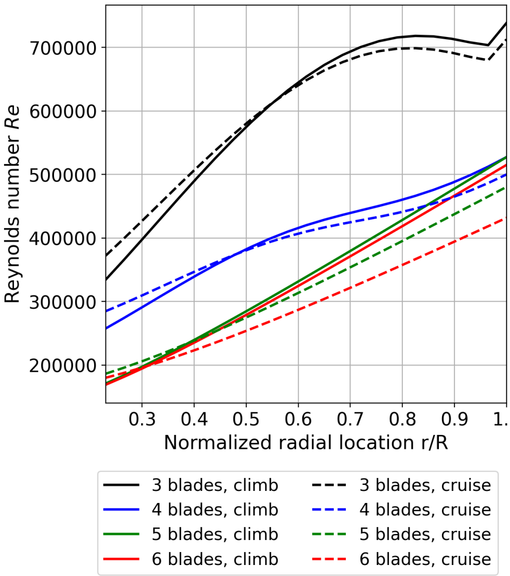

Fig. 9.8 Reynolds number distribution in climb and cruise for different blade counts.

The final design parameter which to take a look at is the solidity σ. The progression of this parameter with increasing blade count is plotted in figure 9.9. As the figure shows, the solidity decreases between the three- and four-bladed propeller, while it remains stable between the four- and five-bladed propeller. This indicates that between the three- and four-bladed propeller, the chord decrease was proportionally larger compared to the chord decrease between the four- and five-bladed propeller. Arguably, the reason for this is that the decrease in blade loading between a three-bladed and four-bladed propeller is larger than the decrease in blade loading between a four- and five-bladed propeller. The climb advance ratio is kept at a minimum to minimize the inflow angle ϕ, which helps to meet the thrust requirement in climb. As a result, the climb dynamic pressure is at its maximum. The decrease in lift loading in climb thus leads to either a decrease in the lift coefficient C_l, or the chord length c, given that the blade lift is equal to $L = C_l \cdot c \cdot q$. The decrease in the lift coefficient needs to be kept to a minimum as to limit the impact on the lift-to-drag ratio, and thereby the profile efficiency. Therefore, the decrease in loading might be leading mostly to a decrease in chord, and since the decrease in loading is larger between three and four blades compared to four and five blades, there is a relatively larger decrease in chord, which could explain the decrease in solidity between three and four blades. Between five and six blades, the solidity goes up again. This is caused due to the fact that for the five-bladed design, the chord length was already at its lower bound along the blade radius, and could therefore not decrease further for the six-bladed design.

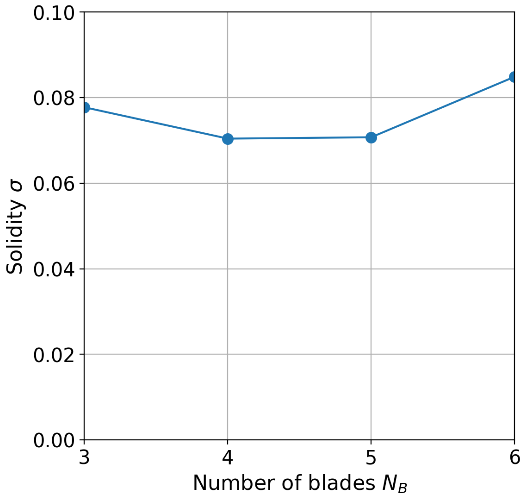

Fig. 9.9 Solidity for different blade counts.

Aeroacoustic Optimization

Before discussing the results, it should be reiterated that the noise levels that are presented represent an average of the noise levels measured at three locations (three observation angles) during the climb phase only. No noise estimations were done for the cruise phase, as the noise emissions during climb were considered to be most relevant with respect to noise pollution around airports, while cruise noise is generally not relevant in this matter.

The objective of the aeroacoustic optimization was to minimize the noise for a given maximum mission energy expenditure, which was introduced as a constraint that allowed a 1%, 2%, or 5% increase in energy expenditure compared to the energy expenditure of the aerodynamic optimum design for that blade count (these allowed percentage increase factors will be referred to as penalty factors). For the aeroacoustic optimization, only a three- and four-bladed propeller were optimized. For every percentage of allowed increase in energy expenditure (1%, 2%, or 5%), a separate design was optimized. The left graph in 9.10 shows the trend of all optimized three- and four-bladed propeller designs in terms of TSSP with respect to the total energy expenditure. On the y-axis of the left plot, the noise reduction is measured with respect to the noise levels of the three-bladed aerodynamic optimum design, while on the x-axis, the energy expenditure is normalized with respect to the total expenditure of the three-bladed aerodynamic optimum design. The four markers from left to right correspond to the aerodynamic optimum, a 1%, 2%, and 5% allowed increase in total energy expenditure with respect to the aerodynamic optimum energy expenditure of the design with the same blade count. As becomes directly apparent, the four-bladed propeller outperforms the three-bladed propeller significantly in terms of aeroacoustic performance, as well as aerodynamic performance. The right plot of figure 9.10 shows how the efficiency changes with increasing energy penalty. As can be seen, the efficiency decreases linearly with energy penalty, but decreases faster for climb compared to cruise. Furthermore it can be seen that the three- and four-bladed design follow the exact same trend when it comes to the reduction in efficiency.

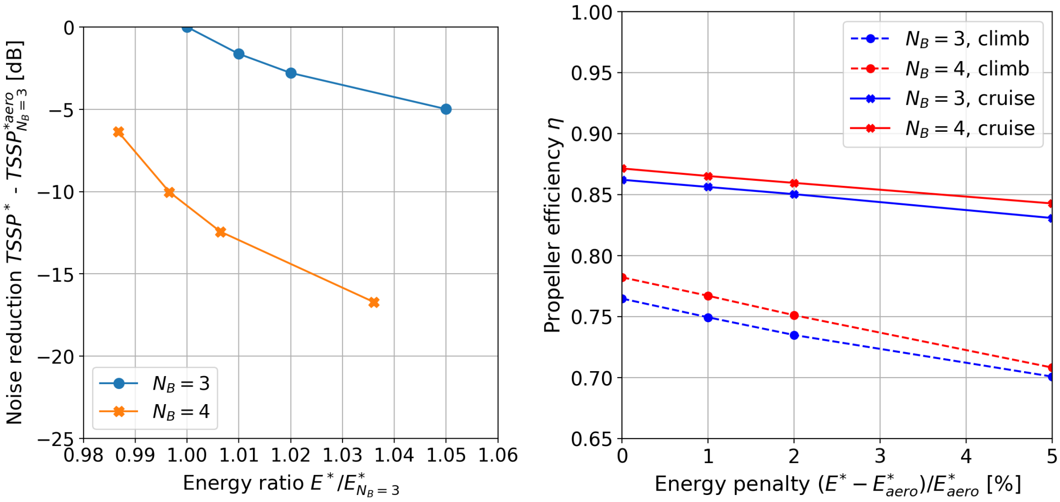

Fig. 9.10 Normalized TSSP versus energy expenditure (left) and propeller efficiency versus energy penalty (right).

Next, it is key to find out what caused the reduction in noise with increasing energy penalty, and how a higher blade count could lead to an even larger reduction in noise. Considering again the expressions for acoustic pressure derived in the HST model (see section 6.2), two major contributors to noise can be distinguished, namely the blade loading and the tip Mach number. While an increase in blade loading increases only its specific related noise component (e.g. an increase in lift loading increases lift loading noise), the tip Mach number influences the noise from all sources. The tip Mach number is found in the argument of the Bessel's function, which influences the radiation efficiency of the noise from all sources. The higher the tip Mach number, the higher the radiation efficiency, which typically increases the noise experienced by the observer (disregarding any possible cancellation effects for the purpose of this explanation). Given that a noise reduction has taken place for both the three- and the four-bladed propeller with increasing energy penalty, the next step is to establish what caused this noise reduction. In the right graph of figure 9.11, the tip Mach number is plotted for the three- and four-bladed propellers with respect to the energy penalty, while the left graph shows how the climb and cruise advance ratios changes with energy penalty for all optimized designs. Figure 9.12 thereafter shows the local lift loading for each of the optimized design in climb (left graph) and cruise (right graph), here normalized with respect to the freestream dynamic pressure times the propeller diameter.

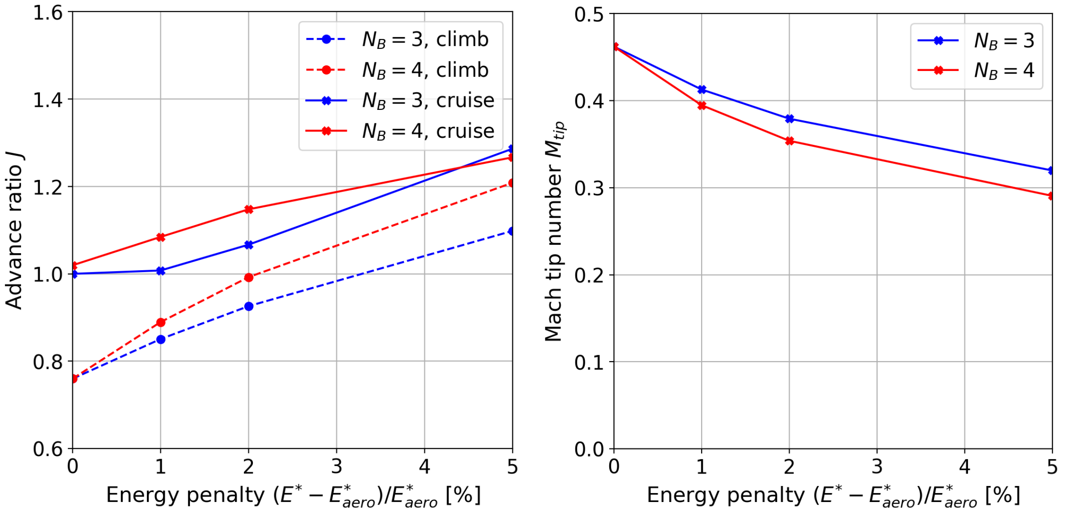

Fig. 9.11 Climb & cruise advance ratio’s (left) and tip Mach number (right) versus energy penalty.

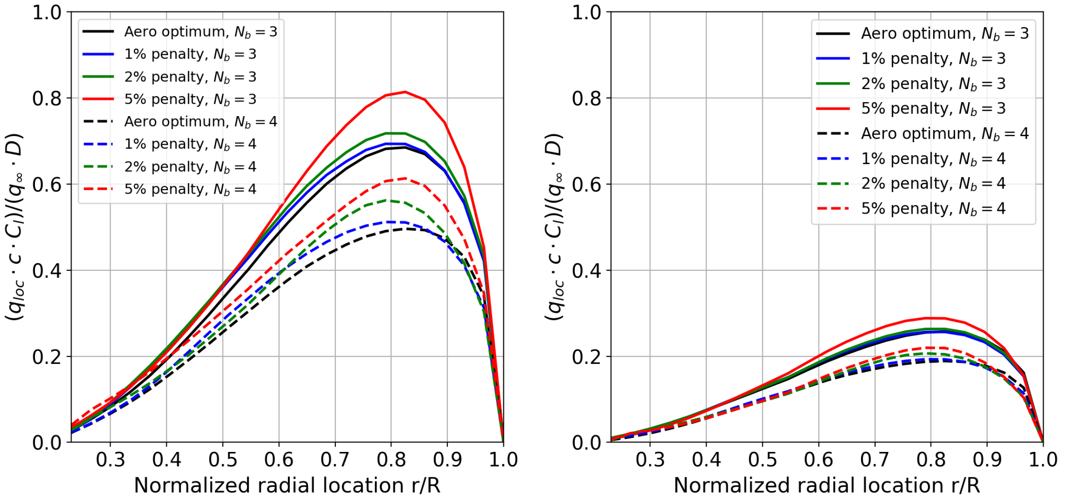

Fig. 9.12 Normalized blade lift distribution in climb (left) and cruise (right) for different penalty levels.

As both figures show, the tip Mach number decreases with energy penalty, while the local lift loading increases with energy penalty. An increase in blade loading would typically lead to an increase in noise due to the associated pressure jump across the blades, but instead a reduction in noise is observed. This can be explained by the reduction in the tip Mach number (see figure 9.11). As the results clearly indicate, the effect of the reduction in tip Mach number outweighs the effect of an increase in blade loading on noise, since a reduction in noise is realized with increasing energy penalty despite increasing blade loading. The blade count impacts the noise performance in two ways. Firstly, increasing the blade count can reduce the blade loading, depending on the solidity of the propellers that are compared. Figure 9.17 shows the solidity of the three- and four-bladed propeller designs, and their trend with increasing energy penalty. As can be seen, the solidity levels are very similar at the first three markers (aerodynamic optimum, 1%, and 2%), but slightly deviate at 5% energy penalty. At the same solidity, a higher blade count has a smaller blade area, as can be seen in figure 9.14, which compares the untwisted blade planforms of the three- and four-bladed propeller designs at all penalty levels. Given the same thrust requirement, and at similar solidity levels, a higher blade count leads to lower blade loading. This allows a larger increase in the advance ratio, which reduces the tip Mach number even further. Secondly, a higher blade count leads to increased acoustic interference between pressure signals from the individual propeller blades, leading to a net reduction in noise[10].

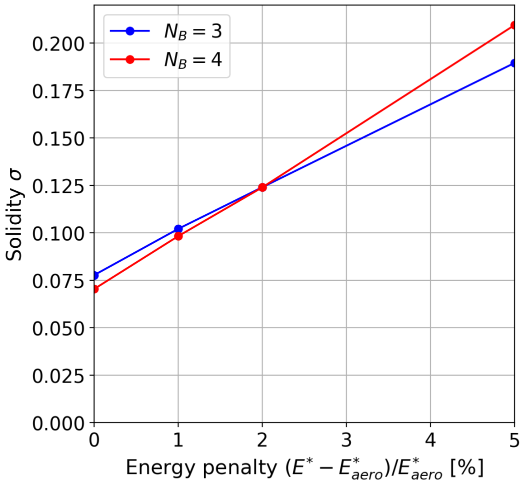

Fig. 9.13 Solidity of the three- and four-bladed propellers at different penalty levels.

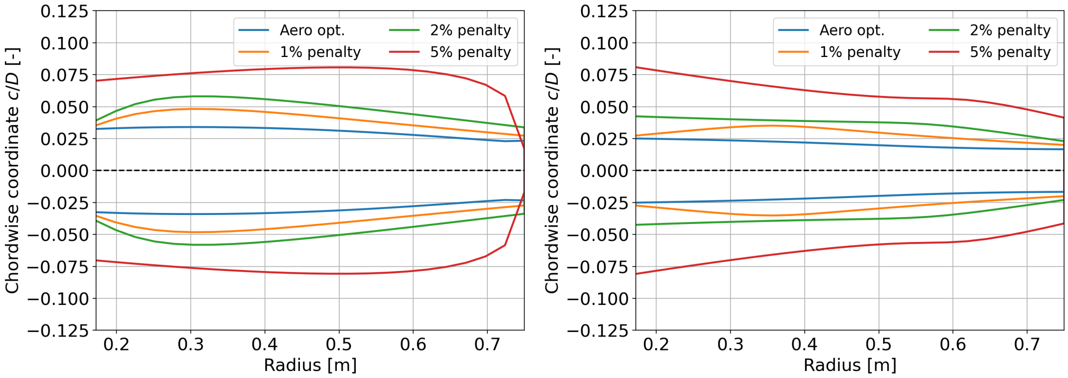

Fig. 9.14 Untwisted blade shapes for the optimized three- (left) and four-bladed propeller (right) at different penalty levels.

To reduce noise, a reduction in tip Mach number is thus deemed the most effective tool. To realize this, the advance ratio is increased, since this is the only measure to reduce the effective velocity at the tip, given that the diameter and freestream velocities for each flight phase are fixed. The increase in advance ratio causes the blades to spin slower, which results in a higher inflow angle ϕ. From BEM theory it is known that the local thrust can be calculated by:

$$T' = L' \cos\phi - D' \sin\phi \tag{9.6}$$

$$\phi = (\beta + \theta) - \alpha \tag{9.7}$$

The thrust requirement is constrained for both flight phases. The increase of the inflow angle ϕ causes a smaller cosine term and a larger sine term, explaining the necessity for the lift loading L' to increase in order to still meet the thrust requirement. Specifically during climb this increase in lift is required, since the thrust requirement is significantly higher, and the relative increase in climb advance ratio is higher compared to that of cruise (see figure 9.11). With the noise reduction comes a significant reduction in propeller efficiency, in particular for the climb phase, as was shown in the right graph of figure 9.10. Since the climb phase has a smaller influence on the total energy expenditure due to its shorter duration, but is the only phase for which aeroacoustic performance is measured and optimized, it makes sense this phase sees the largest penalty in efficiency.

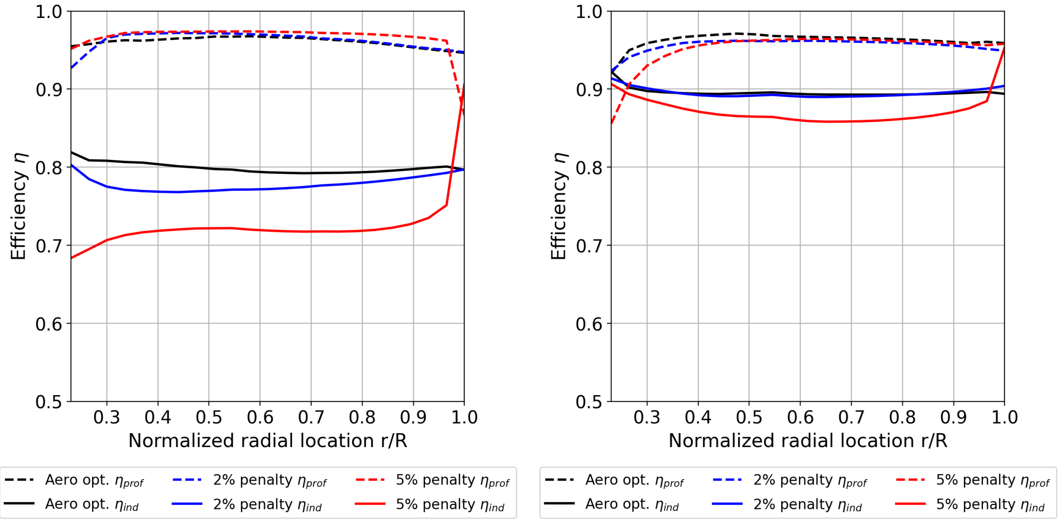

Fig. 9.15 Profile- and induced efficiency distributions for different penalty levels in climb (left) and cruise (right) for an optimized three-bladed propeller.

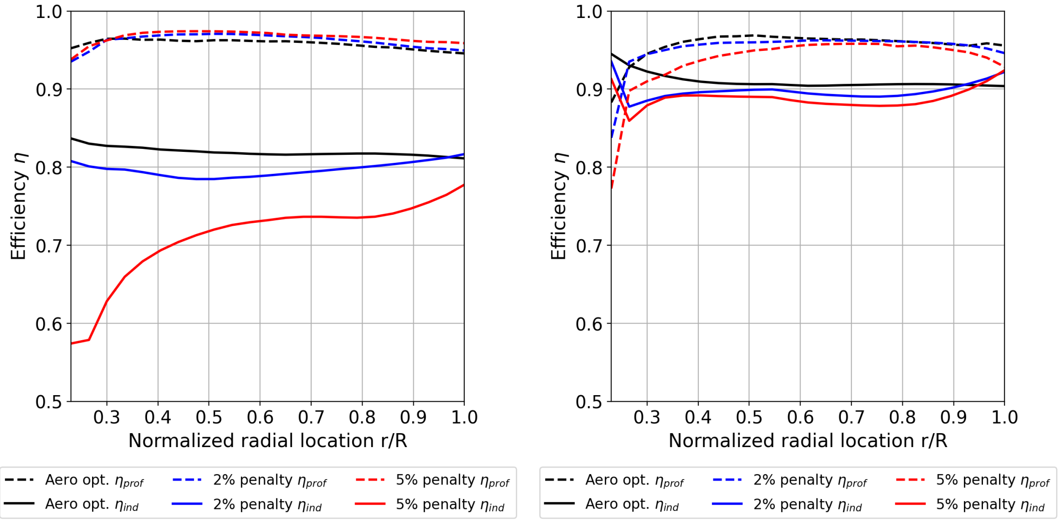

Fig. 9.16 Profile- and induced efficiency distributions for different penalty levels in climb (left) and cruise (right) for an optimized four-bladed propeller.

Next, it is interesting to observe how to efficiency is reduced exactly, by looking at the efficiency components, induced and profile efficiency. For the climb phase, the reduction in efficiency is clearly due to induced losses, as demonstrated by figures 9.15 and 9.16. This corresponds with the increase in the blade lift loading seen for both blade counts during the climb phase, as was presented earlier in figure 9.12. The profile efficiency remains fairly constant and even slightly increases with increasing noise penalty. For cruise on the other hand, the increase in lift loading is almost negligible up to a penalty of 2%, especially for the three-bladed propeller. Only at 5% a definite increase in loading can be seen in figure 9.12, and the accompanying dip in induced efficiency in figures 9.15 and 9.16. The loss in efficiency is minimized in the cruise phase, such that more energy could be 'wasted' on improving noise performance in the climb phase. For the three-bladed design, losses mostly occur in terms profile efficiency at a 2% penalty, and in terms of induced efficiency at a 5% penalty. For the four-bladed case, the the loss in efficiency comes from a combination of the two.

As discussed earlier in this section when observing the results for aerodynamic optimization, the profile efficiency is determined by two factors, the lift-to-drag ratio, and the velocity ratio $V_\infty/\Omega r$ (see also section 5.2.2). Figures 9.15 and 9.16 show that the profile efficiency increases very slightly in climb with increasing energy penalty for both blade counts, but reduces slightly for cruise. In figure 9.11 it was observed that the advance ratio increased with increasing energy penalty for both blade counts, which for a constant freestream velocity means a reduction in rotational velocity, and thereby an increase in the aforementioned velocity ratio. This partly explains the slight increase in profile efficiency with increased energy penalty during climb. However, despite the increase in advance ratio for both climb and cruise, the profile efficiency during cruise slightly reduces with increasing energy penalty for both blade counts. The reason for this might be explained using figure 9.17. The left graph in this figure shows that for cruise, the lift-to-drag ratio decreases with increasing energy penalty, while a marginal increase can be seen for the lift-to-drag ratio in climb. In the right graph, a significant increase is observed in the climb pitch angle, while for the cruise pitch angle an initial decrease, and subsequent marginal increase can be seen for both blade counts. It should be noted that the twist angle θ does not significantly differ between all designs considered here, and is therefore not shown. With an increase in advance ratio for a constant freestream velocity comes an increase in the inflow angle ϕ. Consider again the relationship between the angles shown in equation 9.8. For climb, the pitch angle rises with increasing energy penalty, just like the inflow angle ϕ, which therefore keeps the angle of attack α relatively constant. For cruise however, the angle of attack decreases, since the inflow angle ϕ increase while the collective pitch angle β decreases, or increases only slightly with increasing energy penalty. This decrease in angle of attack during cruise is likely to have contributed to the decrease in lift-to-drag ratio during that flight phase.

$$(\beta+\theta)=\phi+\alpha \tag{9.8}$$

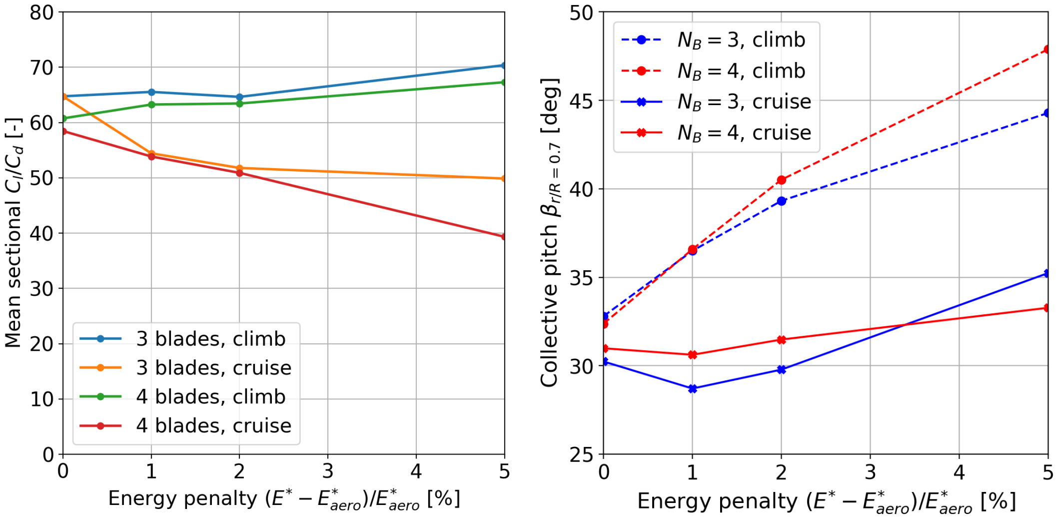

Fig. 9.17 Mean lift-to-drag ratio (left) and collective pitch at r/R = 0.70 (right) for different penalty levels.

It is likely that the chord increased to offset the increase in advance ratio in particular for climb, since the climb thrust requirement is higher. For cruise on the other hand, this increase in chord was so high that the thrust requirement could be met more easily. As a result, both the lift coefficient and dynamic pressure could be lower to achieve the right lift loading. An increase in advance ratio would negatively impact the induced efficiency more through its impact on the inflow angle ϕ which would require a higher lift force in order to meet the thrust requirement (see equation 9.6), while a change in the pitch angle β could change the angle of attack to achieve a lower lift-to-drag ratio, which would effect the profile efficiency more. Since the advance ratio influences both efficiency components through its impact on the inflow angle ϕ, a balance was found by the optimizer leading to the least combined losses during cruise, which explains the combination of reduction in both profile and induced losses during cruise with increasing energy penalty for both blade counts.

Figures 9.18 and 9.19 show the directivity plots for the aerodynamic optimum (left) and the 5% noise penalty (right) of the three- and four-bladed propeller. Comparing left and right gives an insight in the development of the different noise components. As can be observed, lift noise is dominant at the aerodynamic optimum, and remains dominant in the 5% energy penalty case. The volume component barely changes, while the lift and drag noise components decrease. Despite an increase in lift and drag loading during climb, the noise decreases, because all noise components scale with the tip Mach number, which decreases. The decrease in tip Mach number thus has a bigger impact than the increase in loading, as established earlier. While the volume noise might increase slightly due to the increase in solidity, it also scales with the tip Mach number, the result is that the two effects cancel each other out and the volume noise component remains almost unchanged. Comparing figure 9.18 and 9.19, it can be seen that these trends are similar for both blade counts.

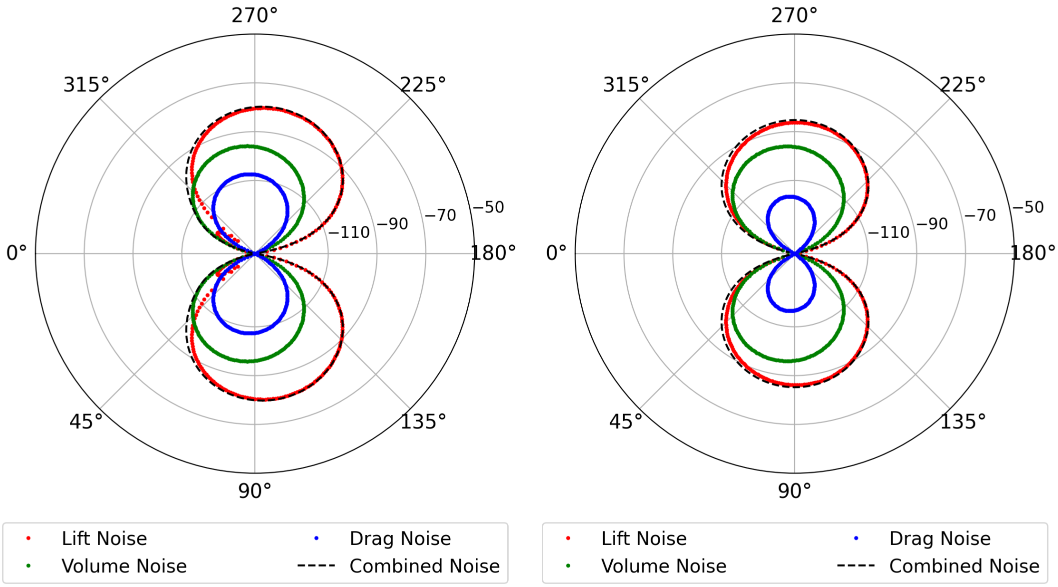

Fig. 9.18 TSSP directivity plot with respect to observer angle θ at the aerodynamic optimum (left) and with a 5% energy penalty (right) for an optimized three-bladed propeller.

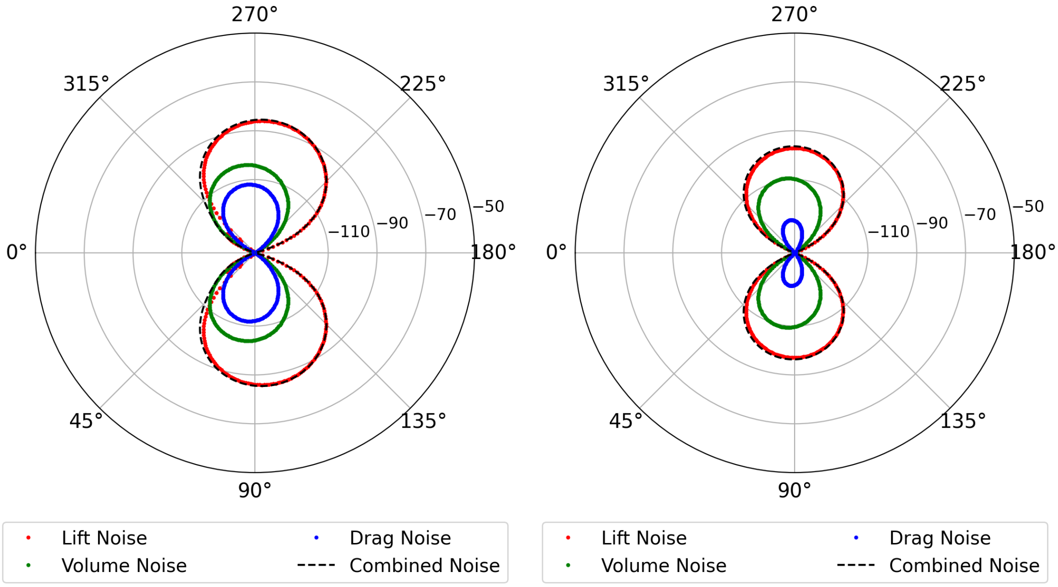

Fig. 9.19 TSSP directivity plot with respect to observer angle θ at the aerodynamic optimum (left) and with a 5% energy penalty (right) for an optimized four-bladed propeller.

As the directivity plot shows, the noise is highest in the plane of the propeller, and goes to zero right in front or behind the propeller. Going back to Hanson's formulation, this makes sense, given that sine terms in the numerator go to zero at 0° and 180°, and the cosine terms in the denominator go to zero at 90° and 270°, which eliminates the $M_x \cos\theta$ term and leads to the maximum value possible in the denominator. Table 9.3 provide an overview of the results. It should be noted that the magnitude of the noise could be inaccurate with the models used, but that the difference in noise can be interpreted with more confidence, given that the models used are deemed to be able to accurately predict trends. As the table shows, and visualized in figure 9.10, the noise reduction trend is flattening slightly with increasing penalty, but there are still noise improvements that can be made for energy penalties above 5%. The reduction in efficiency affects the climb phase more than the cruise phase, which in this study is only 5 times the duration of the climb phase. For a lot of flights, the cruise phase is much more than 5 times longer than the climb phase, while for others it might be shorter. For all those cases, a balance has to be found between the necessary or desired noise reduction and the acceptable reduction in efficiency.

Table 9.3 TSSP values and change with respect to the TSSP at the aerodynamic optimum at different energy penalty levels.

	3 blades		4 blades	
Penalty	TSSP [dB]	diff w.r.t. aero opt. [dB]	TSSP [dB]	diff w.r.t. aero opt. [dB]
0%	-83.33	0	-89.69	0
1%	-84.96	-1.63	-93.36	-3.67
2%	-86.12	-2.79	-95.76	-6.07
5%	-88.32	-4.99	-100.04	-10.35

9.2.2 Non-Uniform Inflow

This subsection will cover the results for the propeller exposed to a non-uniform flow. In this study, an inflow under an angle of attack of 5 degrees was studied. Similar to the propeller in isolated conditions, a three-, four-, five-, and six-bladed propeller design was optimized for aerodynamic optimization, while for noise optimization only a three- and four-bladed design were optimized. A comparison will be made to the result from the isolated optimization studies presented above. In this comparison, three different cases are considered:

1. Isolated propeller design evaluated in uniform inflow (0-deg angle of attack);
2. Isolated propeller design evaluated at an inflow under a 5-deg angle of attack;
3. Installed propeller design evaluated at an inflow under a 5-deg angle of attack;

It should be noted that when the isolated propeller design is evaluated at an inflow under a 5-deg angle of attack, the thrust slightly increases, thereby exceeding the constraints originally put on the design. This increase does remain small, with an increase of about 0.5% for cruise, and 1% for climb. Given this situation and the influence of the thrust on the energy expenditure, no direct comparisons that include energy consumption are made. When regarding the results of the propeller operating in non-uniform flow, it should be noted that the data has been time-averaged over one propeller rotation.

Aerodynamic Optimization

For the aerodynamic optimization, the objective was to minimize the total energy expenditure, which is a sum of the energy expenditure of the climb and the cruise phase. Given that the operating freestream velocity, thrust, and mission segment time were fixed for both climb and cruise, the energy expenditure of these flight phases is controlled through the efficiency factor. Figure 9.20 shows the comparison of propeller efficiencies for different blade counts, and the three aforementioned cases. The efficiency vales plotted in this figure are also presented in tables 9.4 and 9.5.

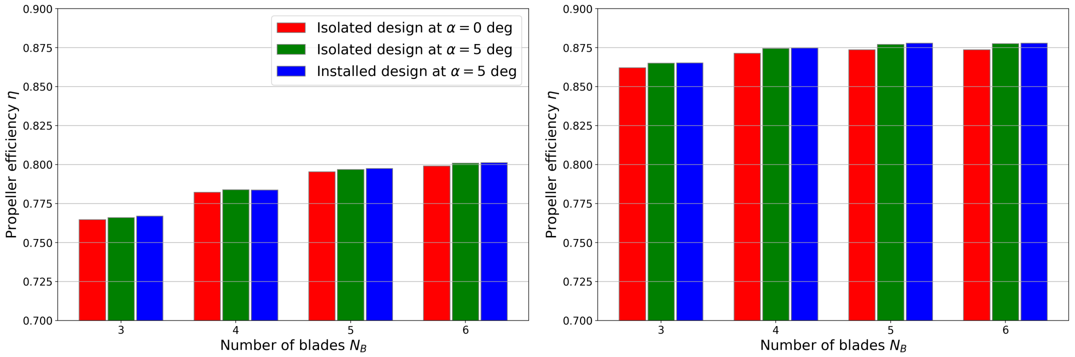

Fig. 9.20 Impact of a 5-deg angle of attack on optimized propeller efficiency in climb (left) and cruise (right).

Table 9.4 Climb efficiency comparison of the isolated design, the isolated design operating in non-uniform flow (inflow under an AoA), and the installed design operating in non-uniform flow, for different blade counts.

	iso. design	iso. design at AoA		inst. design at AoA		
N_b	η	η	% diff w.r.t. iso design	η	% diff w.r.t. iso design	% diff w.r.t. iso design at AoA
3	0.765	0.766	0.16%	0.767	0.30%	0.14%
4	0.782	0.784	0.21%	0.784	0.19%	-0.02%
5	0.796	0.797	0.20%	0.798	0.27%	0.07%
6	0.799	0.801	0.21%	0.801	0.25%	0.04%

Table 9.5 Cruise efficiency comparison of the isolated design, the isolated design operating in non-uniform flow (inflow under an AoA), and the installed design operating in non-uniform flow, for different blade counts.

	iso. design	iso. design at AoA		inst. design at AoA		
N_b	η	η	% diff w.r.t. iso design	η	% diff w.r.t. iso design	% diff w.r.t. iso design at AoA
3	0.862	0.865	0.33%	0.865	0.35%	0.02%
4	0.872	0.875	0.36%	0.875	0.39%	0.03%
5	0.874	0.877	0.38%	0.878	0.49%	0.11%
6	0.874	0.878	0.44%	0.878	0.49%	0.05%

Observing the figure and tables, a slight increase in efficiency can be seen for the designs (both the isolated and installed designs) operating at an angle of attack, compared to the isolated design operating in uniform flow. This is due to the beneficial upwash experienced by the down-going blade side. However, it can also be observed that the design optimized in non-uniform flow performs only marginally better than the design optimized in uniform flow, when operating in the same non-uniform inflow. In fact, a difference is sometimes hardly observable at all as can be seen in tables 9.4 and 9.5, and in one case the isolated design even performs better when exposed to the flow under a 5-degree angle of attack (climb, 4 blades).

To explain why the designs optimized in uniform flow (isolated designs) perform so similar in the inflow under an angle of attack of 5 degrees compared to the designs optimized while exposed to this inflow under an angle of attack (installed designs), the design variables of the designs need to compared. Figures 9.21 and 9.22 show the advance ratios, collective pitch angles, and solidity for the isolated and installed designs of all blade counts. It should be noted that the twist angle distribution θ is not plotted here, since there were no noticeable difference between the twist distributions of all the designs discussed here. Observing these results, it makes sense that the aerodynamic performance levels are very similar, as the design variables lie very close together and show the same trend.

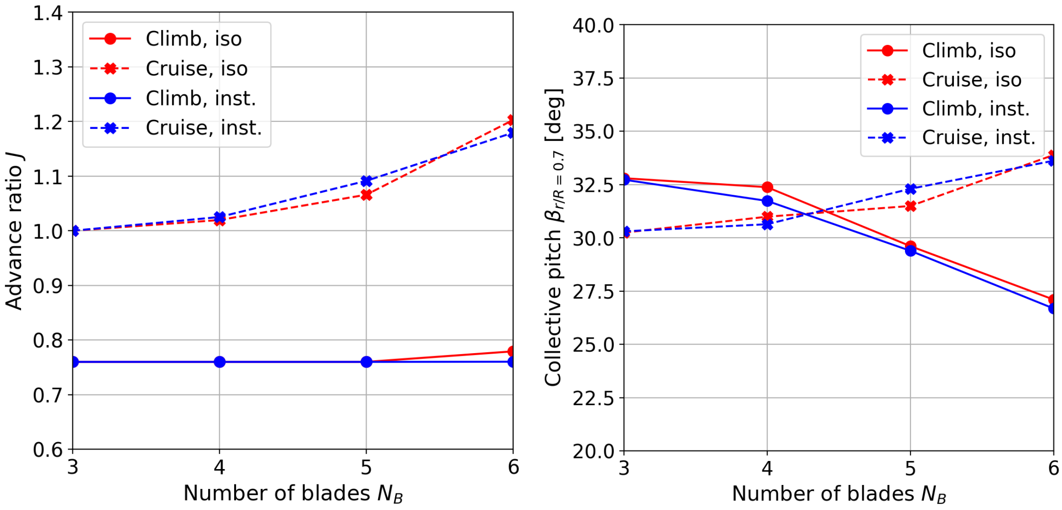

Fig. 9.21 Comparison of the collective pitch $\beta_{r/R=0.7}$ (left) and the climb & cruise advance ratio's (right) of the isolated and installed designs for different blade counts.

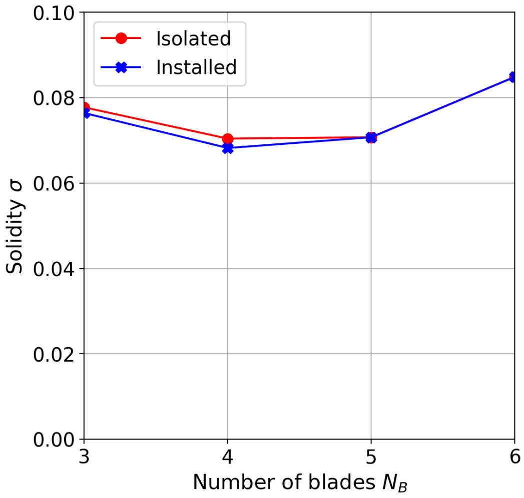

Fig. 9.22 Comparison of the solidity σ of the isolated and installed designs for different blade counts.

As the comparison of the solidity values between the isolated and installed designs suggest, there is very little difference in the chord length distribution of the designs. This is indeed the case, as can be seen in figure 9.23. Aside from a few small changes in the distribution itself, the overall blade area and maximum chord length values are extremely similar, and the differences had no significant effect on the performance outcome.

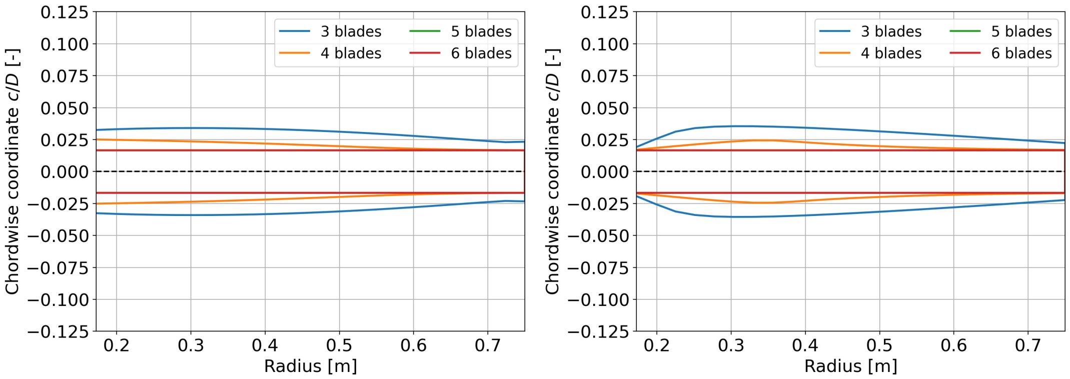

Fig. 9.23 Comparison of the untwisted planforms of the designs optimized for aerodynamic performance in uniform flow (left) and in non-uniform flow (right).

However, despite the fact that there is very little difference in the design variables and the overall aerodynamic efficiency values, there might be a difference in the efficiency components. Tables 9.4 and 9.5 compare the differences in profile and induced efficiencies of the optimized isolated design and the optimized installed design. As can be seen from the differences, there is no clear pattern to be observed that could point to an attempt of the optimizer to focus more on either type of efficiency compared to the isolated design. Based on this data, it can be said that the optimizer followed the same strategy for aerodynamic optimization as in the isolated optimization. The differences are so small, that they are almost indistinguishable from differences that could be caused by noise in the models, or by different starting points for optimization.

Table 9.6 Comparison of the profile and induced efficiency components for optimized isolated and installed propeller designs with different blade counts in climb condition.

	$\eta_{profile}$			$\eta_{induced}$		
N_b	isolated	installed	Δ%	isolated	installed	Δ%
3	0.9607	0.958	-0.29%	0.799	0.805	0.69%
4	0.958	0.953	-0.50%	0.8197	0.823	0.41%
5	0.9577	0.959	0.10%	0.8398	0.836	-0.40%
6	0.9572	0.954	-0.30%	0.84	0.842	0.29%

Table 9.7 Comparison of the profile and induced efficiency components for optimized isolated and installed propeller designs with different blade counts in cruise condition.

	$\eta_{profile}$			$\eta_{induced}$		
N_b	isolated	installed	Δ%	isolated	installed	Δ%
3	0.962	0.962	-0.03%	0.896	0.899	0.33%
4	0.956	0.960	0.37%	0.910	0.907	-0.30%
5	0.927	0.957	3.31%	0.919	0.914	-0.62%
6	0.956	0.955	-0.10%	0.911	0.912	0.17%

These results all indicate that there is no significant change in propeller design or aerodynamic performance if the propeller is optimized in installed conditions compared to if it is optimized in isolated conditions. The almost insignificantly small but consistent increase in efficiency seen in tables 9.4 and 9.5 of the isolated and installed design operating at an angle of attack of 5 degrees can be contributed entirely to the beneficial upwash on the down-going blade. The differences in the design variables between the isolated and installed designs are so small that they could have been simply due to different starting points for the optimization, or noise in the models. It is possible that slight changes were made due to the inflow under an angle of attack, but if so, these were of no consequence to the performance. No consistent change can be seen in either one of the efficiency components, pointing to the fact that the optimizer is fluctuating around an optimum balance of both efficiency types with only very minor differences when comparing the isolated cases to the installed cases. It is known that in the case of an angle of attack, opposite loading changes occur throughout the rotation, which generally lead to a very small impact on the time-averaged performance. The results of this study demonstrate this as well.

Aeroacoustic Optimization

The objective during aeroacoustic optimization was to minimize the TSSP for a given maximum total energy expenditure, included by means of a penalty factor on the total energy expenditure of the aerodynamic optimum design. Figure 9.24 shows a side by side comparison of the progression of the noise improvements in terms of TSSP with increasing energy penalty factor for the propeller designs optimized in uniform flow and the propeller designs optimized in an inflow under a 5-degree angle of attack. Both the TSSP and total energy expenditure E in these graphs were normalized with respect to the TSSP and total energy expenditure of the three-bladed case at the aerodynamic optimum, for isolated and installed cases separately. As can be seen from the comparison, a slightly larger noise improvement could be realized for the installed designs, but a similar trend is visible. Tables 9.8 & 9.9 show a comparison between the absolute noise values that were found in the isolated designs operating in uniform flow and the isolated and installed designs operating in non-uniform flow. A consistent increase of around 20 decibel was found between the isolated designs operating in uniform flow and the propeller designs operating in non-uniform flow. As can be seen, the noise difference between the isolated design and the propeller designs operating under an angle of attack declines with increasing energy penalty, indicating that the additional noise caused by the installation effects is reduced. Similar to what was seen in the comparison between isolated and installed designs in terms of aerodynamic performance, the relative aeroacoustic performance improvement of the designs optimized in installed conditions compared to the isolated designs operating in the same installed conditions is extremely small, never exceeding 1 decibel.

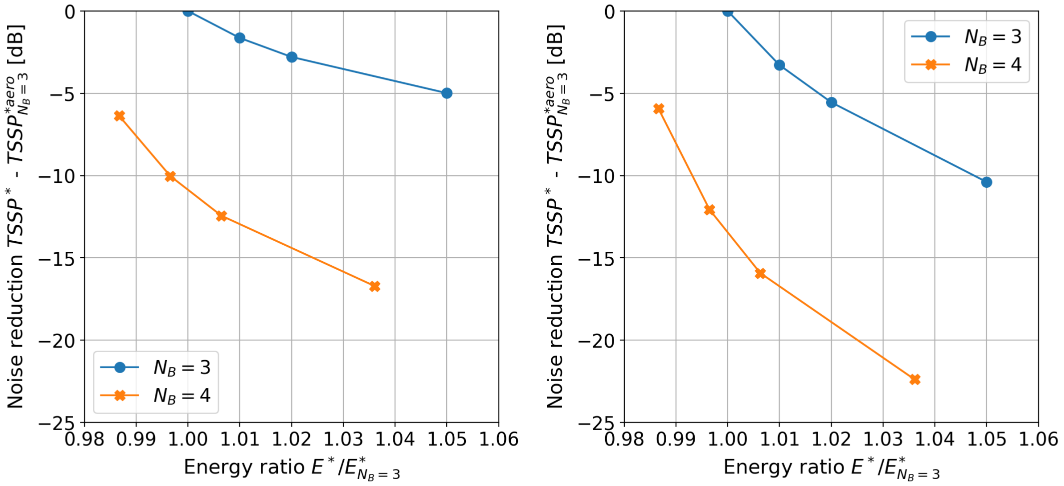

Fig. 9.24 Normalized TSSP versus energy expenditure for the isolated designs (left) and the installed designs (right).

Table 9.8 Comparison of the TSSP between the isolated and the installed designs at different penalty levels for a three-bladed propeller.

	iso. design	iso. design at AoA		inst. design at AoA		
Penalty	TSSP [dB]	TSSP [dB]	Diff w.r.t. iso design	TSSP [dB]	Diff w.r.t. iso design	Diff w.r.t. iso design at AoA
0%	-83.33	-59.49	23.84	-59.49	23.84	0.00
1%	-84.96	-62.69	22.27	-62.77	22.19	-0.08
2%	-86.12	-64.93	21.19	-65.04	21.08	-0.11
5%	-88.32	-69.21	19.11	-69.87	18.45	-0.66

Table 9.9 Comparison of the TSSP between the isolated and the installed designs at different penalty levels for a four-bladed propeller.

	iso. design	iso. design at AoA		inst. design at AoA		
Penalty	TSSP [dB]	TSSP [dB]	Diff w.r.t. iso design	TSSP [dB]	Diff w.r.t. iso design	Diff w.r.t. iso design at AoA
0%	-89.69	-65.43	24.26	-65.43	24.26	0.00
1%	-93.36	-71.25	22.11	-71.57	21.79	-0.32
2%	-95.76	-75.03	20.73	-75.42	20.34	-0.39
5%	-100.04	-81.70	18.34	-81.88	18.16	-0.18

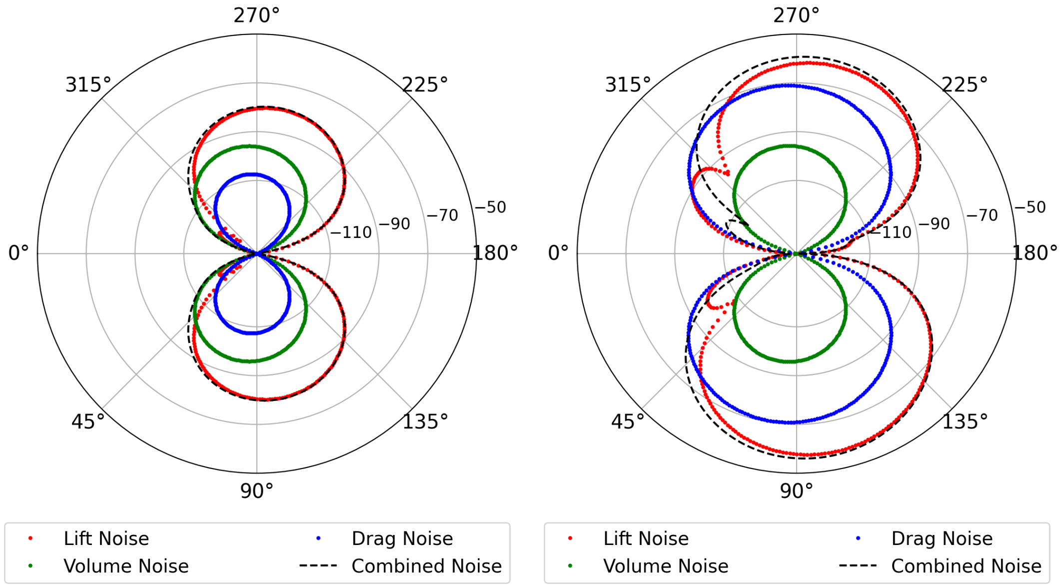

Fig. 9.25 Directivity plots with respect to observer angle θ for the three-bladed isolated design (left) and installed design (right) at the aerodynamic optimum.

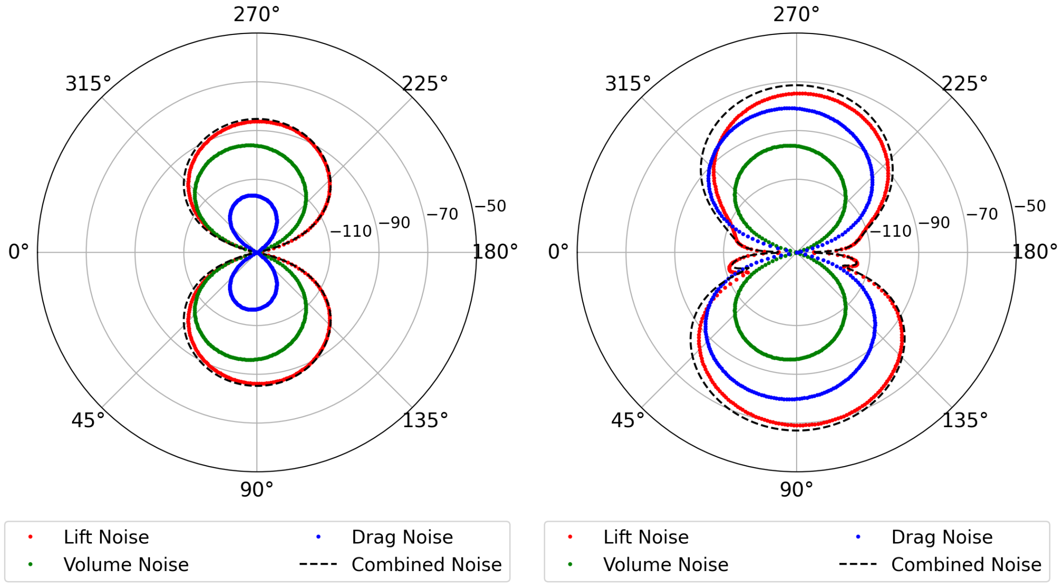

Fig. 9.26 Directivity plots with respect to observer angle θ for the three-bladed isolated design (left) and installed design (right) at a 5% energy penalty.

Figures 9.25 and 9.26 show the differences between the isolated and installed case in terms of the different noise components for the three-bladed case at the aerodynamic optimum and 5% penalty. As the figures show, the lift component remains dominant and increases significantly, but the drag component increases even more severely. The cause of this is the shape of the unsteady drag loading. Comparing the unsteady lift and drag loading curves (figure 9.27), it can be seen that while the lift curve is a nearly perfect sinusoid, the drag curve is more complex with steeper gradients, and larger amplitudes. While the absolute magnitude of the drag component is smaller, this shape causes a more severe relative noise increase compared to the lift component.

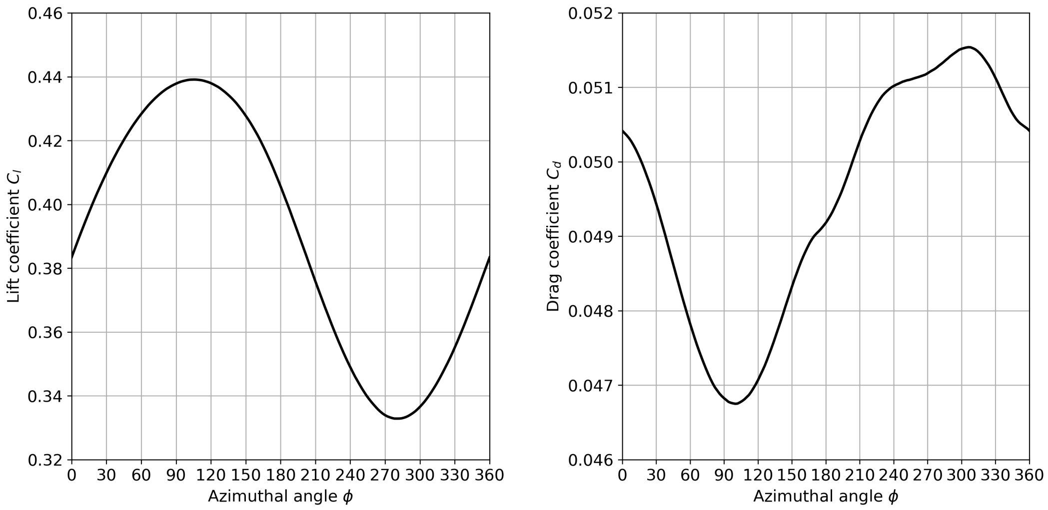

Fig. 9.27 Example of an unsteady lift- (left) and drag-coefficient curve (right) at the last radial station before the tip of an optimized four-bladed propeller at a 1% penalty level.

Figure 9.28 shows a comparison of the increase in advance ratio and the reduction in tip Mach number for the isolated and installed case. The increase in advance ratio is nearly identical to the isolated case (except for cruise at 5% penalty) for the three-bladed as well as the four-bladed case, and a similar trend is visible for the tip Mach number. These results reveal that the noise reduction strategy remains unchanged between the isolated and installed case. A reduction in tip Mach number is found to be the most effective strategy to reduce noise, and the advance ratio is increased to achieve this reduction. The increase in tip Mach number conveniently also decreases the noise cause by unsteady loading, since the unsteady loading amplitudes are largest near the tip. When the tip Mach number decreases, tip speeds and the local dynamic pressure at the tip decrease as well, leading to smaller tip loads and lower unsteady loading amplitudes.

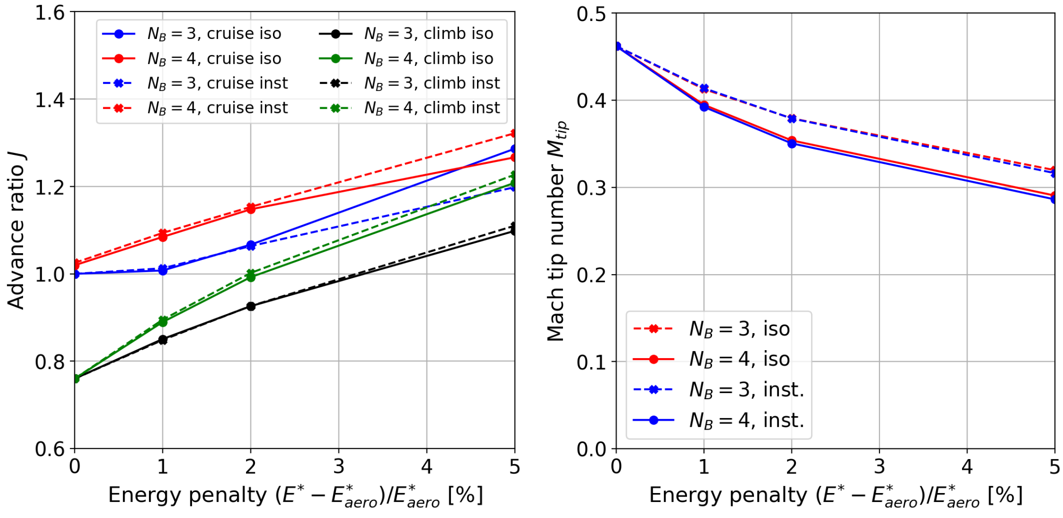

Fig. 9.28 Comparison of isolated and installed tip Mach number (left) and climb & cruise advance ratio's (right) at different penalty levels.

With the increase in advance ratio and the subsequent decrease in dynamic pressure, the product $C_l \cdot c$ has to increase to meet the loading requirement. Similar to the isolated case, a steep increase in chord length and subsequently solidity is observed (see figure 9.29). As the advance ratio increase, the inflow angle ϕ increases as well, requiring a larger lift loading to meet the the thrust requirement, resulting in increased induced losses and lower operating efficiencies (a more detailed explanation of this mechanism is described with the presentation of the results for the designs optimized in uniform flow presented earlier in this section). Figure 9.29 (right) shows the comparison in total efficiency and figure 9.30 the efficiency components.

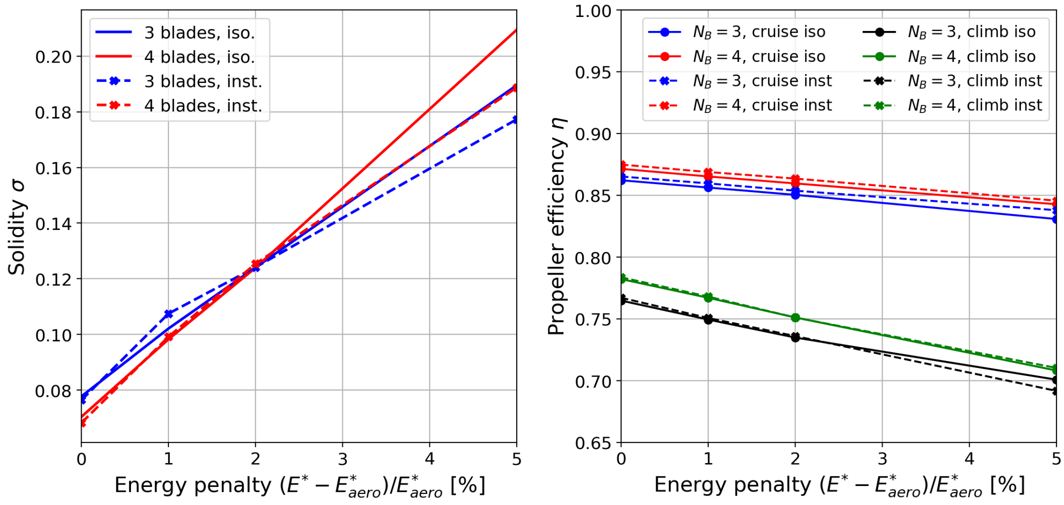

Fig. 9.29 Comparison of isolated and installed solidity (left) and propeller efficiency (right) at different penalty levels.

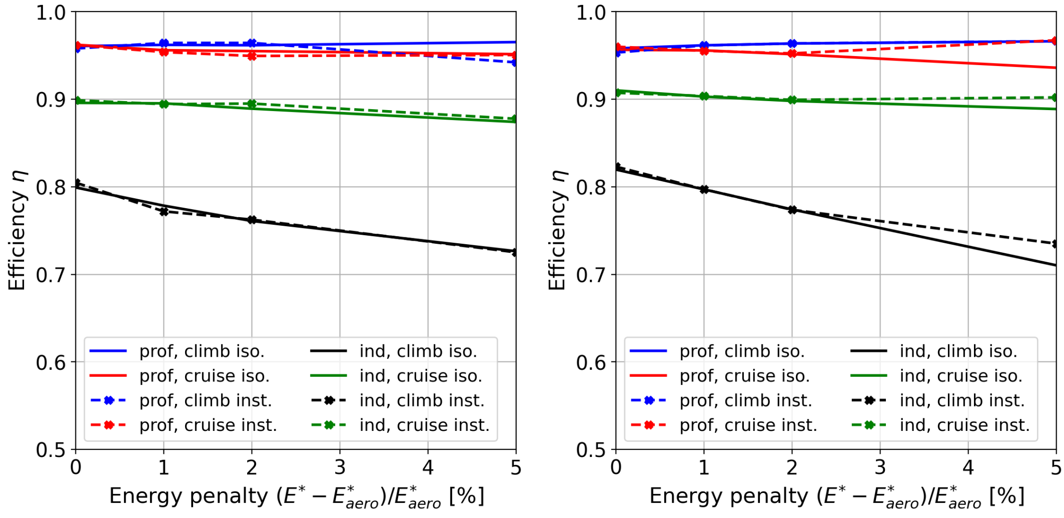

Fig. 9.30 Comparison of isolated and installed efficiency components for a three-bladed (left) and four-bladed (right) propeller at different penalty levels.

Although the noise reduction strategy of the designs optimized in uniform flow is identical to those designs optimized in non-uniform flow, the loading situation is slightly different due to the angular inflow. This explains the deviation in the design parameters which becomes apparent at the 5% penalty, in particular for the cruise parameters. At this penalty level, the installed design shows a smaller increase in solidity, accompanied by a larger increase in climb advance ratio and climb pitch (figures 9.28, 9.29, 9.31). The angular inflow changes the blade loading situation, which can be capitalized on in order to reduce the tip Mach number even further. This requires a larger increase in advance ratio, and a balancing act of the solidity and pitch angle to meet the loading requirement while maintaining a near-optimum lift distribution.

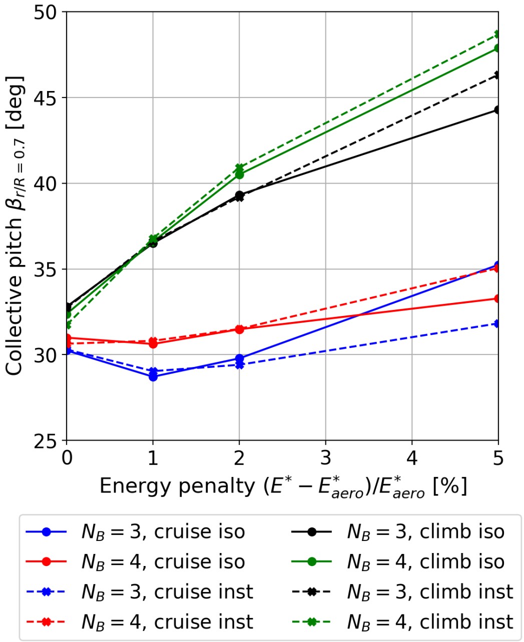

Fig. 9.31 Comparison of the collective pitch $\beta_{r/R=0.7}$ in climb and cruise for a three-bladed and four-bladed propeller at different penalty levels.

For cruise on the other hand, a smaller increase in pitch can be seen for the installed three-bladed case, and a larger increase for the installed four-bladed case. A similar pattern is seen for the advance ratios. It shows that blade count makes a significant difference in being able to meet the thrust requirement. For the three-bladed case, chord lengths are higher and advance ratios are lower to generate the required loading, similar to the isolated condition. The angular inflow changes the lift distribution, such that a different pitch is necessary to get close to the optimum lift-to-drag ratio, which determines the profile efficiency. At four blades, the combination of the smaller chord and angular inflow is such that the pitch and advance ratio can be higher to meet the loading requirement and achieve favorable efficiency. As figure 9.30 shows, there is little to no difference in the progression of the efficiency components, supporting the idea that the same overall strategy is taken to reduce noise and maximize efficiency for the designs optimized in the angular inflow compared to those optimized in uniform flow, but that some design variables required a different balance to deal with the angular inflow.

As shown earlier, the solidity increases with increasing energy penalty in a very similar way for the installed designs compared to the isolated designs. Figures 9.32 and 9.33 show a comparison between the untwisted blade planforms of the optimized three- and four-bladed propeller designs in isolated and installed conditions. As can be seen, the overall trend is the same, showing an increase in chord length with increasing energy penalty. The only difference that is worth observing is that for the 5% energy penalty, the blade planforms of the designs optimized in installed conditions have a larger tip chord compared to the designs optimized in isolated conditions, which tend to taper off more towards the tip. However, given that the other designs optimized with a 1% or 2% energy penalty do not show this difference when comparing the designs optimized in either isolated or installed conditions, and given that there was no significant impact on the performance as a result of this difference, it seems to have been inconsequential to the results as presented here.

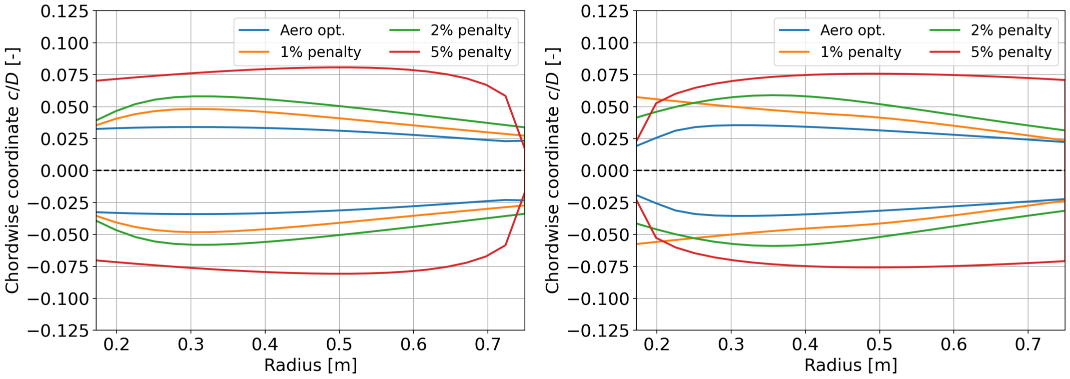

Fig. 9.32 Comparison of the untwisted planforms of the three-bladed propeller designs optimized in uniform flow (left) or non-uniform flow (right) at different penalty levels.

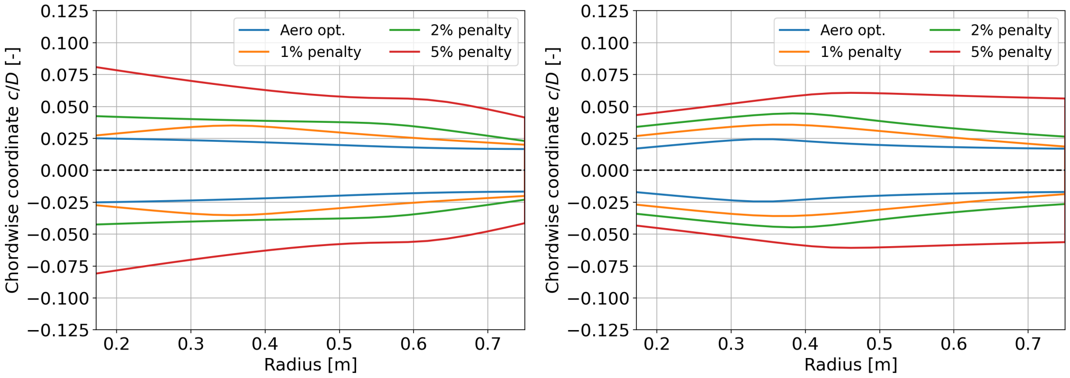

Fig. 9.33 Comparison of the untwisted planforms of the four-bladed propeller designs optimized in uniform flow (left) or non-uniform flow (right) at different penalty levels.

Finally, figures 9.34 and 9.35 show the directivity plots for the installed three- and four-bladed propellers of the aerodynamic optimum design and the design optimized at an energy penalty of 5%, this time varied with observer angle ϕ. It should be noted that the angle of 180° corresponds to the location straight underneath the propeller axis. As the figures show, no significant change in noise level occurs with varying angle ϕ. As such it can be concluded that for this specific type of non-uniform inflow, the observer angle ϕ is of little interest.

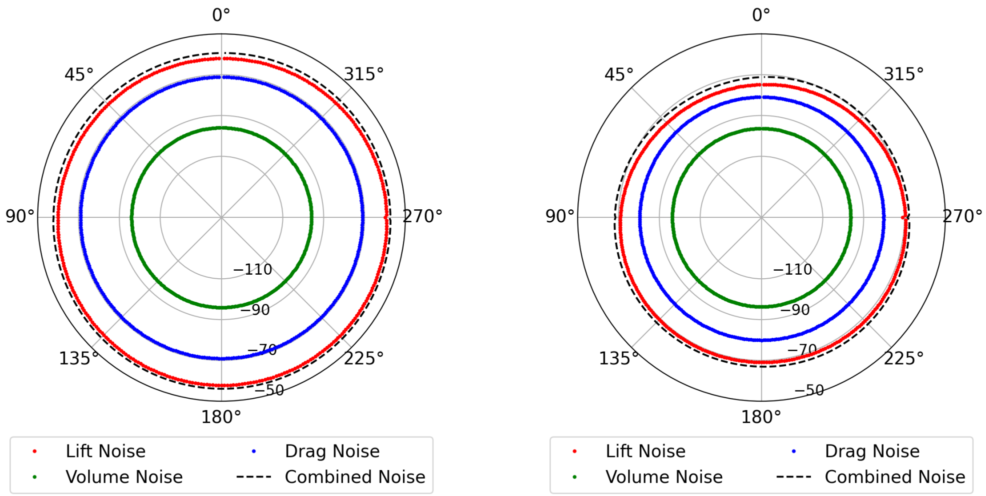

Fig. 9.34 TSSP directivity plot with respect to observer angle ϕ for the three-bladed aerodynamic optimum propeller design (left) and the propeller design optimized at a 5% energy penalty (right)

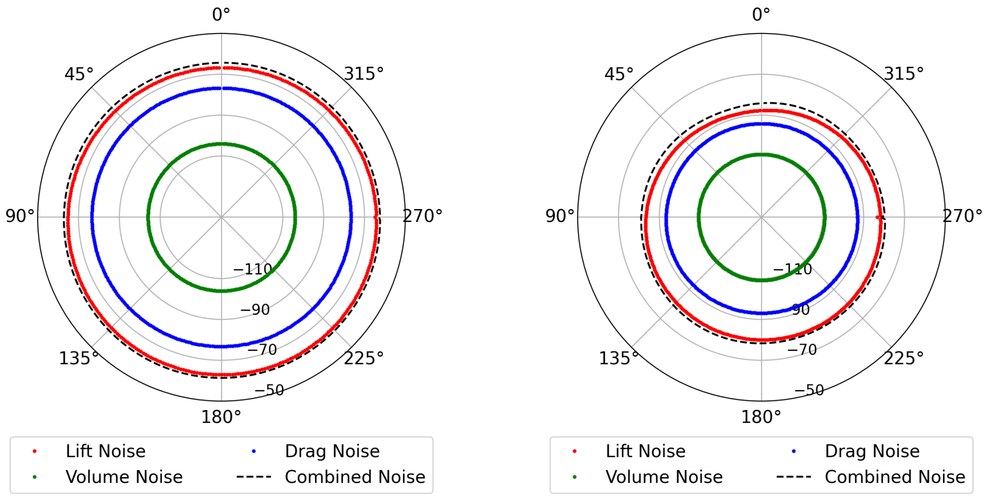

Fig. 9.35 TSSP directivity plot with respect to observer angle ϕ for the four-bladed aerodynamic optimum propeller design (left) and the propeller design optimized at a 5% energy penalty (right)

9.2.3 Limitations

Throughout this work, a number of possible limitations have been discussed already. In this subsection, two limitations that possibly influenced this work are discussed in more detail. The first limitation concerns the database of airfoil polars used for this study. The second limitation concerns blade sweep.

Reynolds Number Limitation

In the results above, a number of graphs have been presented that show the development of the Reynolds number for different design cases. The Reynolds number typically impacts the lift and drag performance of a given airfoil profile. For this study, an airfoil database was used that contained polar data for the TUD-XPROP airfoils at a range of Reynolds numbers from 100,000 to 700,000. However, as can be seen for example in figure **??**, the actual Reynolds number sometimes exceeded 700,000, in particular for the three-bladed case, which featured the highest chord lengths. When this happens, the optimizer automatically defaulted to pick the polar corresponding to the highest Reynolds number available, namely 700,000. Usually, an increased Reynolds number increases the potential lift-to-drag coefficient that could be reached. As a result, the reference maximum lift-to-drag coefficient selected for these profiles could have been lower than it should have been due to the limited polar data. This in turn could have had an impact on the profile efficiency, returning a lower profile efficiency than in actuality, because the optimum lift-to-drag coefficient is lower than in actuality. Because of this, the optimizer might have made different choices than it otherwise would have. To make a better estimation of the impact of this limitation on the results, a study was performed to see the change in maximum achievable lift-to-drag coefficient for increasing Reynolds number. The result are shown in the figure below.

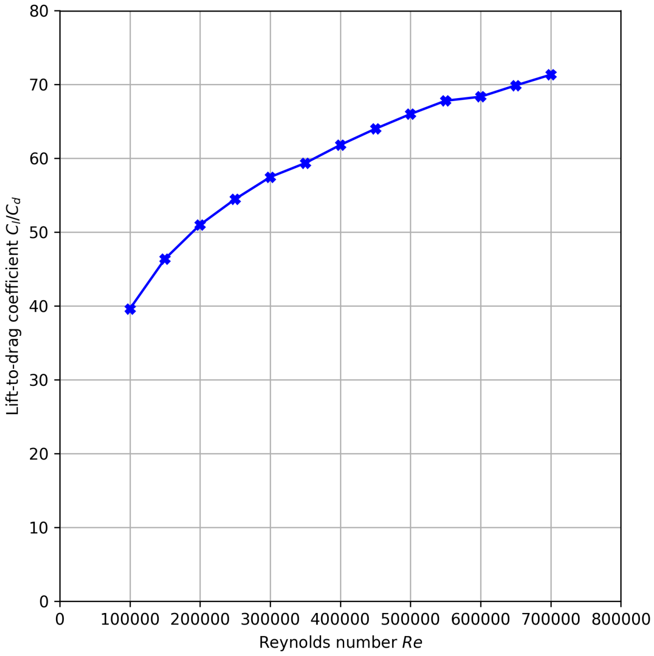

Fig. 9.36 Maximum achievable lift-to-drag coefficient for the Reynolds numbers available in the airfoil polar database (5th radial station / $r/R = 0.3$).

As figure 9.36 shows, the increase of the maximum achievable lift-to-drag ratio is flattening slightly with increasing Reynolds number, but has likely not reached its peak at the cutoff Reynolds number of 700,000. This means that there could definitely have been an effect on the results. However, figures 9.37 and 9.38 show a comparison of the Reynolds number found in the isolated and installed cases. As can be seen, for both cases the penalty levels at which the Reynolds number exceeded the 700,000 mark is similar, meaning that this limitation did not significantly unfavorably impact one over the other. Nevertheless, most of the results of the three-bladed case, and the 5% penalty design for the four-bladed case should be viewed in the light of the limitation, that it was likely easier to keep a high profile efficiency than should have been the case, which could have unjustly skewed the results towards appearing more efficient, and skewed the design variables to focus more on other performance metrics such as induced efficiency than it otherwise would have done. Despite this limitation, it is unlikely that it the impact on the results would have been significant enough to change the interpretation of the results and the conclusion.

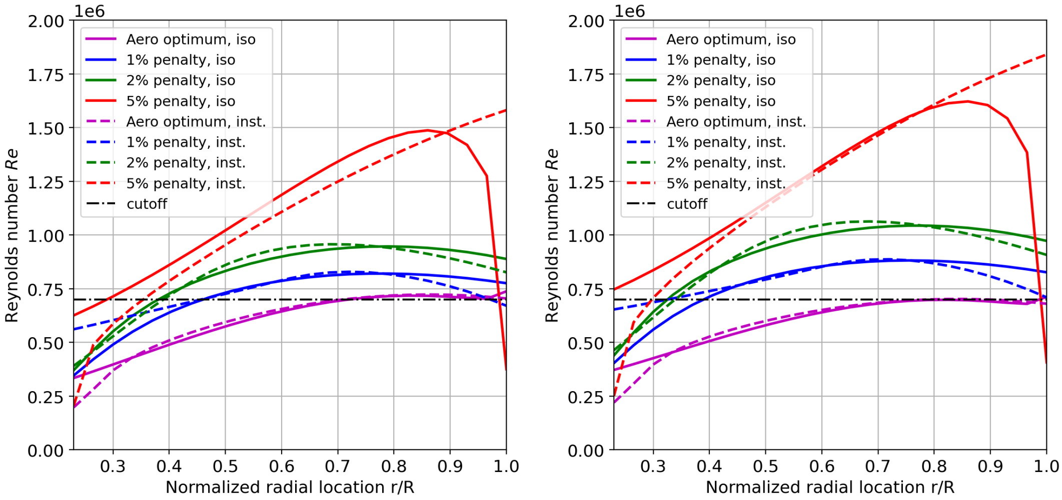

Fig. 9.37 Comparison of Reynolds number distribution between the three-bladed isolated and installed propeller designs in climb (left) and cruise (right) for varying penalty levels with respect to the cutoff Reynolds number.

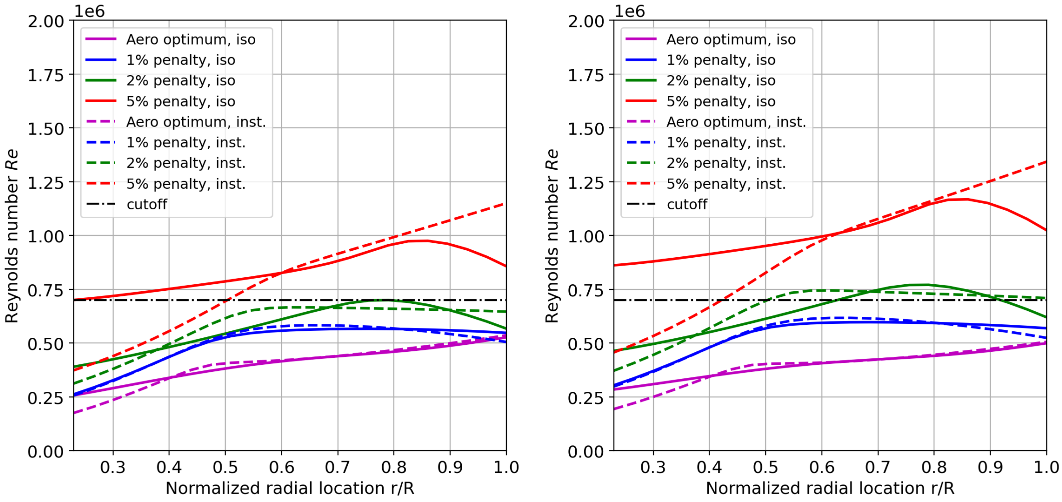

Fig. 9.38 Comparison of Reynolds number distribution between the four-bladed isolated and installed propeller designs in climb (left) and cruise (right) for varying penalty levels with respect to the cutoff Reynolds number.

Sweep Limitation

As discussed earlier in this work, blade sweep was not included as a design variable. The models used, such as the BEM-model, have the possibility to deal with blade sweep, but the elements that deal with sweep specifically were not used. Nevertheless, most blade designs have a certain degree of sweep, measured as the angle between the quarter chord line and the x-axis in figure 9.39, simply due to the change in chord length. As can be deduced from the figure, the red planform likely has the largest sweep out of the blade planforms shown in the figure. This blade sweep could have had an effect on the aerodynamic and aeroacoustic performance if taken into account. However, since the displacements between the different blade sections are very small compared to the wavelength of the dominant acoustic emissions at 1 BPF, the former being in the order of a few centimeters maximum while the latter being in the order of around 2 to 3 meters ($\lambda = c/(N_b * n)$), it is unlikely there would have been any significant phase cancellation due to the sweep which could have resulted in a different aeroacoustic performance. Moreover, the realized blade sweeps were very marginal in this work (the middle of the blade always remained unswept), and if the sweep angle resulting from a tapering effect would have had an impact on aeroacoustic performance, it could have been employed equally in installed and isolated condition by the optimizer. It can therefore be concluded that it is likely that neglecting this effect did not have a significant effect on the interpretation of the results, or the conclusion

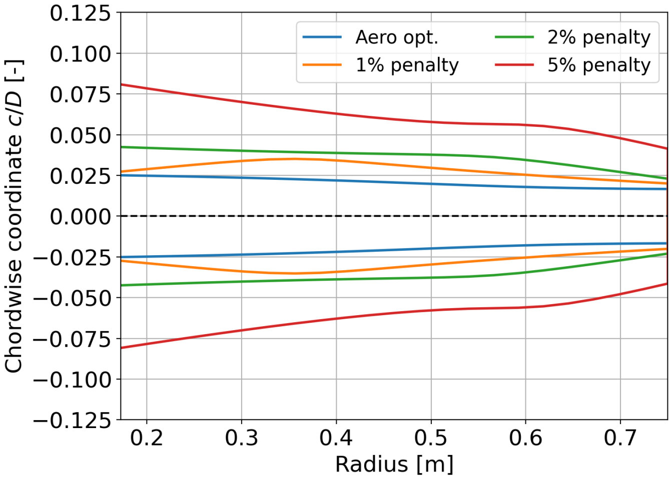

Fig. 9.39 Untwisted planforms of the four-bladed propeller designs optimized for noise improvements in uniform flow.

Part IV

Conclusions & Recommendations

Chapter 10

Conclusions

In this chapter, the research questions set at the beginning of this project will be answered, thereby summarizing and concluding the presented work. The objective of this project was to perform a design optimization study of a propeller exposed to a non-uniform flow, optimizing for efficiency and noise improvements, and making observations on the differences between designs that were optimized when including installation effects, and designs that were optimized in uniform flow. This objective was achieved, and the research questions can be answered as follows.

1. *Based on literature, which aerodynamic and aeroacoustic performance models are capable of accurately modeling isolated and installer propeller performance, and are suitable for implementation in an optimization framework?*

   Since this study involved a lot of optimization work, models were required that required low computational effort, while remaining accurate enough to correctly model trends that are useful in the preliminary design stage. Furthermore, for this work in particular, models were required that could be used to work with an isolated propeller and a propeller exposed to a non-uniform flow. For the aerodynamic models, the BEM model was found to be the fastest model that could still include the blade design variables of interest in the model. During verification and validation, it was found that the BEM model could accurately predict trends, specifically for the advance ratios relevant for this work, but that the propeller efficiency was likely to be over-predicted. This loss in accuracy was deemed acceptable for this work. When operating in a non-uniform flow, the BEM-model does not suffice to model aerodynamic performance. For this part, an aerodynamic performance model for non-uniform inflow by van Arnhem was used[5]. This model was chosen for its ease of implementation and low computational effort. The model had been validated by comparison to CFD data, which showed a 24% under-prediction of the root-mean square blade thrust, but a very close comparison of the integral thrust and torque values. Despite the error, trends were measured accurately, which was the main requirement for this work. For the aeroacoustic model, Hanson's Helicoidal Surface Theory (HST) model was chosen. This method was preferred over time-domain methods for its significantly lower computational cost. Furthermore, this model was available in an adapted version that allowed the modelling of noise due to installation effects. The isolated model was validated in work published by Kotwicz et al.[20], who noted that the model had a significant average error, but that it was suitable for including in optimization framework for preliminary design studies. The adapted version for installed noise could not be validated, but the results seemed reasonable based on the general knowledge of aeroacoustic behavior in the non-uniform flow studied. All models chosen are similar in the sense that they are computationally cheap, but suffer in terms of accuracy. Nevertheless, it was shown for all models that they were able to predict trends correctly. Given this knowledge, these models were found suitable for implementation in an optimization framework aimed at performing preliminary design studies, as carried out in this thesis.

2. *Which optimization method is suitable for this type of problem?*

   A gradient-based optimization method was chosen for this work. Gradient-based methods are known to be robust and converge fast. When selecting the design variables for this study, design variables with discrete values were deliberately avoided to make the use of this optimization method more feasible. A risk of using gradient-based methods is that it could converge to local optima instead of the global optimum. To maximize the chance of finding the global optimum, multiple optimization runs (typically 3 to 5) were performed with different randomized starting points. The fast convergence of this optimization method allowed this to be done in the given span of time. By using this optimization method, designs could be optimized for several blade counts, and for both aerodynamic and aeroacoustic performance within a relatively short time-span. Great confidence was found in the results as the optimized designs found by starting from a different randomized starting point typically had their objective value in very close proximity to each other. As such it could be concluded that this optimization method was very suitable for the type of design optimization performed in this thesis.

3. *How to implement the trade-off between aerodynamic and aeroacoustic performance in the optimization framework that allows for clear quantification of the effects on propeller design for both types of performance?*

   When optimizing for multiple objectives, it is often difficult to interpret the results and make a distinction on which changes in the design variables were made to benefit one objective or the other. As such, it becomes hard to draw conclusions on design strategies which benefit a certain specific objective. In this work, the optimization objectives were twofold, namely aerodynamic efficiency, and improved aeroacoustic performance (noise reduction). To be able to make a more clear distinction between the two objectives, it was decided to split them, rather than lump them together in a single mixed objective. First, the propeller was optimized for aerodynamic efficiency only. In the context of this work this was done by setting an objective to minimize the total energy expenditure for a given mission consisting of a climb and a cruise phase. The resulting design served as the aerodynamic optimum starting point for the aeroacoustic optimization. For the aeroacoustic optimization, the sole objective was to minimize the noise production with respect to the aerodynamic optimum. To ensure a reasonably aerodynamically efficient design, a constraint was put on the total energy expenditure of the design during the same mission. This total energy expenditure was allowed to deviate from the energy expenditure of the aerodynamic optimum with a certain percentage factor, named penalty factors in this work. These penalty factors were chosen to be 1%, 2%, and 5%. In this manner, propeller designs were generated that were optimized for both aerodynamic efficiency and aeroacoustic performance. However, with much more control over the emphasis that was put on either objective by the optimizer, compared to if a mixed objective was used. Furthermore, operating in this manner allowed for a clear distinction between the changes in design variables made for either objective, such that the results could be interpreted in a more meaningful way.

4. *What is the influence of installation effects on the propeller performance and optimized design?*

   Given that the optimization objectives of aerodynamic efficiency and aeroacoustic performance were split, the influence of installation effects on the optimized designs could be studied separately for both objectives. In this work, the only type of installation effect that was studied is a propeller subjected to an inflow under a 5° angle of attack. For the first objective, aerodynamic efficiency, a three-, four-, five-, and six-bladed propeller design was optimized, both in isolated and installed conditions. A comparison was made between the aerodynamic efficiency of the isolated design operating in uniform flow (1), the isolated design operating in the non-uniform flow (2), and the installed design operating in the non-uniform flow (3). With respect to the isolated design operating in uniform flow, the installed design saw an efficiency increase of 0.19 - 0.49%. This very small increase is owing to the beneficial upwash experienced by the downgoing blade and the inflow under an angle of attack of 5 degrees caused a very small but insignificant change in the design variables as a result of different angles of attack experienced by the blade. If the installed design is compared to the isolated design performing in the same non-uniform flow, the efficiency improvement reduces to an almost negligible -0.02 - 0.14%. When comparing the change in design variables as well as the change in the underlying efficiency components (profile and induced efficiency), no different optimization strategy is observed between the installed propellers and the isolated propellers. This strategy can be summarized as an attempt to increase the efficiency for higher blade counts (starting with a blade count of three) by reducing the induced losses, which is possible partially due to the lower blade loading with increased blade counts. The other design variables adjust such that the thrust requirement can still be met, and the profile drag is kept constant. Based on the results, the conclusion can be drawn that for an inflow under an angle of attack of 5 degrees and this mission profile, including installation effects in the optimization process makes no meaningful difference on the optimized design.

   Next, the designs optimized for aeroacoustic performance were compared. For the aeroacoustic optimizations, only a three- and four-bladed propeller design were optimized. The results showed a 18 - 24 dB increase in TSSP for the installed designs compared to the isolated designs, but only a 0.08 - 0.66 dB relative performance increase when comparing the installed design to the isolated design operating in the same flow. Both the isolated and the installed designs showed very similar trends in terms of noise improvements with increasing energy penalty, but the designs performing in non-uniform flow saw a sharper decrease in TSSP. Directivity plots revealed that the noise increase in the installed case was caused by an increase in lift and drag noise, resulting from the unsteady loading as a result of the non-uniform inflow. The noise reduction strategy showed very little difference between the isolated and installed designs. Reducing the tip Mach number was the most effective method available to reduce noise levels. This was done by increasing the advance ratio, reducing the tip speeds and subsequently the dynamic pressure experienced by the blade. Blade loading had to increase in order to make up for the loss in dynamic pressure, resulting in higher induced losses. The introduction of a non-uniform flow did not change the main strategy for noise reduction and efficiency conservation. However, a slightly different balance of design variables had to be found to adequately deal with the non-uniform inflow to arrive at very similar outcomes as the isolated design. Given these results it can be concluded that even though the non-uniform flow does have a significant influence on the aeroacoustic performance, it changes very little in terms of optimization strategy, and the designs optimized in the installed condition are extremely similar to those optimized in uniform flow. Although small differences were observed in the designs optimized in installed conditions compared to the designs optimized in isolated conditions, in particular a lower solidity for the propellers optimized installed conditions and different pitch values, the aim of these changes appeared to be exactly the same, namely the reduction of noise through a reduction in the tip Mach number.

In conclusion, the work has shown that for the non-uniform flow used in this work (inflow under a 5-degree angle of attack) and using the design variables chord length distribution, twist distribution, advance ratio, and collective pitch angle (the latter two having separate values for the climb & cruise phases), there is no benefit in including the non-uniform flow and its effects in the optimization process. The optimized designs that result from the optimization routine that included installation effects do not perform significantly better (both aerodynamically and aeroacoustically) compared to the optimized designs that result from an optimization routine that only considered uniform flow, when both of these types of designs optimized under different conditions are operating in the same non-uniform flow. This does not mean however there is no benefit in including the non-uniform flow in the optimization process when other types of non-uniform flow are considered (e.g. a wake encounter), or when other design variables are included (e.g. blade sweep), which is something that can be researched in future work. Another important conclusion that can be drawn from this work is that the optimization set-up used in this work, including all the implemented aerodynamic and aeroacoustic models, is suitable for the type of design optimization studies that were presented, and can therefore be used in future work to continue the research in the field of propeller design optimization for non-uniform inflow.

Chapter 11

Recommendations

Based on the results presented in this thesis and experience gained by building the model and performing the optimizations, a number of recommendations can be made for future authors.

- The airfoil data available for this work formed a limitation and obstacle for two reasons. Firstly, polars were not available for Reynolds numbers above 700,000, while many of the optimized designs operated at Reynolds numbers far above this. As a result, they used the polar with the highest Reynolds number available, thereby affecting the results. Secondly, some of the polars were sparsely filled, especially at low Reynolds numbers, and the missing lift and drag coefficient data were determined by means of inter- or extrapolation, which sometimes resulted in odd and unrealistic results. It is therefore recommended to either create a far more extensive and robust polar database for the airfoils used, or implement an airfoil performance analysis tool in the optimization framework. With the latter choice it should be noted that the implementation of such a tool could lead to a significant increase in computational effort for each optimization run, and should therefore carefully be considered on its merits in the light of that specific project.
- The installed noise model used in this study is (as far as the author knows) as of yet not validated comprehensively by means of comparison with experiment or CFD. Therefore, the results generated by this model should be regarded with a great deal of caution. If more studies want to use this model, and want to draw meaningful conclusions from the generated results, it is recommended that this model is validated for several different types of non-uniform flow.
- In the present study, only the effects of a flow under an angle of attack were studied. However, there are a number of other common types of non-uniform flow with distinct characteristics. In a real-world situation, the propeller is likely to operate under a combination of these different types of non-uniform flow. A wake encounter would be an interesting flow to study, since the disturbance is very acute and short. As a result, it hardly impacts efficiency, but can lead to significant noise increases. The typical method of reducing noise by means of reducing the tip Mach number, as seen in this study, intuitively does not seem to be the best method of reducing noise for this type of disturbance, since it does not specifically address the unsteady loading amplitude that causes the noise increase when operating in this type of flow. Therefore, including installation effects in the optimization could potentially lead to a very different optimization strategy, and make an impact. Especially if including

the minimization of the unsteady loading that causes the noise increase is considered as an optimization objective. It is therefore recommended to investigate the impact of including installation effects in the design optimization for different types of non-uniform flow such as a wake encounter situation.

- This study did not make use of a structural model. Instead, the bounds of the design variables were chosen as such that a structurally feasible design was highly likely. Nevertheless, sometimes sharp increases or decreases in chord or twist angle were observed in some of the results generated by this model, which could be structurally impossible to realize. Furthermore, including a structural model could potentially allow one to use a larger design space, since the structural model now guarantees a certain structural feasibility, even if unexpected shapes are explored by the optimizer. It is therefore recommended to explore the possibility of adding a structural model if one is to expand the work presented in this thesis.
- A number of design variables of interest were not included in this study in the interest of time and to curb complexity. It would be interesting to include certain design parameters in future studies to explore their influence on the aerodynamically and aeroacoustically optimized designs. In particular:
  - Blade sweep, which has been shown to be able to reduce noise by means of a phase-cancellation effect in isolated propeller design. When operating in non-uniform flow, the acoustic cancellation effect might be even larger, as the blade sweep will lead to an additional phase lag in the unsteady loading components, which were not present in the isolated situation;
  - Airfoil shape, to be able to influence profile efficiency and thickness noise in a more profound way, and change the unsteady response;
  - Propeller diameter, which can modify the overall disk loading, and thereby blade loading and blade aspect ratio, all of which will effect the aerodynamic efficiency. This gives the optimizer an extra tool and potentially new strategies to keep efficiency as high as possible while attempting to reduce noise.
- The mission design used in this study consisted only of a climb and cruise phase. Noise was measured from the climb phase only, at an altitude of 100 meters, and the cruise phase took 5 times as long as the climb phase. The mission design has a significant influence on the results, since the ratio in time between the cruise and climb phase determines how costly an efficiency loss is in either mission segment for the total energy expenditure. While the noise at 100 meter altitude is relevant, it is hardly the only location at which noise would be relevant to measure. Most aircraft noise complaints are from those that live nearby airports, and it would thus be relevant to analyze the noise at height differences between a climbing or approaching aircraft and housing of those living near airports. Moreover, the type of propeller aircraft that are typically associated with noise pollution (e.g. regional turboprop aircraft) generally have a cruise phase that is longer than 5 times the climb phase, which could have a large impact on the results of the optimization. It is therefore recommend in the future to think critically about the mission design, such that a mission is studied that generates results that are meaningful for real world applications.

References

[1] L.L.M. Veldhuis. *Propeller Wing Aerodynamic Interference*. PhD thesis, Delft University of Technology, Department of Aerospace Engineering, 2005.

[2] Ger J.J. Ruijgrok. *Elements of Airplane Performance*. Delft Academic Press (VSSD), Delft, the Netherlands, 2009.

[3] B. Magliozzi and D.B. Hanson. Propeller and Propfan Noise. *NASA, Langley Research Center, Aeroacoustics of Flight Vehicles: Theory and Practice, 1:1-64*, 1991.

[4] B.G. Marinus. *Multdisciplinary Optimization of Aircraft Propeller Blades*. PhD thesis, Centrale Lyon - Unviersity Lyon I, Doctoral School of Mechanics, Energetics, Civil Engineering and Acoustics, 2005.

[5] Nando van Arnhem, Reynard de Vries, Tomas Sinnige, Roelof Vos, Georg Eitelberg, and Leo L. M. Veldhuis. Engineering Method to Estimate the Blade Loading of Propellers in Nonuniform Flow. *AIAA Journal Vol. 58, No. 12*, 2020.

[6] T. Sinnige. *Aerodynamic and Aeroacoustic Interaction Effects for Tip-Mounted Propellers*. PhD thesis, Delft University of Technology, Department of Aerospace Engineering, 2018.

[7] L.L.M. Veldhuis, E. van Berkel, M. Kotsonis, and G. Eitelberg. Non-Uniform Inflow Effects on Propeller Performance. *AIAA Paper 2013-2801*, 2013.

[8] T. Sinnige, N. van Arnhem, T.C.A. Stokkermans, G. Eitelberg, and L.L.M. Veldhuis. Wingtip-Mounted Propellers: Aerodynamic Analysis of Interaction Effects and Comparison with Conventional Layout. *Journal of Aircraft, Vol. 56, No. 1, pp. 295-312*, 2019.

[9] Laurence J. Heidelberg and Richard P. Woodward. Advanced Turboprop Wing Installation Effects Measured by Unsteady Blade Pressure and Noise. *AIAA 11th Aeroacoustics Conference, AIAA-87-2719*, 1987.

[10] C.J. Miller and J.P. Sullivan. Noise Constraints Effecting Optimal Propeller Designs. *Technical Memorandum 105369, NASA Technical Memorandum, 86967*, 1985.

[11] D.B. Hanson. The influence of propeller design parameters on far field harmonic noise in forward flight. *5th Aeroacoustics Conference, American Institute of Aeronautics and Astronautics (AIAA)*, 1979.

[12] Antonio Pagano, Luigi Federico, Mattia Barbarino, Fabio Guida, and Marco Aversano. Multi-objective Aeroacoustic Optimization of an Aircraft Propeller. *12th AIAA/ISSMO Multidisciplinary Analysis and Optimization Conference*, 2008.

[13] Tianxing (George) Hu. Optimization for a Quiet Propeller. A report of a visiting researcher in the NL from 12.2018 to 11.2019, Delft University of Technology, Department of Aerospace Engineering, 2019.

[14] Donald B. Hanson. Noise of Counter-rotation Propellers. *AIAA Journal, Vol. 22, No. 7*, 1985.

[15] D.B. Hanson. Helicoidal Surface Theory for Harmonic Noise of Propellers in the Far Field. *AIAA Journal 18.10*, 1980.

[16] Xin Geng, Tianxiang Hu, Peiqing Liu, Tomas Sinnige, and Georg Eitelberg. Analysis of Thrust-Scaled Acoustic Emissions Of Aircraft Propeller and their Dependence on Propulsice Efficiency (Accepted/In press). *32nd Congress of the International Council of the Aeronautical Sciences [ICAS-2021-0751] (ICAS 2021). International Council of the Aeronautical Sciences.*, 2021.

[17] P. Dufour. Comparison of Two Aerodynamic Loading Calculation Methods for Propellers, and Application to the Prediction of Blade Noise. A Research Internship, Delft University of Technology, Department of Aerospace Engineering, 2020.

[18] Qingxi Li, Kenan Öztürk, Tomas Sinnige, Daniele Ragni, Georg Eitelberg, Leo Veldhuis, and Yangang Wang. Design and Experimental Validation of Swirl-Recovery Vanes for Propeller Propulsion Systems. *35th AIAA Applied Aerodynamics*, 2017.

[19] Jack E. Marte and Donald W. Kurtz. A Review of Aerodyanmic Noise From Propellers, Rotors, and Lift Fans. *NASA Technical Report 32-1462*, 1970.

[20] Mark T. Kotwicz Herniczek, Daniel Feszty, Sid-Ali Meslioui, Jong Park, and Fred Nitzsche. Evaluation of Acoustic Frequency Methods for the Prediction of Propeller Noise. *AIAA Journal, Vol. 57, No. 6*, 2019.

[21] H. Swift. A Review of the Literature Related to Potential Health Effects of Aircraft Noise. *Partnership for AiR Transportation*, 2010.

[22] T. Sinnige. Aircraft Aerodynamics primer course: Propeller Interactional Aerodynamics. Lecture Notes, Delft University of Technology, Department of Aerospace Engineering, 2020.

[23] Werner M. Dobrzynski, Hanno H. Heller, John O. Powers, and James E. Densmore. DFVLR/FAA Propeller Noise Tests in the German-Dutch Wind Tunnel DNW. *DFVLR-IB 129-86/3, FAA-AEE 86-3*, 1986.

[24] Stewart A. L. Glegg and William J. Devenport. *Aeroacoustics of Low Mach Number Flows: Fundamentals, Analysis, and Measurement*. Academic Press, London, United Kingdom, 2017.

[25] R.E. Kuhn and J.W. Draper. Investigation of the Aerodynamic Characteristics of a Model Wing-Propeller Combination and of the Wing and Propeller Separately at Angles of Attack up to 90. *NACA Rep. 1263*, 1956.

[26] D.P. Bencze, R.C. Smith, H.R. Welge, and J.P. Crowder. Propeller Slipstream Wing Interactions at Mach No. 0.8. *SAE 780997*, 1978.

[27] Arne W. Stuermer. Unsteady CFD Simulations of Propeller Installation Effects. *42nd AIAA/ASME/SAE/ASEE Joint Propulsion Conference & Exhibit*, 2006.

[28] Wouter de Haan. *Impact of Blade Sweep on Aerodynamic and Aeroacoustic Performance Optimization of Isolated Propellers*, MSc Thesis, Delft University of Technology, Department of Aerospace Engineering. 2021.

[29] Stijn Burger. *Multi-Fidelity Aerodynamic and Aeroacoustic Sensitivity Study of Isolated Propellers*, MSc Thesis, Delft University of Technology, Department of Aerospace Engineering. 2020.

[30] Emmanuel Bralard, Kristian Dixon, and Mac Gaunaa. An improved tip-loss correction based on vortex code results. *European Wind Energy Conference and Exhibition 2012, EWEC 2012, volume 2, pages 1079–1087*, 2012.

[31] O. Gur and A. Rosen. Comparison Between Blade-Element Models of Propellers. *48th Israel Annual Conference on Aerospace Sciences*, 2008.

[32] Xinqiang Liu and Weiliang He. Performance Calculation and Design of Stratospheric Propeller. *IEEE Access 5, pp. 14358-14368*, 2017.

[33] Snorri Gudmundsson. *General Aviation Aircraft Design*. Butterworth-Heinemann, The Boulevard, Langford Lane, Kidlington, Oxford OX5 1GB, UK, 2014.

[34] Roger Willemsen. *A Sensitivity Study on the Aerodynamic Performance of a Wingtip-Mounted Tractor Propeller-Wing System*, MSc Thesis, Delft University of Technology, Department of Aerospace Engineering. 2020.

[35] C.N. Adkins and R.H. Liebeck. Design of Optimum Propellers. *Journal of Propulsion and Power 10.5, pp. 676-682*, 1994.

[36] M.K. Rwigema. Propeller Blade Element Momentum Theory with Vortex Wake Deflection. *27th international congress of the aeronautical sciences (ICAS 2010)*, 2010.

[37] Mark Drela, MIT Aero & Astro. QPROP Formulation, 2006. [Accessed: 31-03-2022] https://web.mit.edu/drela/Public/web/qprop/qprop_theory.pdf.

[38] W.R. Sears. Some Aspects of Non-Stationary Airfoil Theory and Its Practical Application. *Journal of the Aeronautical Sciences, Vol. 8, No. 3, pp. 104-108*, 1941.

[39] R.K. Amiet. Compressibility Effects in Unsteady Thin-Airfoil Theory. *AIAA Journal, Vol. 12, No. 2, pp. 252-255*, 1974.

[40] F. Farassat. Theory of Noise Generation from Moving Bodies with an Application to Helicopter Rotors. *NASA Technical report*, 1975.

[41] F. Farassat. Open Rotor Noise Prediction Methods at NASA Langley - A Technology Review. *15th AIAA/CEAS Aeroacoustic Conference (30th AIAA Aeroacoustic Conference) pp.11-13*, 2009.

[42] F. Farassat. Derivation of Formulations 1 and 1A of Farassat. *NASA, NASA/TM-20(March):1-25*, 2007.

[43] D.B. Hanson. Near Field Noise of High Tip Speed Propellers in Forward Flight. *AIAA Paper No. 76-565*, 1976.

[44] L. Gutin. On the Sound Field of a Rotating Propeller. *NACA TM 1195*, 1948.

[45] The MathWorks, Inc. FMINCON Documentation, 2006. [Accessed: 31-03-2022] https://www.mathworks.com/help/optim/ug/fmincon.html.

[46] Jorge Nocedal and Stephen J. Wright. *Numerical Optimization*. Springer Science+Business Media, LLC, 223 Spring Street, New York, NY 10013, USA, 2006.

[47] InHolland Delft - Aeronautical and Precision Engineering. *The Dragonfly Project*, 2019. https://projectdragonfly.nl/ [Accessed: 21-03-2022].

Appendix A

Optimization Workflow Diagram

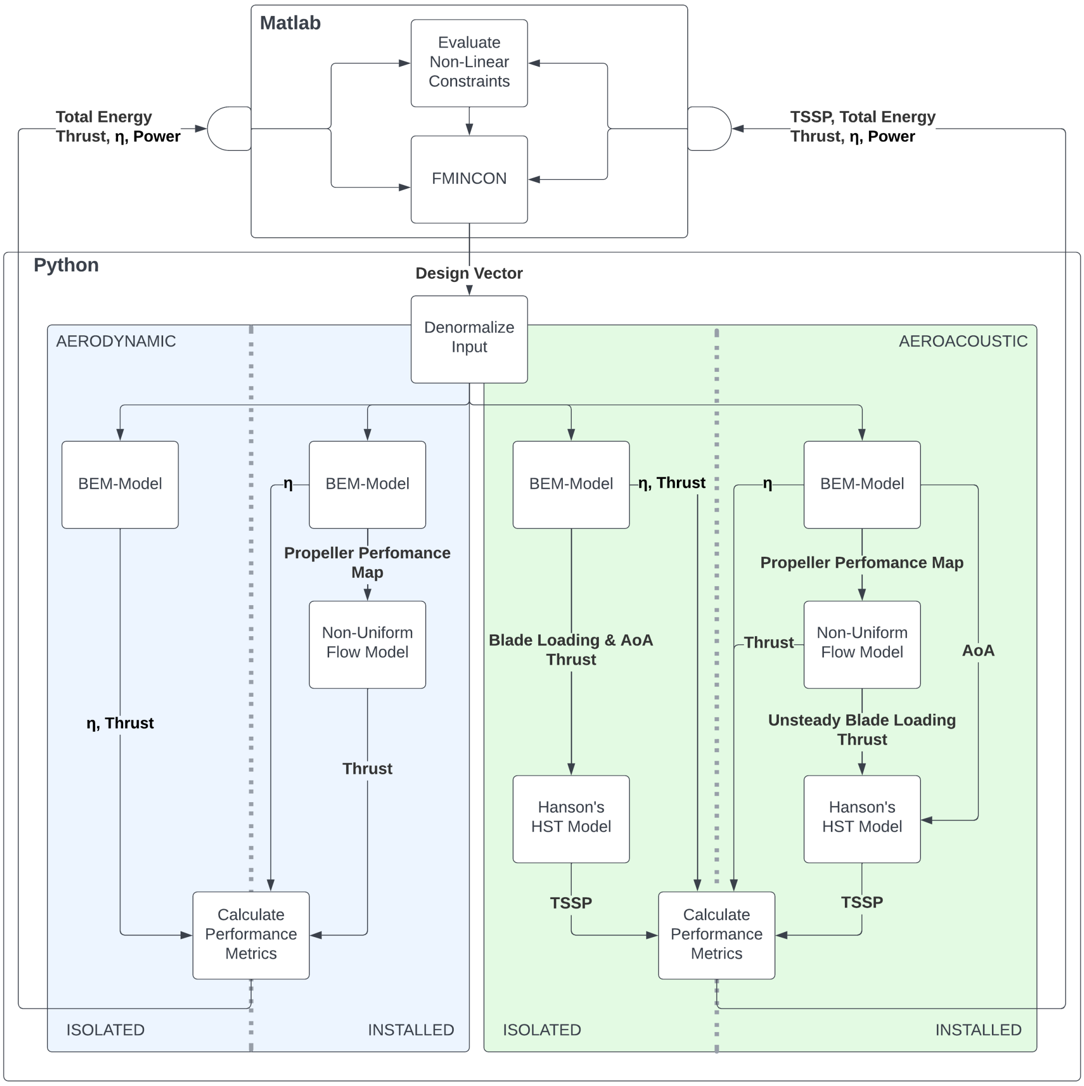

Fig. A.1 Full Optimization Workflow Diagram

The optimization setup has 4 different possible workflows, optimizing for aerodynamic (blue) or aeroaocustic performance (green), and within those realms, optimizing a propeller in uniform flow (isolated, left) or non-uniform flow (installed, right). Only one of these workflows is active at a time. As can be seen, the majority of the code was written and operates in Python, but the optimization controller FMINCON works from Matlab, and interacts with the Python code. The non-uniform flow data is provided to the Non-Uniform Flow Model in the form of a csv-file. The XPROP airfoil polar data is available to the code in the form of a .mat file that can be read by the Python code.